

# State Preparation for Quantum Information Science and Metrology

Von der Fakultät für Mathematik und Physik  
der Gottfried Wilhelm Leibniz Universität Hannover  
zur Erlangung des Grades

**Doktor der Naturwissenschaften**  
– Dr. rer. nat. –

genehmigte Dissertation  
von

**Dipl.-Phys. Aiko Samblowski**

geboren am 06. August 1981 in Hannover

2012

Referent:	Prof. Dr. Roman Schnabel
Korreferent:	Prof. Dr. Karsten Danzmann
Tag der Promotion:	08.06.2012

---

## Abstract

---

The precise preparation of non-classical states of light is a basic requirement for performing quantum information tasks and quantum metrology. Depending on the assignment, the range of required states varies from preparing and modifying squeezed states to generating bipartite entanglement and establishing multimode entanglement networks. Every state needs special preparation techniques and hence it is important to develop the experimental expertise to generate all states with the desired degree of accuracy.

In this thesis, the experimental preparation of different kinds of non-classical states of light is demonstrated. Starting with a multimode entangled state, the preparation of an unconditionally generated bound entangled state of light of unprecedented accuracy is shown. Its existence is of fundamental interest, since it certifies an intrinsic irreversibility of entanglement and suggests a connection with thermodynamics. The state is created in a network of linear optics, utilizing optical parametric amplifiers operated below threshold, beam splitters and phase gates. The experimental platform developed here afforded the precise and stable control of all experimental parameters.

Focusing on the aspect of quantum information networks, the generation of suitable bipartite entangled states of light is desirable. The optical connection between atomic transitions and light that can be transmitted via telecommunications fibers opens the possibility to employ quantum memories within fiber networks. For this purpose, a non-degenerate optical parametric oscillator is operated above threshold and the generation of bright bipartite entanglement between its twin beams at the wavelengths of 810 nm and 1550 nm is demonstrated.

In the field of metrology, quantum states are used to enhance the measurement precision of interferometric gravitational wave (GW) detectors. Recently, the sensitivity of a GW detector operated at a wavelength of 1064 nm was increased using squeezed vacuum states. In order to enhance the sensitivity of future GW detectors operating at a wavelength of 532 nm, squeezed vacuum states at this wavelength are required. With this intention, a highly efficient up-conversion of coherent states from 1550 nm to 532 nm is demonstrated. The presented setup is suitable to convert squeezed states in frequency. The preparation of squeezed vacuum states at 1550 nm can be realized with a standard approach using parametric down-conversion, while the transition to 532 nm is achievable by the presented sum-frequency generation process.

**Keywords:** Bipartite entanglement, bound entanglement, non-degenerate optical parametric oscillation, quantum frequency conversion.



---

## Kurzfassung

---

Die präzise Erzeugung nicht-klassischen Lichts ist ein grundlegender Baustein der Quanteninformation und der Quantenmetrologie. Je nach Aufgabengebiet werden unterschiedliche Zustände, wie zum Beispiel gequetschtes Licht, verschränkte Lichtfelder zwischen zwei Parteien und Verschränkungsnetzwerke mit mehreren involvierten Moden, benötigt. Jeder dieser Zustände wird mit speziellen Methoden präpariert, deren experimentelle Realisierbarkeit es zu entwickeln und zu optimieren gilt.

Im Rahmen dieser Arbeit wird die experimentelle Erzeugung unterschiedlicher Systeme nicht-klassischen Lichts demonstriert. Beginnend mit einem multimoden-verschränkten Zustand wird die unkonditionierte, hochpräzise Erzeugung eines gebunden-verschränkten Lichtfeldes gezeigt. Die Existenz dieses Zustandes ist von elementarer Relevanz, da sie auf einen irreversiblen Charakter der Dekohärenz von Verschränkung schließen lässt und eine Verbindung zwischen Quantentheorie und Thermodynamik nahelegt. Die Erzeugung des Zustandes wurde mithilfe eines Netzwerkes linearer Komponenten durchgeführt, das aus optischen parametrischen Verstärkern, die unterhalb der Schwellleistung betrieben wurden, Strahlteilern und Phasengattern bestand. Die entwickelte Plattform für die Zustandspräparation ermöglichte die präzise und stabile Kontrolle der großen Anzahl der benötigten experimentellen Parameter.

Großflächige Quanteninformationsnetzwerke können mithilfe von bereits vorhandenen Telekommunikationsfasernetzwerken ermöglicht werden. Quantenzustände, die eine optische Verbindung zwischen den Wellenlängen der Fasernetzwerke und atomarer Übergänge herstellen, ermöglichen dabei die Entwicklung von Quantenspeichern innerhalb dieser Netzwerke. Zu diesem Zweck wird im Rahmen dieser Arbeit die Erzeugung eines verschränkten Zustandes zwischen den Wellenlängen 1550 nm und 810 nm demonstriert. Ein nicht-entarteter optischer parametrischer Oszillator wurde hierfür oberhalb der Schwellleistung betrieben. Seine hellen Ausgangsfelder wurden untersucht und die Verschränkung zwischen ihnen nachgewiesen.

Im Bereich der Metrologie werden nicht-klassische Zustände zur Erhöhung der Messempfindlichkeit genutzt. Vor kurzem wurde der Gravitationswellendetektor GEO 600 mit gequetschtem Licht bei 1064 nm verbessert. Um zukünftige Detektoren, die bei 532 nm betrieben werden, zu verbessern, werden gequetschte Vakuumfelder bei dieser Wellenlänge benötigt. Hierfür wird im Rahmen dieser Arbeit die effiziente Quantenkonversion von 1550 nm zu 532 nm anhand kohärenter Zustände demonstriert. Die Ergebnisse zeigen, dass auch gequetschte Felder effizient aus dem nahinfraroten in den sichtbaren Bereich konvertiert werden können.

**Schlüsselwörter:** Gebundene Verschränkung, nicht-entarteter optischer parametrischer Oszillator, Quantenfrequenzkonversion, Zweiparteien-Verschränkung.



---

# Contents

---

<b>Abstract</b>	<b>iii</b>
<b>Kurzfassung</b>	<b>v</b>
<b>List of Figures</b>	<b>xii</b>
<b>List of Tables</b>	<b>xiii</b>
<b>Glossary</b>	<b>xv</b>
<b>1 Introduction</b>	<b>1</b>
1.1 Quantum Information Science . . . . .	2
1.2 Quantum Metrology . . . . .	3
1.3 Structure of the Thesis . . . . .	4
<b>2 Theoretical Description of Light</b>	<b>5</b>
2.1 Classical Description of Light Fields . . . . .	6
2.1.1 Coupled Wave Equations . . . . .	8
2.1.2 Sum-Frequency Generation . . . . .	9
2.1.3 Difference-Frequency Generation . . . . .	11
2.2 Quantization of the Electric Field . . . . .	13
2.3 Eigenstates of the Harmonic Oscillator . . . . .	16
2.4 Description of States by Quadrature Operators . . . . .	17
2.4.1 Vacuum States . . . . .	18
2.4.2 Coherent States . . . . .	18
2.4.3 Squeezed States . . . . .	20

---

<b>3</b>	<b>Gaussian States</b>	<b>21</b>
3.1	Gaussian States Described by the Wigner Function . . . . .	21
3.1.1	Examples of Wigner Functions . . . . .	24
3.2	Description of Linear Optics . . . . .	26
3.2.1	The Phase Shifter . . . . .	26
3.2.2	The Beam Splitter . . . . .	27
3.3	Reconstruction of a State's Covariance Matrix . . . . .	28
3.4	Verifying Gaussianity . . . . .	29
<b>4</b>	<b>Experimental Techniques</b>	<b>35</b>
4.1	Homodyne Detection . . . . .	35
4.2	Single Sideband Modulation – A Phase-Locking Scheme . . . . .	37
4.3	Variable Attenuation for Specific Squeezing Settings . . . . .	40
<b>5</b>	<b>Bound Entanglement</b>	<b>43</b>
5.1	Theoretical Description of Bound Entanglement . . . . .	43
5.1.1	Inseparability – An Entanglement Measure . . . . .	44
5.1.2	Partial Transposition – A Measure for Distillability . . . . .	45
5.2	The Search for Bound Entangled States . . . . .	45
5.3	Experimental Realization . . . . .	46
5.3.1	Laser and Squeezer . . . . .	47
5.3.2	Generation of Hot Squeezing . . . . .	51
5.3.3	Locking Scheme . . . . .	51
5.3.4	Phase Gates . . . . .	52
5.3.5	Measurement Process . . . . .	53
5.3.6	Experimental Parameters . . . . .	54
5.4	Gaussianity of the Prepared States . . . . .	56
5.5	Reconstructing the $8 \times 8$ Covariance Matrix . . . . .	58
5.6	Experimental Results . . . . .	61
5.7	Discussion . . . . .	62
<b>6</b>	<b>Twin Beams – Entanglement between 810 nm and 1550 nm</b>	<b>67</b>
6.1	Theory of Optical Parametric Oscillation above Threshold . . . . .	67
6.2	Quantum Correlations between the Twin Beams . . . . .	70
6.2.1	A Bipartite Entanglement Criterion . . . . .	76
6.3	Experimental Components . . . . .	77
6.3.1	Laser . . . . .	77
6.3.2	Second-Harmonic Generation . . . . .	78
6.3.3	Optical Parametric Oscillator . . . . .	78



---

6.4	Amplitude Correlation Measurement . . . . .	80
6.4.1	Experimental Setup . . . . .	80
6.4.2	Results . . . . .	80
6.5	Entanglement Measurement . . . . .	84
6.5.1	Experimental Setup . . . . .	84
6.5.2	Results . . . . .	86
6.6	Discussion . . . . .	87
<b>7</b>	<b>Quantum Frequency Conversion</b>	<b>89</b>
7.1	Quantum Theory of Sum-Frequency Generation . . . . .	89
7.2	Frequency Conversion of a Coherent State . . . . .	90
7.2.1	Experimental Setup . . . . .	91
7.2.2	Measurement Methods . . . . .	94
7.2.3	Numerical Simulations . . . . .	95
7.2.4	Measurement Results . . . . .	96
7.3	Discussion . . . . .	98
<b>8</b>	<b>Summary and Outlook</b>	<b>101</b>
<b>A</b>	<b>Convex Optimization Problems</b>	<b>105</b>
<b>B</b>	<b>Cavity Equations and Nonlinearities</b>	<b>107</b>
<b>C</b>	<b>Two-Mirror-Cavity with Absorption</b>	<b>113</b>
	<b>Acknowledgments</b>	<b>117</b>
	<b>Curriculum Vitae</b>	<b>119</b>
	<b>List of Publications</b>	<b>121</b>
	<b>Bibliography</b>	<b>125</b>



---

## List of Figures

---

2.1	Intensity of Sum-Frequency Generation . . . . .	12
2.2	Intensity of Difference-Frequency Generation . . . . .	13
3.1	Wigner Function of a Coherent State . . . . .	25
3.2	Wigner Function of a Squeezed State . . . . .	25
3.3	Gaussianity Check: Histograms . . . . .	31
3.4	Gaussianity Check: Cumulative Distribution Functions . . . . .	32
3.5	Gaussianity Check: QQ-Plots . . . . .	33
4.1	Schematic of a Balanced Homodyne Detector . . . . .	36
4.2	Error Signal for Balanced Homodyne Detectors and Phase Gates . . . . .	38
4.3	Schematic of a Phase Gate Lock . . . . .	39
5.1	Bound Entanglement: Overview of the Experimental Setup . . . . .	47
5.2	Bound Entanglement: Complete Optical Setup . . . . .	48
5.3	Squeezing Spectrum of Squeezer 3 . . . . .	50
5.4	Interference at the Phase Gates . . . . .	52
5.5	Phase Space of Distillability . . . . .	55
5.6	Phase Space of Inseparability . . . . .	55
5.7	Phase Space of Bound Entanglement . . . . .	56
5.8	Phase Space of Bound Entanglement – a zoom in . . . . .	57
5.9	Scan of Phase Gate 3 . . . . .	57
5.10	Comparison of Measured CDF . . . . .	59
5.11	QQ-plot of a Measurement’s Raw Data . . . . .	60
5.12	Bound Entanglement: Measurement Results . . . . .	63
5.13	Phase Gate Tuning: Experimental Results . . . . .	64

LIST OF FIGURES

---

6.1	Airy Function of a Doubly Resonant OPO . . . . .	69
6.2	Oscillation Restrictions of an OPO . . . . .	70
6.3	Visualization of Mode Hops and Cluster Jumps . . . . .	71
6.4	Difference-Frequency Generation: Schematics . . . . .	72
6.5	Amplitude Difference of Twin Beams . . . . .	73
6.6	Phase Sum of Twin Beams . . . . .	74
6.7	Twin Squeezing . . . . .	75
6.8	Asymmetric Amplitude Difference Noise . . . . .	76
6.9	Off-Resonance Asymmetric Amplitude Difference Noise . . . . .	77
6.10	Temperature Scan of the OPO . . . . .	79
6.11	OPO Mode Hops and Cluster Jumps . . . . .	79
6.12	OPO Output Power over Pump Power . . . . .	81
6.13	OPO Conversion Efficiency . . . . .	81
6.14	Measured Amplitude Difference . . . . .	82
6.15	Measured Amplitude Difference, Dark Noise Corrected . . . . .	83
6.16	Measured Amplitude Difference over Signal Power . . . . .	83
6.17	Spectrum of the Amplitude Difference . . . . .	84
6.18	Twin Beam Entanglement: Setup . . . . .	85
6.19	Twin Beam Entanglement: Results . . . . .	86
7.1	Conversion Efficiency Dependence on Pump Power . . . . .	91
7.2	Frequency Conversion: Setup . . . . .	92
7.3	SFG Cavity's Resonance Conditions . . . . .	93
7.4	SFG Optical Impedance due to Parasitical Cavities . . . . .	94
7.5	Design AR Coating . . . . .	95
7.6	Frequency Conversion: Results . . . . .	96
7.7	Frequency Conversion: Results . . . . .	97
7.8	Schematic of Squeezing Conversion Setup . . . . .	99
C.1	Schematic of a Linear Cavity . . . . .	114

---

## List of Tables

---

5.1	Initial Parameters of the Bound Entangled State . . . . .	53
5.2	Angle Sign Permutations of the Phase Gates . . . . .	54
5.3	Reconstructing the Covariance Matrix: Needed Measurements . . . . .	61
5.4	Best Obtained Covariance Matrix . . . . .	62
5.5	Phase Gate Tuning: Experimental Results . . . . .	65
7.1	Comparison of Conversion Measurements . . . . .	98



### List of Abbreviations

AC	alternating current
ADC	analog-to-digital converter
AOM	acousto-optical modulator
AR	anti-reflective
BHD	balanced homodyne detector
BS	50/50 beam splitter
CDF	cumulative distribution function
CV	continuous variables
DAQ	data acquisition system
dB	decibel
DBS	dichroic beam splitter
DC	direct current
DV	discrete variables
eLO	electronic local oscillator
EOM	electro-optical modulator
FMC	filter mode cleaner
FSR	free spectral range
FWHM	full width at half maximum
GEO 600	German-British gravitational wave observatory
GW	gravitational wave
HR	highly-reflective

KS	Kolmogorow-Smirnow
LO	local oscillator (optical)
LOCC	local operations and classical communication
MC	mode cleaner (three mirror ring cavity)
MgO:LiNbO <sub>3</sub>	Magnesium-oxide-doped Lithium Niobate
Nd:YAG	Neodymium-doped Yttrium Aluminum Garnet Nd:Y <sub>3</sub> Al <sub>5</sub> O <sub>12</sub>
NL	nonlinear
NPT	negative partial transposition
OPO	optical parametric oscillation
PBS	polarizing beam splitter
PC	personal computer
PD	photo-detector
PDH	Pound-Drever-Hall
PG	phase gate
PIN	positive intrinsic negative
PPKTP	periodically poled potassium titanyl phosphate KTiOPO <sub>4</sub>
PPL	phase-lock loop
PPT	positive partial transposition
PZT	piezo-electric transducer
QKD	quantum key distribution
RF	radio frequency
SA	spectrum analyzer
SFG	sum-frequency generator
SHD	self homodyne detector
SHG	second-harmonic generation
SPCM	single photon counting module
SQZ	squeezer
TEM	transverse electro-magnetic
thr	threshold
TMS	two-mode squeezing

### List of Symbols

This list is divided into a part originating from the Latin alphabet and another part originating from the Greek alphabet. Quantum mechanical operators and states are listed subsequently.



---





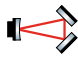
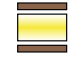




<b>B</b>	magnetic field vector
$\mathcal{B}$	magnetic field amplitude
$c$	speed of light
<b>D</b>	electric displacement field vector
$\mathbf{D}'_n{}^{(1)}$	one-frequency-mode electric displacement vector
$d_{\text{eff}}$	effective nonlinear coupling constant
diag	diagonal matrix
<b>E</b>	electric field vector
$\mathbf{E}'_n$	one-frequency-mode electric field vector
$\mathcal{E}$	electric field amplitude
$\mathbf{e}_{\mathbf{k}}$	unit polarization vector
$\mathbf{e}_{x,y,z}$	unit vectors
$E_n$	energy eigenvalue
eig	eigenvalue
$\mathcal{F}$	finesse
<b>H</b>	magnetizing field vector
$H$	Hamiltonian, classical
$i$	$\sqrt{-1}$
<b>J</b>	total current density vector
<b>k</b>	wave vector
$L$	length
$n$	linear index of refraction, photon number
$P$	optical power, optical
<b>P</b>	polarization vector
$\mathbf{P}'_n$	one-frequency-mode polarization vector
$R$	mirror power reflectivity
$r$	mirror amplitude reflectivity
$S(\omega)$	noise spectrum
$T$	temperature
$t$	mirror amplitude transmission, time
$\tau$	mirror power transmission, optical loss, cavity storage time
tr	trace
$W(\xi)$	Wigner function
$\alpha_{\mathbf{k}}$	complex field amplitude of mode $\mathbf{k}$
$\beta_{1,2,3}^{\text{in}}$	incoupling vacuum fields, associated with the intra-cavity losses

$\beta_i$	intensity absorption coefficient
$\chi^{(1)}$	linear optical susceptibility
$\chi^{(2)}$	second-order susceptibility
$\chi^{(3)}$	third-order susceptibility
$\delta$	relative depletion
$\delta_{jj'}$	Kronecker delta
$\Delta k$	wave vector mismatch
$\Delta\varphi$	phase mismatch
$\Delta\omega$	cavity linewidth
$\epsilon_0$	vacuum permittivity ( $8.85 \cdot 10^{-12}$ F/m)
$\epsilon_1 = 1 + \chi^{(1)}$	relative permittivity
$\eta$	efficiency
$\gamma_{1,2,3}$	intra-cavity round trip loss, associated with the output mirror
$\gamma^{(N)}$	$N$ -mode covariance matrix
$\gamma$	cavity linewidth (FWHM)
$\lambda$	wavelength
$\mu$	$2N$ -dimensional vector of quadrature displacement pairs
$\mu_i$	internal cavity loss per round trip
$\mu_0$	vacuum permeability
$\nabla$	del operator
$\omega$	angular frequency
$\rho$	total charge density
$\sigma$	pump power ratio
$\xi$	squeezing parameter, $2N$ -dimensional vector of quadrature amplitudes
$\hbar$	Planck constant, reduced
$B(\gamma)$	measure for Heisenberg's Uncertainty Relation
$E(\gamma)$	measure for separability
$P(\gamma)$	measure for distillability
$\mathcal{I}$	measure for inseparability (Duan)
$\hat{\mathbb{1}}$	identity operator
$\hat{a}$	annihilation operator
$\hat{a}^\dagger$	creation operator
$\hat{B}(\tau)$	beam splitter operator
$\hat{D}(\alpha)$	displacement operator

$\hat{H}$	Hamiltonian
$\hat{i}$	current operator
$\hat{n}$	number operator
$\hat{R}(\theta)$	rotation operator
$\hat{S}(\xi)$	squeezing operator
$\Delta_s \hat{A}$	standard deviation of operator $\hat{A}$
$\langle (\Delta \hat{A})^2 \rangle$	variance of operator $\hat{A}$
$V_{S,A}$	variance of squeezed/anti-squeezed quadrature
$\hat{x}$	amplitude quadrature operator
$\hat{p}$	phase quadrature operator
$\hat{x}^\theta$	arbitrary quadrature operator at angle $\theta$
$ \alpha\rangle$	coherent state
$ n\rangle$	number state

### List of Pictograms

The following pictograms were used to visualize the experimental setups. They are taken from the *Component Library* designed by Alexander Franzen (component library by alexander franzen 2016).

	laser
	hemilithic optical cavity containing a $\chi^{(2)}$ nonlinear crystal
	two-mirror optical cavity containing a $\chi^{(2)}$ nonlinear crystal
	monolithic optical cavity containing a $\chi^{(2)}$ nonlinear crystal
	spatial mode-cleaning traveling-wave resonator (mode-cleaner or MC)
	electro-optical modulator
	$\lambda/2$ wave plate (1064 nm and 532 nm)
	beam splitter
	beam splitter
	polarizing beam splitter (PBS)

## GLOSSARY

---

	dichroic beam splitter (DBS, transmits 532 nm, reflects 1064 nm)
	dichroic beam splitter (DBS, transmits 532 nm, reflects 1550 nm)
	dichroic beam splitter (DBS, transmits 532 nm, 1550 nm, reflects 810 nm)
	highly reflective (HR) steering mirror
	piezo-actuated steering mirror
	Faraday rotator
	beam dump
	photo-detector
	phase shifter (optical and electronic)
	electronic signal generator
	electronic mixer
	electronic subtraction
	electronic addition / subtraction
	electronic low pass (LP) filter
	PID controller
	high voltage (HV) amplifier
	data acquisition (DAQ) system
	spectrum analyzer (SA)

# CHAPTER 1

---

## Introduction

---

Quantum mechanics is one of the pillars of modern physics. It has been verified by a huge number of experimental studies and is successful in describing many physical phenomena that cannot be explained by classical theories. Although its beginning dates back over a century when Max Planck postulated the quantized nature of light and gave a description of blackbody radiation in 1901 [1], its counter-intuitive behavior still engages scientists all over the world. Possibly *the* most fascinating property of quantum mechanics is the *entanglement* between two or more physical parties. In contrast to classical theories, the individual (spatially separated) parties cannot be fully described by a local theory. Correlations stronger than allowed by any classical (local) theory can occur between the parties. Albert Einstein, Boris Podolsky and Nathan Rosen – also known as EPR – argued in 1935 that quantum mechanics must be incomplete, since it is contradictory to the intuitively graspable local reality [2]. They urged a theory with hidden variables to explain the possible correlations. In 1964 John Bell formulated his famous inequalities which allow an experimental distinction between a local theory with hidden variables and a non-local theory, such as quantum mechanics [3]. It was not until 1982, however, that Alain Aspect *et al.* demonstrated polarization entanglement of photons and refuted the Bell inequalities in favor of quantum mechanics within the realm of quantum optics [4].

The beginning of quantum optics goes back to Jeffrey Kimble *et al.* in 1977, who demonstrated the first quantum effect in an optical experiment: photon antibunching in resonance fluorescence [5]. The non-classical photon statistics were measured with photomultiplier tubes, which could either detect a photon or could not. This discrete type of “yes/no” measurement defined the regime of the first experiments in quantum

optics – the regime of discrete variables (DV). It took another eight years until Richard Slusher *et al.* could demonstrate a second quantum effect of light: squeezing of quantum fluctuations [6]. Here, the nonlinear four wave mixing process was used to reshape the quantum noise distribution of the field’s quadrature amplitudes. The measurements were performed with balanced homodyne detection and yielded a continuous data spectrum – this was the advent of the regime of continuous variables (CV). The measurement apparatus defines the properties under investigation and illustrates the particle *and* wave nature of light.

Great progress has been made since the discovery of the first optical quantum effects. The insight that the counterintuitive features of quantum mechanics can be utilized gave rise to the fields of quantum information and quantum metrology in the last decades.

In order to implement new technological applications and to investigate novel concepts, the precise preparation of quantum states of light is a basic requirement. Depending on the assignment, the states must exhibit specially designed features. Within this thesis we consider state preparation for quantum information science and quantum metrology in the continuous variable regime.

## 1.1 Quantum Information Science

The field of quantum information science combines quantum physics with communication theory and computer science. Utilizing the peculiar properties of quantum mechanics enabled novel fundamental research and the development of new applications. After the realization of CV entanglement in 1992 by Ou *et al.* [7], major achievements in the area of entanglement based quantum communication in the CV regime were made in the last two decades: teleportation of coherent states [8–11], enhancement of the classical channel capacity using dense coding [12–14] and quantum key distribution (QKD) [15–18]. Long distant quantum networks came within reach with the realization of quantum memory for light [19, 20], entanglement swapping [21, 22] and entanglement distillation [23–25]. Satisfying CV quantum computing is still pending, although great progress in one-way computing with cluster states has been made recently [26, 27].

The study and precise preparation of entangled states is a fundamental requirement to further improve the existing techniques and to develop new applications. Within the framework of quantum information the preparation of an unconditionally generated bound entangled state of light is presented in Chapter 5 of this thesis. This multi-mode entangled state has been realized for the first time in the CV regime with an extraordinary significance. Its existence is of fundamental interest, since it certifies an intrinsic irreversibility of entanglement and suggests a connection with thermodynamics [28, 29]. Although its properties – entangled but not distillable – seem to be

unattractive for applications at first glance, it can be used to “superactivate” quantum channels with zero capacity and enables quantum communication [30, 31]. Hence, its realization enables not only the study of fundamental entanglement properties but also the development of new quantum communication channels. The bound entangled state is created in a network of linear optics, utilizing optical parametric amplifiers operated below threshold, beam splitters and phase gates. The experimental platform developed in this work afforded the precise and stable control of all experimental parameters.

Focusing on the aspect of quantum information networks, the generation of suitable bipartite entangled states of light is desirable. To implement quantum protocols between remote parties, the entangled states are already nowadays distributed by existing telecommunications fiber networks operated at a wavelength of 1550 nm [32]. Even though standard fibers have reached very low attenuation values of about 0.17 dB/km [33], quantum repeaters are necessary to bridge distances of several hundred kilometers [34, 35]. Alkaline atoms having transition lines at wavelengths around 810 nm may be used to establish quantum memories [36, 37] that are an essential requirement in quantum repeaters. To connect these two wavelengths, entangled twin beams between 810 nm and 1550 nm could be used to transfer the quantum states from one wavelength to the other via entanglement swapping [22]. To achieve this, the operation of a non-degenerate optical parametric oscillator above threshold is discussed in Chapter 6. The generation of bright bipartite entanglement between twin beams at the wavelengths of 810 nm and 1550 nm is demonstrated.

## 1.2 Quantum Metrology

Quantum states can be used to obtain an improved measurement precision within the field of metrology. In the DV regime, so called  $N00N$  states have been used in the recent past to improve phase measurements of an Mach-Zehnder interferometer operated with very low photon rates [38]. In the CV regime, Carlton Caves proposed in 1981 the use of squeezed states to improve the sensitivity of high-power laser interferometers [39]. It took, however, three decades until the measurement sensitivity of large-scale laser interferometers was enhanced. It was recently realized in the gravitational wave (GW) detector GEO 600 by combining ultra-stable coherent light with squeezed vacuum states at a laser wavelength of 1064 nm [40]. Assuming a fixed laser power, the sensitivity of such interferometers can still be improved by increasing the squeezing factor and by reducing the laser wavelength. The combination of both approaches is not easy to achieve, since material properties of the nonlinear squeezing media limit the generation of squeezed vacuum states at short, e.g. visible, wavelengths. One solution can be the frequency up-conversion of squeezed states from

near-infrared wavelengths, where strong squeezed states have been realized recently [41].

The highly efficient experimental frequency up-conversion of a continuous-wave coherent light field from 1550 nm to 532 nm is demonstrated in Chapter 7. The possibility of generating strongly squeezed vacuum states at 532 nm with this technique for the improvement of future GW detectors, such as *DECIGO* [42], is discussed.

### 1.3 Structure of the Thesis

The structure of the following chapters of this thesis is as follows:

- *Chapters 2–4* give an overview of general theoretical and experimental concepts. These chapters review a general quantum mechanical formalism for quantum optics, concepts particularly useful for the description of Gaussian states, and experimental techniques used within the thesis.
- *Chapters 5–6* discuss the experiments conducted in the realm of quantum information science. They provide special theoretical background, describe the experimental layout and present the obtained results.
- *Chapter 7* presents and discusses the experiment conducted in the realm of quantum metrology.
- *Chapter 8* summarizes the obtained experimental results and gives an outlook.



## CHAPTER 2

---

### Theoretical Description of Light

---

In 1865, James Clerk Maxwell set the theoretical foundation for modern electrodynamics. In his publication “A Dynamical Theory of the Electromagnetic Field” [43] he proposed eight equations, which describe light as oscillations of the electromagnetic field. Today, we know a combination of these equations in a vectorized form as the four Maxwell’s equations.

A new era in physics arose in 1901 when Max Planck described black body radiation by quantizing its energy [1]. He formed the basis of quantum mechanics, which would eliminate disagreements between classical theories and experiments and explain new and counterintuitive features of nature. An extension of Planck’s idea allowed Albert Einstein to explain the photo-electric effect in 1905 [44] and led him to introduce the concept of photons. A couple of years later, in the 1920s, a quantum theory of radiation had been developed by Max Born, Pascual Jordan, Werner Heisenberg and Paul Dirac. Nevertheless, the theory could not provide a quantitative description of physical processes until Roy Glauber developed the quantum theory of optical decoherence in 1963 [45, 46].

In this chapter we outline the classical and quantum description of light. First, we will derive the classical wave equation from Maxwell’s equations for nonlinear media. This provides the basis to understand the nonlinear optical phenomena – such as down-conversion and sum-frequency generation – used within this thesis. Then, we will quantize the classical wave equation to obtain a quantum mechanical description and give an overview of quantum mechanical states.

## 2.1 Classical Description of Light Fields

In order to describe optical effects occurring in nonlinear media – such as second-harmonic generation, sum-frequency generation or down-conversion – we need to obtain the wave equation for the propagation of light through such a medium. We follow the approach in [47] and employ Maxwell’s equations. In SI units, they read

$$\nabla \cdot \mathbf{D} = \rho \qquad \nabla \cdot \mathbf{B} = 0 \qquad (2.1a,b)$$

$$\nabla \times \mathbf{E} = -\frac{\partial \mathbf{B}}{\partial t} \qquad \nabla \times \mathbf{H} = \frac{\partial \mathbf{D}}{\partial t} + \mathbf{J} \qquad (2.1c,d)$$

where  $\mathbf{E}$  is the electric field,  $\mathbf{D}$  the electric displacement field,  $\mathbf{B}$  the magnetic field,  $\mathbf{H}$  the magnetizing field,  $\mathbf{J}$  the total current density and  $\rho$  the total charge density.

In our case, we are interested in the solution of these equations in regions of space that neither contain free charges nor free currents, i.e. where

$$\rho = 0, \qquad \mathbf{J} = 0. \qquad (2.2a,b)$$

We also assume that the material is non-magnetic, which is true for common optical nonlinear materials

$$\mathbf{B} = \mu_0 \mathbf{H}. \qquad (2.3)$$

Since the material is allowed to be nonlinear, the electric displacement field  $\mathbf{D}$  and the electric field  $\mathbf{E}$  are related by

$$\mathbf{D} = \epsilon_0 \mathbf{E} + \mathbf{P}, \qquad (2.4)$$

where  $\epsilon_0$  depicts the permittivity of free space and the polarization vector  $\mathbf{P}$  depends nonlinearly upon the electric field  $\mathbf{E}$

$$\begin{aligned} \mathbf{P} &= \epsilon_0 \sum_{n=1}^{\infty} \chi^{(n)} \mathbf{E}^n \\ &= \sum_{n=1}^{\infty} \mathbf{P}^{(n)}. \end{aligned}$$

$\chi^{(1)}$  is the linear optical susceptibility, while the quantities  $\chi^{(2)}$  and  $\chi^{(3)}$  are known as the second- and third-order nonlinear optical susceptibility, respectively. The nonlinear processes we are interested in are describable solely with the second-order susceptibility.

To obtain the wave equation, we take the curl of the Maxwell Equation (2.1c), interchange the order of space and time derivative and use Equations (2.1d), (2.2b) and (2.3):

$$\nabla \times \nabla \times \mathbf{E} + \frac{1}{c^2} \frac{\partial^2}{\partial t^2} \mathbf{E} = -\mu_0 \frac{\partial^2}{\partial t^2} \mathbf{P}.$$

To simplify this expression, we can write the first term of the left-hand side as

$$\nabla \times \nabla \times \mathbf{E} = \nabla (\nabla \cdot \mathbf{E}) - \nabla^2 \mathbf{E}.$$

In linear optics the first term on the right-hand side vanishes because the Maxwell Equation (2.1a) implies that  $\nabla \cdot \mathbf{E} = 0$ . In nonlinear optics this is not true in general; see Equation (2.4). Fortunately, the divergence term can usually be neglected. If we consider a transverse, infinite plane wave,  $\nabla \cdot \mathbf{E}$  vanishes anyway. But even if the term does not vanish, it can often be shown to be small, especially if the slowly varying amplitude approximation (see Section 7.1) is valid. Assuming this, we obtain the wave equation in the form

$$\nabla^2 \mathbf{E} - \frac{1}{c^2} \frac{\partial^2}{\partial t^2} \mathbf{E} = \mu_0 \frac{\partial^2}{\partial t^2} \mathbf{P}.$$

It is convenient to split  $\mathbf{P}$  and  $\mathbf{D}$  into their linear and nonlinear parts

$$\mathbf{P} = \mathbf{P}^{(1)} + \mathbf{P}^{(\text{NL})}, \quad (2.5a)$$

$$\mathbf{D} = \mathbf{D}^{(1)} + \mathbf{P}^{(\text{NL})}, \quad (2.5b)$$

where the linear electric displacement is given by

$$\mathbf{D}^{(1)} = \epsilon_0 \mathbf{E} + \mathbf{P}^{(1)} = \epsilon_0 \underline{\underline{\epsilon}}^{(1)} \cdot \mathbf{E}, \quad (2.6)$$

where  $\underline{\underline{\epsilon}}^{(1)}$  depicts the frequency-independent dielectric tensor, which simplifies to a dimensionless scalar quantity  $\epsilon^{(1)} = 1 + \chi^{(1)}$  in the case of an isotropic medium. The rewritten wave equation for an isotropic, dispersionless medium then reads

$$\nabla^2 \mathbf{E} - \frac{\epsilon^{(1)}}{c^2} \frac{\partial^2}{\partial t^2} \mathbf{E} = \mu_0 \frac{\partial^2}{\partial t^2} \mathbf{P}^{(\text{NL})}. \quad (2.7)$$

Since most  $\chi^{(2)}$ -media are dispersive, we have to treat every frequency component separately. We write the electric field, the electric displacement field and the polarization field as sums of their frequency components

$$\mathbf{E}(\mathbf{r}, t) = \sum_n \mathbf{E}'_n(\mathbf{r}, t) = \sum_n \left[ \mathbf{E}_n(\mathbf{r}) e^{-i\omega_n t} + \mathbf{E}_n^*(\mathbf{r}) e^{i\omega_n t} \right] \quad (2.8a)$$

$$\mathbf{D}^{(1)}(\mathbf{r}, t) = \sum_n \mathbf{D}'_n{}^{(1)}(\mathbf{r}, t) = \sum_n \left[ \mathbf{D}_n^{(1)}(\mathbf{r}) e^{-i\omega_n t} + \mathbf{D}_n^{*(1)}(\mathbf{r}) e^{i\omega_n t} \right] \quad (2.8b)$$

$$\mathbf{P}^{(\text{NL})}(\mathbf{r}, t) = \sum_n \mathbf{P}'_n{}^{(\text{NL})}(\mathbf{r}, t) = \sum_n \left[ \mathbf{P}_n^{(\text{NL})}(\mathbf{r}) e^{-i\omega_n t} + \mathbf{P}_n^{*(\text{NL})}(\mathbf{r}) e^{i\omega_n t} \right] \quad (2.8c)$$

and connect the one-frequency-mode electric displacement  $\mathbf{D}'_n{}^{(1)}$  with the one-frequency-mode electric field  $\mathbf{E}'_n$  analogously to Equation (2.6) with a real, frequency-dependent dielectric tensor

$$\mathbf{D}'_n{}^{(1)} = \epsilon_0 \underline{\underline{\epsilon}}^{(1)}(\omega_n) \cdot \mathbf{E}'_n. \quad (2.9)$$

If we now combine Equations (2.8) and (2.9) with the wave equation (2.7) we obtain the final wave equation that is valid for each frequency component of the field

$$\nabla^2 \mathbf{E}'_n - \frac{\epsilon^{(1)}(\omega_n)}{c^2} \frac{\partial^2}{\partial t^2} \mathbf{E}'_n = \mu_0 \frac{\partial^2}{\partial t^2} \mathbf{P}'^{(\text{NL})}_n. \quad (2.10)$$

This solution has the form of a driven wave equation. The nonlinear response of the medium behaves as a source that appears on the right-hand side. We will use this expression in the following subsections to derive sum-frequency generation and down-conversion processes, which are needed in Chapter 6 and Chapter 7.

Without this source ( $\mathbf{P}'^{(\text{NL})}_n = 0$ ), the equation depicts a free propagating wave with velocity  $c/n$ , where  $n$  is the linear index of refraction that satisfies  $n^2 = \epsilon^{(1)}$ . For simplicity, we will quantize this expression in Section 2.2 to obtain a quantum mechanical description of the light field.

### 2.1.1 Coupled Wave Equations

We now continue following [47] and sketch the derivation of the sum-frequency generation, where two optical fields with (angular) frequency  $\omega_{1,2}$  create a new field having  $\omega_3 = \omega_1 + \omega_2$  within a nonlinear medium. This will lead to the coupled wave equations of a lossless  $\chi^{(2)}$  medium. Equation (2.10) must hold for all involved fields. Without a nonlinear source the plane wave solution for the sum-frequency component is

$$E'_3(z, t) = E_3 e^{i(k_3 z - \omega_3 t)} + E_3^* e^{-i(k_3 z - \omega_3 t)}, \quad (2.11)$$

which assumes a propagation along the  $z$ -axis with frequency  $\omega_3$ , wave vector  $k_3 = \frac{n_3 \omega_3}{c}$ , index of refraction  $n_3^2 = \epsilon^{(1)}(\omega_3)$  and constant field amplitude  $E_3$ . Taking the nonlinear source term into account, Equation (2.8c) gives

$$P'_3{}^{(\text{NL})}(z, t) = P_3^{(\text{NL})} e^{-i\omega_3 t} + P_3^{*(\text{NL})} e^{i\omega_3 t}, \quad (2.12)$$

with  $P_3^{(\text{NL})} = 4\epsilon_0 d_{\text{eff}} E_1 e^{ik_1 z} E_2 e^{ik_2 z}$ .  $d_{\text{eff}}$  denotes the effective nonlinear coupling constant. Substituting Equations (2.11) and (2.12) into the Wave Equation (2.10) and replacing  $\nabla^2$  by  $\frac{d^2}{dz^2}$  yields

$$\begin{aligned} & \left[ \frac{d^2 E_3}{dz^2} + 2ik_3 \frac{dE_3}{dz} - k_3^2 E_3 + \frac{\epsilon^{(1)}(\omega_3) \omega_3^2 E_3}{c^2} \right] e^{i(k_3 z - \omega_3 t)} \\ & + \left[ \frac{d^2 E_3^*}{dz^2} - 2ik_3 \frac{dE_3^*}{dz} - k_3^2 E_3^* + \frac{\epsilon^{(1)}(\omega_3) \omega_3^2 E_3^*}{c^2} \right] e^{-i(k_3 z - \omega_3 t)} \\ & = \frac{-4d_{\text{eff}} \omega_3^2}{c^2} E_1 E_2 e^{i[(k_1 + k_2)z - \omega_3 t]} + \frac{-4d_{\text{eff}} \omega_3^2}{c^2} E_1^* E_2^* e^{-i[(k_1 + k_2)z - \omega_3 t]}. \end{aligned}$$

With  $k_3^2 = \frac{\epsilon^{(1)}(\omega_3)\omega_3^2}{c^2}$  and dropping the complex conjugate we obtain

$$\frac{d^2 E_3}{dz^2} + 2ik_3 \frac{dE_3}{dz} = \frac{-4d_{\text{eff}}\omega_3^2}{c^2} E_1 E_2 e^{i(k_1+k_2-k_3)z}.$$

Since the second order derivative is usually much smaller than the first order one,  $\left|\frac{d^2 E_3}{dz^2}\right| \ll \left|k_3 \frac{dE_3}{dz}\right|$ , we apply the *slowly varying amplitude* approximation by neglecting the second derivative and obtain the coupled amplitude equation

$$\frac{dE_3}{dz} = \frac{2id_{\text{eff}}\omega_3^2}{k_3 c^2} E_1 E_2 e^{i\Delta k z}, \quad (2.13)$$

with the wave vector mismatch  $\Delta k = k_1 + k_2 - k_3$ . In general we need to take the spatial variations of  $E_1$  and  $E_2$  into account and obtain analogously the remaining coupled wave equations

$$\frac{dE_1}{dz} = \frac{2id_{\text{eff}}\omega_1^2}{k_1 c^2} E_3 E_2^* e^{-i\Delta k z}, \quad (2.14)$$

$$\frac{dE_2}{dz} = \frac{2id_{\text{eff}}\omega_2^2}{k_2 c^2} E_3 E_1^* e^{-i\Delta k z}. \quad (2.15)$$

### 2.1.2 Sum-Frequency Generation

In this thesis we are interested in the case of sum-frequency generation, where a strong pump field  $\omega_2$  is used to up-convert a weak signal field  $\omega_1$ , see Chapter 7. By assuming that the pump field is not depleted by the interaction ( $E_2 = \text{const}$ ), the coupled Equations (2.13) through (2.15) simplify to:

$$\frac{dE_1}{dz} = K_1 E_3 e^{-i\Delta k z}, \quad (2.16)$$

$$\frac{dE_3}{dz} = K_3 E_1 e^{+i\Delta k z}, \quad (2.17)$$

with the quantities

$$K_1 = \frac{2i\omega_1^2 d_{\text{eff}}}{k_1 c^2} E_2^*, \quad K_3 = \frac{2i\omega_3^2 d_{\text{eff}}}{k_3 c^2} E_2.$$

For a non-vanishing wave vector mismatch,  $\Delta k \neq 0$ , we expect solutions of the form

$$E_1(z) = (F e^{igz} + G e^{-igz}) e^{-i\Delta k z/2}, \quad (2.18)$$

$$E_3(z) = (C e^{igz} + D e^{-igz}) e^{-i\Delta k z/2}, \quad (2.19)$$

where  $g$  is the rate of the field's spatial variation and  $C$ ,  $D$ ,  $F$  and  $G$  are constants depending on the boundary conditions. Substituting Equation (2.18) and (2.19) into Equation (2.16) gives

$$\begin{aligned} (igFe^{igz} - igGe^{-igz})e^{-\frac{i}{2}\Delta kz} - \frac{i}{2}\Delta k (Fe^{igz} + Ge^{-igz})e^{-\frac{i}{2}\Delta kz} \\ = (K_1Ce^{igz} + K_1De^{-igz})e^{-\frac{i}{2}\Delta kz}. \end{aligned}$$

Since this equation has to hold for all values of  $z$ , the coefficients of  $e^{\pm igz}$  must be related by

$$F \left( ig - \frac{i}{2}\Delta k \right) = K_1 C, \quad (2.20)$$

$$-G \left( ig + \frac{i}{2}\Delta k \right) = K_1 D. \quad (2.21)$$

Analogously we obtain with Equation (2.17)

$$\begin{aligned} (igCe^{igz} - igDe^{-igz})e^{\frac{i}{2}\Delta kz} + \frac{i}{2}\Delta k (Ce^{igz} + De^{-igz})e^{\frac{i}{2}\Delta kz} \\ = (K_3Fe^{igz} + K_3Ge^{-igz})e^{\frac{i}{2}\Delta kz} \end{aligned}$$

and hence a relation for the coefficients

$$C \left( ig + \frac{i}{2}\Delta k \right) = K_3 F, \quad (2.22)$$

$$-D \left( ig - \frac{i}{2}\Delta k \right) = K_3 G.$$

Equations (2.20) and (2.22) restrict the solution of  $F$  and  $C$ . They read in matrix form

$$\begin{pmatrix} i \left( g - \frac{1}{2}\Delta k \right) & -K_1 \\ -K_3 & i \left( g + \frac{1}{2}\Delta k \right) \end{pmatrix} \begin{pmatrix} F \\ C \end{pmatrix} = 0.$$

A solution exists, if the determinant vanishes, hence

$$g^2 = \kappa^2 + \frac{1}{4}\Delta k^2$$

with  $\kappa^2 = -K_1K_3$ . Assuming that the fields  $E_1(z=0)$  and  $E_3(z=0)$  are known at the input plane of the nonlinear medium, this yields from Equations (2.18) and (2.19)

$$E_1(0) = F + G,$$

$$E_3(0) = C + D.$$

Equations (2.20) and (2.21) provide two additional restrictions among the constants. The general solutions of Equations (2.18) and (2.19) that fulfill the boundary conditions read

$$\begin{aligned} E_1(z) &= \left[ E_1(0) \cos(gz) + \left( \frac{K_1}{g} E_3(0) + \frac{i\Delta k}{2g} E_1(0) \right) \sin(gz) \right] e^{-\frac{i}{2}\Delta kz}, \\ E_3(z) &= \left[ E_3(0) \cos(gz) + \left( \frac{-i\Delta k}{2g} E_3(0) + \frac{K_3}{g} E_1(0) \right) \sin(gz) \right] e^{\frac{i}{2}\Delta kz}. \end{aligned} \quad (2.23)$$

Considering the case that no sum-frequency field  $\omega_3$  is present at the beginning,  $E_3(0) = 0$ , Equation (2.23) simplifies to

$$E_3(z) = \frac{K_3}{g} E_1(0) \sin(gz) e^{\frac{i}{2}\Delta kz}.$$

The measurable intensity of the generated wave

$$|E_3(z)|^2 = |E_1(0)|^2 \frac{|K_3|^2}{g^2} \sin^2(gz)$$

shows an oscillatory behavior. For a vanishing wave vector mismatch ( $\Delta k = 0$ )  $g$  becomes minimal and the generated intensity maximal. It reaches its maximum at a certain penetration depth, after which the field gets back-converted, see Figure 2.1. The degenerated case of  $\omega_1 = \omega_2 =: \omega$  corresponds to *second-harmonic generation* (SHG). Two photons of energy  $\hbar\omega$  merge to one photon of energy  $2\hbar\omega$ .

### 2.1.3 Difference-Frequency Generation

We will now consider the opposite case: the interaction of two optical fields at  $\omega_3$  and  $\omega_1$  in a lossless  $\chi^{(2)}$  medium producing an output field at the difference-frequency  $\omega_2 = \omega_3 - \omega_1$ .  $\omega_3$  is treated as a strong, undepleted pump field, i.e.  $E_3 = \text{const}$ . The wave vector mismatch is now given by  $\Delta k = k_3 - k_1 - k_2$  and the coupled wave Equations (2.13) and (2.14) transform to

$$\frac{dE_1}{dz} = \frac{2id_{\text{eff}}\omega_1^2}{k_1c^2} E_3 E_2^* e^{i\Delta kz}, \quad (2.24)$$

$$\frac{dE_2}{dz} = \frac{2id_{\text{eff}}\omega_2^2}{k_2c^2} E_3 E_1^* e^{i\Delta kz}. \quad (2.25)$$

For perfect phase matching,  $\Delta k = 0$ , we differentiate Equation (2.25) and use the complex conjugate of Equation (2.24) to obtain

$$\frac{d^2 E_2}{dz^2} = \frac{4d_{\text{eff}}^2 \omega_1^2 \omega_2^2}{k_1 k_2 c^4} E_3 E_3^* E_2 \equiv \kappa^2 E_2.$$

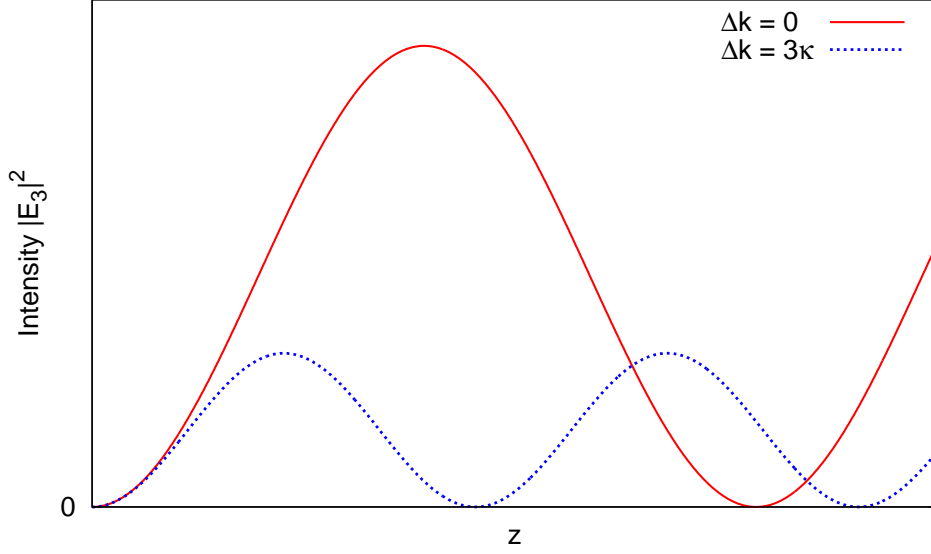


**Figure 2.1** – Intensity of sum-frequency generation over penetration depth in the nonlinear medium for an undepleted pump. The intensity is maximal at a certain penetration depth and back-converted afterwards. Maximum position and height depend on the wave vector mismatch.

The coupling constant  $\kappa$  is given by  $\kappa^2 = \frac{4d_{\text{eff}}^2\omega_1^2\omega_2^2}{k_1k_2c^4} |E_3|^2$  and a general solution reads

$$E_2(z) = C \sinh(\kappa z) + D \cosh(\kappa z) .$$

Assuming the boundary conditions

$$E_2(0) = 0, \quad E_1(0) = \text{const} ,$$

yields the solutions

$$E_1(z) = E_1(0) \cosh(\kappa z) ,$$

$$E_2(z) = i \sqrt{\frac{n_1\omega_2}{n_2\omega_1}} \frac{E_3}{|E_3|} E_1^*(0) \sinh(\kappa z) .$$

The initial *signal* field at  $\omega_1$  gets amplified by the process and generates an *idler* field at  $\omega_2$  for conservation of energy. The generation of the  $\omega_1$  field stimulates the generation of the  $\omega_2$  field and vice versa. Hence we do not observe an oscillatory behavior as for sum-frequency generation and each field grows exponentially with  $e^{\kappa z}$  for large  $\kappa z$ , as shown in Figure 2.2. The difference-frequency generation, or parametric amplification, plays a central role in the generation of entangled fields, as later discussed in Chapter 6.



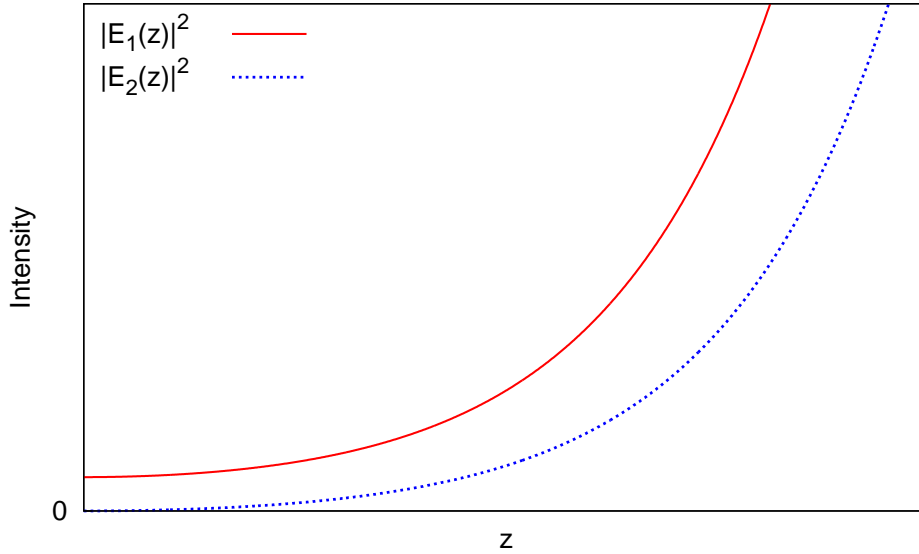


**Figure 2.2** – Intensity of difference-frequency generation over penetration depth in the nonlinear medium for an undepleted pump and zero phase mismatching. The initial signal field at  $\omega_1$  grows and generates an idler field at  $\omega_2$ . For large  $\kappa z$  each field grows exponentially as  $e^{\kappa z}$ .

## 2.2 Quantization of the Electric Field

One approach to describe a classical theory quantum mechanically is the canonical quantization. Here, the classical theory is written in the Hamilton formalism and the canonical position and momentum variables are replaced by operators, obeying the quantum mechanical commutation relation.

In order to find a quantum mechanical description for light, we follow the approach in [48, 49] and quantize the electric field. Therefore, we consider an electric field inside a perfect cavity of length  $L$ . Due to the boundary conditions, it forms a standing wave with frequency  $\omega_m = c(m\pi/L)$ ,  $m \in \mathbb{N}^+$ . We assume that it propagates in the  $z$ -direction and is polarized along the  $x$ -axis. For reasons of readability we drop the index  $m$  and simply write  $\omega$  for the resonance frequency of all possible modes.

According to wave equation (2.10), a solution for the electric field is given by

$$E_x(z, t) = \sqrt{\frac{2\omega^2}{V\epsilon_0}} Q(t) \sin(kz), \quad (2.26)$$

where  $k = \omega/c$  is the wave number,  $V = L^3$  the effective cavity volume and  $Q(t)$  a time-dependent factor with the dimension of a length. According to Equations (2.1d)

and (2.26), the magnetic field  $\mathbf{B}(\mathbf{r}, t) = \mathbf{e}_y B_y(z, t)$  is given by

$$B_y(z, t) = \frac{\mu_0 \epsilon_0}{k} \sqrt{\frac{2\omega^2}{V \epsilon_0}} \dot{Q}(t) \cos(kz). \quad (2.27)$$

The classical energy of a single-mode field is determined by its Hamiltonian, and with Equations (2.26) and (2.27) we can calculate that the classical field energy takes the form of a harmonic oscillator of unit mass

$$\begin{aligned} H &= \frac{1}{2} \int \left[ \epsilon_0 \mathbf{E}^2(\mathbf{r}, t) + \frac{1}{\mu_0} \mathbf{B}^2(\mathbf{r}, t) \right] dV \\ &= \frac{1}{2} (P^2 + \omega^2 Q^2), \end{aligned} \quad (2.28)$$

where the electric and magnetic fields correspond to the canonical position  $Q$  and momentum  $P = \dot{Q}$ .

To carry out the quantization, we replace the canonical variables by operators, denoted by a hat,

$$\begin{aligned} Q &\rightarrow \hat{Q}, \\ P &\rightarrow \hat{P} \end{aligned}$$

and assume that they obey the Bosonic commutation relation

$$\begin{aligned} [\hat{Q}_j, \hat{P}_{j'}] &= i\hbar \delta_{jj'} \hat{1} \rightarrow i\hbar \delta_{jj'}, \\ [\hat{Q}_j, \hat{Q}_{j'}] &= [\hat{P}_j, \hat{P}_{j'}] = 0. \end{aligned} \quad (2.29)$$

The commutator is defined as

$$[\hat{A}, \hat{B}] = \hat{A}\hat{B} - \hat{B}\hat{A} = \hat{C}$$

and leads to Heisenberg's Uncertainty Principle [50]. This states that two non-commuting canonical variables, i.e.  $\hat{C} \neq 0$ , cannot be measured simultaneously to an arbitrary precision. The measurement of one variable is restricted by the knowledge of the other through the product of their standard deviations

$$\Delta_s \hat{A} \cdot \Delta_s \hat{B} \geq \frac{1}{2} |\langle \hat{C} \rangle|, \quad (2.30)$$

where the standard deviation  $\Delta_s$  is defined as the square root of the variance

$$\Delta_s \hat{A} = \sqrt{\langle (\Delta \hat{A})^2 \rangle} = \sqrt{\langle \hat{A}^2 \rangle - \langle \hat{A} \rangle^2}. \quad (2.31)$$

For the canonical position and momentum we obtain the famous deviation product

$$\Delta_s \hat{Q} \cdot \Delta_s \hat{P} \geq \frac{\hbar}{2}.$$

For simplicity, we drop the identity operator  $\hat{\mathbb{1}}$  in Equation (2.29) and introduce the annihilation and creation operators

$$\hat{a} = \frac{1}{\sqrt{2\hbar\omega}} (\omega\hat{Q} + i\hat{P}) , \quad (2.32)$$

$$\hat{a}^\dagger = \frac{1}{\sqrt{2\hbar\omega}} (\omega\hat{Q} - i\hat{P}) . \quad (2.33)$$

Regarding Equation (2.29), they satisfy the commutation relation

$$[\hat{a}, \hat{a}^\dagger] = 1 \quad (2.34)$$

and the Hamiltonian of the electric field takes the form

$$\hat{H} = \hbar\omega \left( \hat{a}^\dagger \hat{a} + \frac{1}{2} \right) .$$

Replacing the canonical variables in Equations (2.26) and (2.27) by operators, the electromagnetic field is described by

$$\begin{aligned} \hat{E}_x(z, t) &= \mathcal{E}_0 (\hat{a}^\dagger + \hat{a}) \sin(kz) , \\ \hat{B}_y(z, t) &= i\mathcal{B}_0 (\hat{a}^\dagger - \hat{a}) \cos(kz) , \end{aligned}$$

where  $\mathcal{E}_0 = \sqrt{\hbar\omega/\epsilon_0 V}$  and  $\mathcal{B}_0 = \mu_0/k \cdot \sqrt{\epsilon_0 \hbar\omega^3/V}$  represent the electric and magnetic field amplitude, respectively.

So far we have considered the quantization of the one-mode radiation field in a finite one-dimensional cavity. We shall now review the quantization of the multi-mode field in a traveling-wave cavity. By the same approach, we take the classical electric and magnetic field in its traveling-wave solution

$$\begin{aligned} \mathbf{E}(\mathbf{r}, t) &= \sum_{\mathbf{k}} \mathbf{e}_{\mathbf{k}} \mathcal{E}_{\mathbf{k}} \left( \alpha_{\mathbf{k}} e^{-i(\omega_{\mathbf{k}} t - \mathbf{k} \cdot \mathbf{r})} + \alpha_{\mathbf{k}}^* e^{+i(\omega_{\mathbf{k}} t - \mathbf{k} \cdot \mathbf{r})} \right) , \\ \mathbf{B}(\mathbf{r}, t) &= \sum_{\mathbf{k}} \frac{\mathbf{k} \times \mathbf{e}_{\mathbf{k}}}{\omega_{\mathbf{k}}} \mathcal{E}_{\mathbf{k}} \left( \alpha_{\mathbf{k}} e^{-i(\omega_{\mathbf{k}} t - \mathbf{k} \cdot \mathbf{r})} + \alpha_{\mathbf{k}}^* e^{+i(\omega_{\mathbf{k}} t - \mathbf{k} \cdot \mathbf{r})} \right) \end{aligned}$$

with the dimensionless complex field amplitude  $\alpha_{\mathbf{k}}$ , the wave vector  $\mathbf{k}$ , the unit polarization vector  $\mathbf{e}_{\mathbf{k}}$  and the field constant  $\mathcal{E}_{\mathbf{k}} = \sqrt{\hbar\omega_{\mathbf{k}}/2\epsilon_0 V}$ . They also obey Maxwell's Equations (2.1) and from Equation (2.1a) it follows that  $\mathbf{k} \cdot \mathbf{e}_{\mathbf{k}} = 0$ , i.e. the field is purely transverse and there exist two independent polarization directions of  $\mathbf{e}_{\mathbf{k}}$  for each propagation direction  $\mathbf{k}$ .

The quantization is carried out as before: we replace the complex field amplitudes  $\alpha_{\mathbf{k}}$  and  $\alpha_{\mathbf{k}}^*$  by the annihilation and creation operators  $\hat{a}$  and  $\hat{a}^\dagger$ , respectively. Thus, the

quantized free electric and magnetic fields take the form

$$\begin{aligned}\hat{\mathbf{E}}(\mathbf{r}, t) &= \sum_{\mathbf{k}} \mathbf{e}_{\mathbf{k}} \mathcal{E}_{\mathbf{k}} \left( \hat{a}_{\mathbf{k}} e^{-i(\omega_{\mathbf{k}} t - \mathbf{k} \cdot \mathbf{r})} + \hat{a}_{\mathbf{k}}^{\dagger} e^{+i(\omega_{\mathbf{k}} t - \mathbf{k} \cdot \mathbf{r})} \right), \\ \hat{\mathbf{B}}(\mathbf{r}, t) &= \sum_{\mathbf{k}} \frac{\mathbf{k} \times \mathbf{e}_{\mathbf{k}}}{\omega_{\mathbf{k}}} \mathcal{E}_{\mathbf{k}} \left( \hat{a}_{\mathbf{k}} e^{-i(\omega_{\mathbf{k}} t - \mathbf{k} \cdot \mathbf{r})} + \hat{a}_{\mathbf{k}}^{\dagger} e^{+i(\omega_{\mathbf{k}} t - \mathbf{k} \cdot \mathbf{r})} \right).\end{aligned}\quad (2.35)$$

In free space, we must replace the sum by an integral:  $\sum_{\mathbf{k}} \rightarrow \frac{1}{\Delta\omega} \int d\omega$  and  $\hat{a}_{\mathbf{k}} \rightarrow \sqrt{\Delta\omega} \hat{a}_{\omega}$  with  $\Delta\omega = \frac{2\pi c}{L} \rightarrow 0$ .

### 2.3 Eigenstates of the Harmonic Oscillator

The eigenstates of the harmonic oscillator Equation (2.28) are called *Fock* or *number states*,  $|n\rangle$ . They are defined by the energy eigenvalue equation

$$\hat{H} |n\rangle = \hbar\omega \left( \hat{a}^{\dagger} \hat{a} + \frac{1}{2} \right) |n\rangle = E_n |n\rangle, \quad (2.36)$$

with the eigenenergy  $E_n$ . The operator product  $\hat{a}^{\dagger} \hat{a}$  takes a special role and we call it the number operator,  $\hat{n}$ . To see why, we examine the effect of the annihilation and creation operators from Equations (2.32) and (2.33) on Equation (2.36). Multiplying the creation operator from the left side leads, under consideration of the commutation relation Equation (2.34), to the expression

$$\hbar\omega \left( \hat{a}^{\dagger} \hat{a} + \frac{1}{2} \right) (\hat{a}^{\dagger} |n\rangle) = (E_n + \hbar\omega) (\hat{a}^{\dagger} |n\rangle). \quad (2.37)$$

Thus, the creation operator “creates” an energy quantum  $\hbar\omega$ . If we do the same for the annihilation operator, we see that one energy quantum is destroyed. If we apply the annihilation operator several times, we decrease the energy eigenvalues by integer multiples of  $\hbar\omega$ . Since the Hamiltonian is positive definite, the eigenenergies need to be positive and we will reach the lowest energy level  $E_0 > 0$  at a point such that

$$\hat{H} (\hat{a} |0\rangle) = (E_0 - \hbar\omega) (\hat{a} |0\rangle) = 0,$$

with  $\hat{a} |0\rangle = 0$ . The corresponding eigenstate is called the *vacuum state*  $|0\rangle$ , because it does not contain any mode quanta. The eigenvalue relation for the vacuum state is then

$$\hat{H} |0\rangle = \hbar\omega \left( \hat{a}^{\dagger} \hat{a} + \frac{1}{2} \right) |0\rangle = \frac{1}{2} \hbar\omega |0\rangle.$$

This lowest energy eigenvalue  $\hbar\omega/2$  is called the *zero-point energy* and defines with Equation (2.37) all other energies of the harmonic oscillator

$$E_n = \hbar\omega \left( n + \frac{1}{2} \right), \quad n \in \mathbb{N}.$$

Thus, the number operator  $\hat{n} = \hat{a}^\dagger \hat{a}$  returns the state's number of quanta

$$\hat{n} |n\rangle = n |n\rangle .$$

In conclusion, the eponymous effects of the creation  $\hat{a}^\dagger$  and annihilation  $\hat{a}$  operators on Fock states are

$$\begin{aligned} \hat{a}^\dagger |n\rangle &= \sqrt{n+1} |n+1\rangle , \\ \hat{a} |n\rangle &= \sqrt{n} |n-1\rangle , \\ \hat{a}^\dagger \hat{a} |n\rangle &= n |n\rangle \end{aligned}$$

and hence any Fock state can be obtained by repeated application of the creation operator to the vacuum state

$$|n\rangle = \frac{(\hat{a}^\dagger)^n}{\sqrt{n!}} |0\rangle .$$

Since the Fock states  $|n\rangle$  form a complete orthonormal basis

$$\begin{aligned} \langle n | n' \rangle &= \delta_{nn'} , \\ \sum_{n=0}^{\infty} |n\rangle \langle n| &= \hat{\mathbb{1}} , \end{aligned}$$

every arbitrary state can be expressed in the Fock basis.

## 2.4 Description of States by Quadrature Operators

To describe light fields quantum mechanically, it is convenient to go back to the position and momentum operators from Equations (2.32) and (2.33) and introduce the dimensionless operators

$$\begin{aligned} \hat{x} &= \frac{1}{2} (\hat{a}^\dagger + \hat{a}) = \sqrt{\frac{\omega}{2\hbar}} \cdot \hat{Q} , \\ \hat{p} &= \frac{i}{2} (\hat{a}^\dagger - \hat{a}) = \frac{1}{\sqrt{2\hbar\omega}} \cdot \hat{P} , \end{aligned} \tag{2.38}$$

which represent the amplitude and phase quadrature of the electric field. They obey the commutation relation

$$[\hat{x}, \hat{p}] = \frac{i}{2} \tag{2.39}$$

and the standard deviation product gives the uncertainty

$$\Delta_s \hat{x} \cdot \Delta_s \hat{p} \geq \frac{1}{4} . \tag{2.40}$$

We can rewrite the Hamiltonian of the harmonic oscillator as

$$\hat{H} = \hbar\omega \left( \hat{n} + \frac{1}{2} \right) = \hbar\omega (\hat{x}^2 + \hat{p}^2)$$

and see that the continuous quadrature operators are related to the discrete number operator. Wave and particle properties of a quantum are described by the same Hamiltonian.

### 2.4.1 Vacuum States

The vacuum state  $|0\rangle$  takes a special role in quantum mechanics. If we consider an arbitrary quadrature

$$\hat{x}^\theta = \frac{1}{2} (\hat{a}e^{-i\theta} + \hat{a}^\dagger e^{i\theta}) = \hat{x} \cos \theta + \hat{p} \sin \theta \quad (2.41)$$

of the vacuum state, we find that although the expectation value vanishes

$$\langle \hat{x}^\theta \rangle = \left\langle 0 \left| \frac{1}{2} (\hat{a}e^{-i\theta} + \hat{a}^\dagger e^{i\theta}) \right| 0 \right\rangle = 0,$$

the variance gives non-zero fluctuation contributions

$$\langle (\Delta \hat{x}^\theta)^2 \rangle_0 = \langle (\Delta \hat{x})^2 \rangle_0 = \langle (\Delta \hat{p})^2 \rangle_0 = \frac{1}{4}. \quad (2.42)$$

Individual measurements can return non-zero values of the field, despite there being no quanta in the mode. That means even the vacuum state is subject to Heisenberg's Uncertainty Principle. Since the variances of amplitude and phase quadrature are minimal according to Equation (2.40), we speak about a *vacuum noise limited* state.

The existence of such vacuum fluctuations has extensive consequences. For example, spontaneous emission in atomic systems can be seen as a vacuum noise stimulated emission. Also quantum optics experiments are limited by vacuum fluctuations, i.e. they couple into the experiment wherever optical losses are present.

### 2.4.2 Coherent States

To describe laser light, it is convenient to use the concept of coherent states  $|\alpha\rangle$ , which were introduced by Roy Glauber in 1963 [46]. It utilizes a vacuum state that is displaced by a coherent amplitude  $\alpha$  in phase space and hence exhibits the same noise properties.

The displacement operator is given by

$$\hat{D}(\alpha) = e^{\alpha \hat{a}^\dagger - \alpha^* \hat{a}}$$

and defines the coherent state in the Fock basis as

$$\begin{aligned}
 |\alpha\rangle &= \hat{D}(\alpha) |0\rangle \\
 &= e^{-\frac{1}{2}|\alpha|^2} \sum_{n=0}^{\infty} \frac{\alpha^n}{\sqrt{n!}} |n\rangle \\
 &= e^{-\frac{1}{2}|\alpha|^2} \sum_{n=0}^{\infty} \frac{\alpha^n}{n!} (\hat{a}^\dagger)^n |0\rangle.
 \end{aligned} \tag{2.43}$$

If we apply the annihilation operator to Equation (2.43) we see that coherent states are eigenstates of the annihilation operator

$$\hat{a} |\alpha\rangle = \alpha |\alpha\rangle$$

and describe a minimal uncertainty state, i.e. it is vacuum noise limited

$$\langle(\Delta\hat{x})^2\rangle_\alpha = \langle(\Delta\hat{p})^2\rangle_\alpha = \frac{1}{4}.$$

This corresponds to the definition: we displace a vacuum state and maintain its noise properties. Formally, coherent states are over-complete

$$\int |\alpha\rangle\langle\alpha| \frac{d\alpha}{\pi} = \mathbb{1}.$$

Although they are not orthogonal

$$\langle\alpha|\beta\rangle = e^{-|\alpha-\beta|^2},$$

the scalar product is vanishingly small for sufficiently different coherent amplitudes and we can regard them as being orthogonal.

The probability to detect  $n$  photons in a measurement follows the classical Poisson distribution

$$P_n = |\langle n|\alpha\rangle|^2 = e^{-|\alpha|^2} \frac{|\alpha|^{2n}}{n!},$$

where the mean photon number and variance are identical:

$$\langle n\rangle_\alpha = \langle(\Delta\hat{n})^2\rangle_\alpha = |\alpha|^2.$$

Furthermore the ratio of photon number fluctuation to mean photon number decreases with growing photon number

$$\frac{\Delta n}{\langle n\rangle} = \frac{1}{\sqrt{\langle n\rangle}}.$$

In the limit for large  $\langle n\rangle$  it reaches the classical approximation  $\frac{\Delta n}{\langle n\rangle} \rightarrow 0$ .

In agreement with the classical theory, the expectation value of the electric field from Equation (2.35) returns the classical expression

$$\begin{aligned}\langle \hat{\mathbf{E}}(\mathbf{r}, t) \rangle_\alpha &= \langle \alpha | \sum_{\mathbf{k}} \mathbf{e}_{\mathbf{k}} \mathcal{E}_{\mathbf{k}} \left( \hat{a}_{\mathbf{k}} e^{-i(\omega_{\mathbf{k}} t - \mathbf{k} \cdot \mathbf{r})} + \hat{a}_{\mathbf{k}}^\dagger e^{+i(\omega_{\mathbf{k}} t - \mathbf{k} \cdot \mathbf{r})} \right) | \alpha \rangle \\ &= \sum_{\mathbf{k}} \mathbf{e}_{\mathbf{k}} \mathcal{E}_{\mathbf{k}} \left( \alpha_{\mathbf{k}} e^{-i(\omega_{\mathbf{k}} t - \mathbf{k} \cdot \mathbf{r})} + \alpha_{\mathbf{k}}^* e^{+i(\omega_{\mathbf{k}} t - \mathbf{k} \cdot \mathbf{r})} \right).\end{aligned}$$

### 2.4.3 Squeezed States

Vacuum and coherent states represent special cases within the class of minimal uncertainty states, since their fluctuations are distributed equally in both quadratures  $\langle (\Delta \hat{x})^2 \rangle = \langle (\Delta \hat{p})^2 \rangle = \frac{1}{4}$ . More generally, however, are the so-called *squeezed states*. Their fluctuations are unequally distributed in different quadratures and the noise in one quadrature can drop below the noise of the vacuum state. To obey Heisenberg's Uncertainty Principle, Equation (2.30), the noise in the orthogonal quadrature must be larger than the vacuum noise

$$\langle (\Delta \hat{x})^2 \rangle = \frac{1}{16 \langle (\Delta \hat{p})^2 \rangle}, \quad (2.44)$$

while the product of the variances still describes a state of minimal uncertainty.

To obtain a squeezed state formally, we need to introduce the squeezing operator

$$\hat{S}(\xi) = e^{\frac{1}{2}[\xi^* \hat{a}^2 - \xi \hat{a}^{\dagger 2}]}$$

with  $\xi = r e^{i\Theta}$ . The squeezing parameter is denoted by  $r \geq 0$  and  $0 \leq \Theta \leq 2\pi$  defines the squeezed quadrature angle. A squeezed vacuum state can be created by applying the squeezing operator to the vacuum state

$$|\xi\rangle = \hat{S}(\xi) |0\rangle.$$

The changed noise properties become obvious if we consider an amplitude squeezed state ( $\Theta = 0$ ) and look at the variances of the amplitude and phase quadratures

$$\begin{aligned}\langle (\Delta \hat{x})^2 \rangle_\xi &= \frac{1}{4} e^{-2r}, \\ \langle (\Delta \hat{p})^2 \rangle_\xi &= \frac{1}{4} e^{+2r}.\end{aligned}$$

The squeezing parameter  $r$  signifies the squeezing strength. It is evident that the noise of one quadrature decreases at the expense of the other.

However, in everyday laboratory work, it is more convenient to describe the strength of squeezing on a logarithmic scale, normalized to the vacuum noise. Therefore, we introduce the decibel (dB) of the variance

$$\text{Var}(\hat{x}^\theta) \text{ [dB]} = 10 \log_{10} \frac{\langle (\Delta \hat{x}^\theta)^2 \rangle_\xi}{\langle (\Delta \hat{x}^\theta)^2 \rangle_0} = 10 \log_{10} \frac{\langle (\Delta \hat{x}^\theta)^2 \rangle_\xi}{1/4}.$$



# CHAPTER 3

---

## Gaussian States

---

Throughout this thesis, we deal with Gaussian states of light. In this case, all coherent, squeezed and entangled fields can be described by continuous variables (CV) with Gaussian statistics. In this chapter we will review some useful concepts and descriptions of Gaussian CV states.

### 3.1 Gaussian States Described by the Wigner Function

In classical optics the electromagnetic field is completely described by the statistics of the classical amplitude  $\alpha$ . We introduce a phase space distribution  $P(\alpha = q + ip)$ , which quantifies the probability of finding a particular pair of position and momentum components. Knowing this phase space distribution enables us to predict all statistical quantities of the electromagnetic field.

In quantum physics the situation is slightly different. Due to Heisenberg's Uncertainty Principle, we can neither measure position and momentum precisely at the same time nor predict them. However, we can use a probability distribution to describe the properties of quantum states in a classical-like fashion.

The most intuitive representation for our purpose is the Wigner function. It was introduced by Eugene Wigner in 1932 in his paper "On the quantum correction for thermodynamic equilibrium" [51]. Although the Wigner function can become negative, we are able to use it to predict the statistics of quantum observations. Hence, we will treat it as a quasi-probability distribution.

We wish to describe the quantum effects on quadrature observables. Therefore, we consider the phase space spanned by the amplitude quadrature  $x$  and phase quadrature

$p$ . For simplicity, we restrict ourselves to the one-mode case and obtain the Wigner function

$$W(x, p) = \frac{1}{\pi} \int \left\langle x - \frac{\zeta}{2} \left| \hat{\rho} \right| x + \frac{\zeta}{2} \right\rangle e^{2ip\zeta} d\zeta,$$

where  $\hat{\rho}$  describes the density matrix of an arbitrary quantum state. Treating this as a joint probability distribution for  $x$  and  $p$  yields some useful properties. The marginal distributions

$$\begin{aligned} \int W(x, p) dp &= \langle x | \hat{\rho} | x \rangle, \\ \int W(x, p) dx &= \langle p | \hat{\rho} | p \rangle \end{aligned} \quad (3.1)$$

correspond to the projection of the Wigner function onto the quadrature axes and return the amplitude and phase probabilities, respectively. The Wigner function is real

$$W^*(x, p) = W(x, p)$$

for Hermitian operators  $\hat{\rho}$  and normalized

$$\iint W(x, p) dx dp = 1.$$

The purity  $\text{tr}(\hat{\rho}^2)$  – as a measure of the state’s mixedness which ranges between zero and unity (pure state) – is expressed through the Wigner function by

$$\text{tr}(\hat{\rho}^2) = \pi \iint (W(x, p))^2 dx dp. \quad (3.2)$$

Further details can be found in many quantum optics text books. The description in this section is based upon [52, 53].

### Multimode Gaussian States

Since any Gaussian state can be described by its mean value and its variance, it is convenient to express the Wigner function by these properties. According to [14] for a multimode state it reads

$$W(\xi) = \frac{1}{(2\pi)^N \sqrt{\det \gamma^{(N)}}} \exp \left\{ -\frac{1}{2} (\xi - \mu) [\gamma^{(N)}]^{-1} (\xi - \mu)^T \right\},$$

where  $\xi$  and  $\mu$  are  $2N$ -dimensional vectors.  $\xi$  contains the quadrature pairs  $x_i, p_i$  of all  $N$  modes and  $\mu$  contains the corresponding mean values, which describe the state’s displacement:

$$\begin{aligned} \xi &= (x_1, p_1, x_2, p_2, \dots, x_N, p_N), \\ \mu &= (x_{1,0}, p_{1,0}, x_{2,0}, p_{2,0}, \dots, x_{N,0}, p_{N,0}). \end{aligned}$$

The  $2N \times 2N$  matrix  $\gamma^{(N)}$  represents the covariance matrix. It describes the correlations between the state's modes. Its elements are the symmetrized second moments according to the Weyl correspondence [52]

$$\begin{aligned} \text{tr} \left[ \hat{\rho} (\Delta \hat{\xi}_i \Delta \hat{\xi}_j + \Delta \hat{\xi}_j \Delta \hat{\xi}_i) / 2 \right] &= \langle (\hat{\xi}_i \hat{\xi}_j + \hat{\xi}_j \hat{\xi}_i) / 2 \rangle \\ &= \int W(\xi) \xi_i \xi_j d^{2N} \xi \\ &= \gamma_{ij}^{(N)}, \end{aligned} \quad (3.3)$$

where  $\Delta \hat{\xi}_i = \hat{\xi}_i - \langle \hat{\xi}_i \rangle = \hat{\xi}_i$  because we extracted the mean value into the vector  $\mu$ . For Gaussian states the noise properties and correlations are completely determined by the second-order covariance matrix  $\gamma_{ij}^{(N)}$ . It is real, symmetric and its eigenvalues are non-negative

$$\gamma^{(N)} = \left( \gamma^{(N)} \right)^* , \quad \gamma^{(N)} = \left( \gamma^{(N)} \right)^T , \quad \text{eig} \left( \gamma^{(N)} \right) \geq 0 .$$

The normalization is in agreement with Equation (2.42), such that the covariance matrix of a vacuum state is given by  $\gamma_{ij}^{(N)} = 1/4 \delta_{ij}$ , with  $\delta_{ij}$  the Kronecker delta. Since its entries are the quadrature operators, they must obey their commutation relation, Equation (2.39). For the  $2N$ -dimensional case we can write it compactly as [54]

$$[\hat{\xi}_k, \hat{\xi}_l] = \frac{i}{2} \Lambda_{kl} ,$$

where the  $2N \times 2N$  matrix  $\Lambda$  consists of the  $2 \times 2$  matrix  $\sigma$  as diagonal elements for each quadrature pair

$$\Lambda := \bigoplus_{k=1}^N \sigma = \begin{pmatrix} \sigma & & \\ & \ddots & \\ & & \sigma \end{pmatrix} , \quad \sigma := \begin{pmatrix} 0 & 1 \\ -1 & 0 \end{pmatrix} .$$

As for the one-mode case, the  $N$ -mode state is subject to an uncertainty relation. The compact notation of Heisenberg's Uncertainty Relation for  $N$  modes reads [54]

$$B(\gamma) = \min \text{eig} \left( \gamma^{(N)} + \frac{i}{4} \Lambda \right) \geq 0 . \quad (3.4)$$

For a state of minimal uncertainty,  $B(\gamma)$  is zero. If it is negative, the covariance matrix does not represent a physical state – it is not *bona fide*.

Since  $\gamma$  is real, the complex conjugate is an equivalent description. In a common abbreviated notation, the positive semi-definiteness (minimum eigenvalue) is implied and it reads

$$B(\gamma) = \gamma^{(N)} \pm \frac{i}{4} \Lambda \geq 0 .$$

To avoid confusion we will stick to the long version throughout this thesis.

### 3.1.1 Examples of Wigner Functions

We consider the case of the two-dimensional phase space,  $N = 1$ . The quadrature operator reduces to  $\hat{\xi} = (\hat{x}, \hat{p})$  and the Wigner function becomes

$$W(x, p) = \frac{1}{2\pi\sqrt{\det \gamma}} \exp \left\{ -\frac{1}{2} \begin{pmatrix} x - x_0 \\ p - p_0 \end{pmatrix}^T \begin{pmatrix} \gamma_{11} & \gamma_{12} \\ \gamma_{21} & \gamma_{22} \end{pmatrix}^{-1} \begin{pmatrix} x - x_0 \\ p - p_0 \end{pmatrix} \right\}.$$

#### The Coherent State

A coherent state corresponds to a displaced vacuum state. Hence, the covariance matrix is equivalent to  $\gamma_{ij} = 1/4 \delta_{ij}$  and the vector  $\mu = (x_0, p_0)$  defines the displacement. Keeping in mind that

$$\gamma^{-1} = \frac{1}{\det \gamma} \begin{pmatrix} \gamma_{22} & -\gamma_{12} \\ -\gamma_{21} & \gamma_{11} \end{pmatrix} = 4 \begin{pmatrix} 1 & 0 \\ 0 & 1 \end{pmatrix},$$

gives the Wigner function for a coherent state

$$W(x, p) = \frac{2}{\pi} \exp \left\{ -2 \left( (x - x_0)^2 + (p - p_0)^2 \right) \right\}.$$

Figure 3.1 shows an example with displacement  $\mu = (3, 0)$ . The red traces depict the marginal distributions. They are projections of the Wigner function onto the  $x$  and  $p$  axes and correspond to the amplitude and phase probabilities, according to Equation (3.1). Their variances are  $1/4$  for the coherent state.

#### The Squeezed State

According to Equation (3.3), the entries of the covariance matrix for an amplitude squeezed state are the squeezed and anti-squeezed variances of both quadratures on its main diagonal. The secondary diagonal vanishes due to the anti-symmetric commutator of  $\hat{x}$  and  $\hat{p}$ , see Equation (2.39). For the amplitude squeezed state we get  $\langle (\Delta \hat{x})^2 \rangle = \frac{1}{4} e^{-2r} \equiv V_S$  and  $\langle (\Delta \hat{p})^2 \rangle = \frac{1}{4} e^{+2r} \equiv V_A$  and hence

$$\gamma = \begin{pmatrix} V_S & 0 \\ 0 & V_A \end{pmatrix}, \quad \gamma^{-1} = \begin{pmatrix} 1/V_S & 0 \\ 0 & 1/V_A \end{pmatrix}.$$

The resulting Wigner function for a displaced, amplitude squeezed state then reads

$$W(x, p) = \frac{1}{2\pi\sqrt{V_S V_A}} \exp \left\{ -\frac{(x - x_0)^2}{2V_S} - \frac{(p - p_0)^2}{2V_A} \right\}.$$

Figure 3.2 shows an example of a displaced amplitude squeezed state with a squeezing factor of  $-6$  dB.

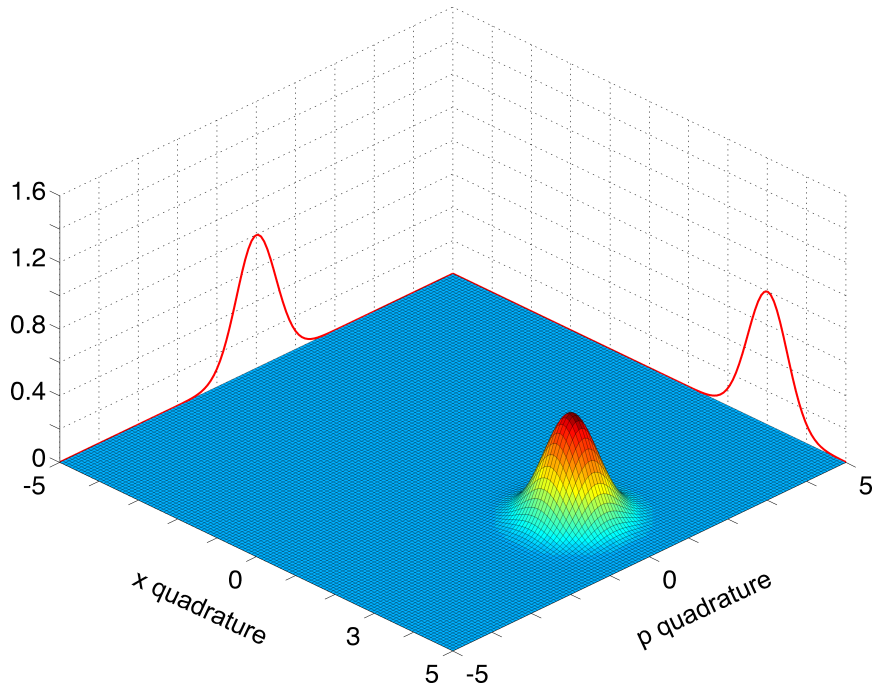


**Figure 3.1** – Wigner function of a coherent state with displacement  $\mu = (3, 0)$ . The red traces depict the marginal distributions.

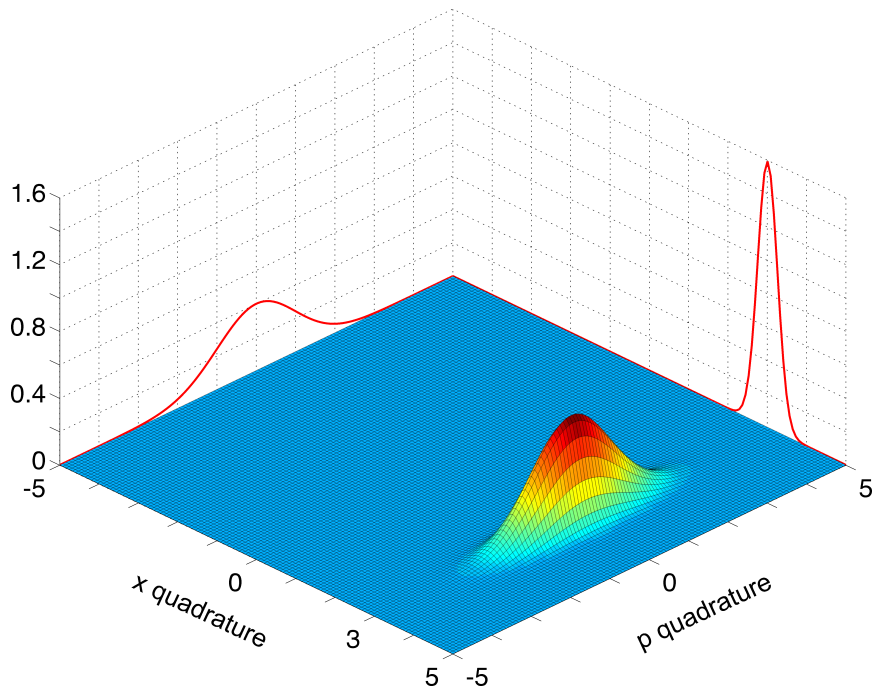


**Figure 3.2** – Wigner function of a  $-6$  dB amplitude squeezed state with coherent displacement  $\mu = (3, 0)$ . The red traces depict the marginal distributions.

## 3.2 Description of Linear Optics

In order to describe the preparation of a non-classical state we need not only the covariance matrix of the initial (squeezed) state but we must also describe the state's propagation through a set of linear optics. The most important linear optical components for (multimode) quantum networks are the phase shifter and the beam splitter. We will use them to generate particular quantum states.

### 3.2.1 The Phase Shifter

The phase shift has no physical meaning for a single mode on its own. It is usually defined with respect to a local oscillator, e.g. for homodyne detection (see Section 4.1), or with respect to another non-classical mode. A phase shift acting on a squeezed mode rotates its squeezing ellipse in phase space. Experimentally, this can be realized by simply changing the optical path length of the beam. The quadrature pair of the shifted mode transforms via the symplectic map  $\hat{\xi} \rightarrow \hat{R}(\theta)\hat{\xi}$ , while the covariance matrix transforms as  $\gamma^{(1)} \rightarrow \hat{R}\gamma^{(1)}\hat{R}^T$  with

$$\hat{R}(\theta) = \begin{pmatrix} \cos \theta & \sin \theta \\ -\sin \theta & \cos \theta \end{pmatrix}.$$

The phase shift angle  $\theta$  defines the state's rotation in phase space.

Introducing a phase shift to the covariance matrix of a  $-5$  dB amplitude squeezed field

$$\gamma_A^{(1)} = \begin{pmatrix} 0.08 & 0 \\ 0 & 0.8 \end{pmatrix} \quad (3.5)$$

such that the ellipse is rotated by  $45^\circ$  leads to the following covariance matrix

$$\begin{aligned} \gamma_{\pi/4}^{(1)} &= \hat{R}(\pi/4) \gamma_A^{(1)} \hat{R}^T(\pi/4) \\ &= \begin{pmatrix} 0.44 & 0.36 \\ 0.36 & 0.44 \end{pmatrix}. \end{aligned}$$

### Phase Shift of an $N$ -mode State

To shift the phase of the  $K^{\text{th}}$  mode in an  $N$ -mode state, the matrix is the direct sum of identities for the unchanged modes and the phase shift operation of the  $K^{\text{th}}$  mode:

$$\hat{R}_K^{(N)}(\theta) = \mathbb{1}_1 \oplus \dots \oplus \hat{R}_K(\theta) \oplus \dots \oplus \mathbb{1}_N.$$

### 3.2.2 The Beam Splitter

A common approach to generate entangled states is to interfere two squeezed beams with a phase shift of  $90^\circ$  at a beam splitter. The symplectic map of a beam splitter with power transmissivity  $\tau \in [0, 1]$  reads [55]

$$\hat{B}(\tau) = \begin{pmatrix} \sqrt{1-\tau} & 0 & \sqrt{\tau} & 0 \\ 0 & \sqrt{1-\tau} & 0 & \sqrt{\tau} \\ -\sqrt{\tau} & 0 & \sqrt{1-\tau} & 0 \\ 0 & -\sqrt{\tau} & 0 & \sqrt{1-\tau} \end{pmatrix}. \quad (3.6)$$

The quadrature pairs become  $\hat{\xi} \rightarrow \hat{B}(\tau)\hat{\xi}$  and the covariance matrix transforms as  $\gamma^{(2)} \rightarrow \hat{B}(\tau)\gamma^{(2)}\hat{B}^T(\tau)$ .

Interfering the  $-5$  dB amplitude squeezed state  $\gamma_A^{(1)}$  (Equation (3.5)) with a  $-5$  dB phase squeezed state  $\gamma_B^{(1)} = \hat{R}(\pi/2)\gamma_A^{(1)}\hat{R}^T(\pi/2)$  at a 50/50 beam splitter ( $\tau = 0.5$ ) leads to the covariance matrix of a two-mode squeezed (TMS) state:

$$\begin{aligned} \gamma_{\text{TMS}}^{(2)} &= \hat{B}(0.5) \left( \gamma_A^{(1)} \oplus \gamma_B^{(1)} \right) \hat{B}^T(0.5) \\ &= \begin{pmatrix} \frac{1}{\sqrt{2}} & 0 & \frac{1}{\sqrt{2}} & 0 \\ 0 & \frac{1}{\sqrt{2}} & 0 & \frac{1}{\sqrt{2}} \\ -\frac{1}{\sqrt{2}} & 0 & \frac{1}{\sqrt{2}} & 0 \\ 0 & -\frac{1}{\sqrt{2}} & 0 & \frac{1}{\sqrt{2}} \end{pmatrix} \begin{pmatrix} 0.08 & 0 & 0 & 0 \\ 0 & 0.8 & 0 & 0 \\ 0 & 0 & 0.8 & 0 \\ 0 & 0 & 0 & 0.08 \end{pmatrix} \begin{pmatrix} \frac{1}{\sqrt{2}} & 0 & -\frac{1}{\sqrt{2}} & 0 \\ 0 & \frac{1}{\sqrt{2}} & 0 & -\frac{1}{\sqrt{2}} \\ \frac{1}{\sqrt{2}} & 0 & \frac{1}{\sqrt{2}} & 0 \\ 0 & \frac{1}{\sqrt{2}} & 0 & \frac{1}{\sqrt{2}} \end{pmatrix} \\ &= \begin{pmatrix} 0.44 & 0 & 0.36 & 0 \\ 0 & 0.44 & 0 & -0.36 \\ 0.36 & 0 & 0.44 & 0 \\ 0 & -0.36 & 0 & 0.44 \end{pmatrix}. \end{aligned}$$

In Section 5.1.1 we will see that such an entangled state is called inseparable, since we cannot write the covariance matrix as the direct sum of its two subsystems  $\gamma_{\text{TMS}}^{(2)} \neq \gamma_A^{(1)} \oplus \gamma_B^{(1)}$ .

### Mixing Two Modes of an $N$ -mode State

If we want to overlap the two modes  $K$  and  $L$  of an  $N$ -mode state at a beam splitter, the matrix generalizes to:

$$\left( \hat{B}_{K,L}^{(N)} \right)_{i,j} = \begin{cases} \sqrt{1-\tau} \delta_{i,j} + \sqrt{\tau} \delta_{2K-i,2L-j} - \sqrt{\tau} \delta_{2L-i,2K-j} & i, j \in M \\ 1 \delta_{i,j} & i, j \in [1, 2N] \setminus M \end{cases}.$$

The set  $M = \{2K-1, 2K, 2L-1, 2L\}$  defines the matrix entries that are affected by the mixing. The other entries  $i, j \in [1, 2N] \setminus M$  correspond to the non-involved modes which remain unchanged.

### Optical Losses

Optical loss in quantum optics does not only mean a loss of signal amplitude but also an injection of vacuum noise into the system. This degrades the quality of the light's non-classical properties. Hence, any optical loss acts on the considered state as a mixture with the vacuum noise. This can be modeled by the beam splitter matrix from Equation (3.6). The transmissivity  $\tau$  corresponds to the optical loss and the second input mode is the vacuum state. Based on the complete two-mode relation

$$\gamma_{\text{mixed}}^{(2)} = \hat{B}(\tau) \left( \gamma_{\text{state}}^{(1)} \oplus \gamma_{\text{vacuum}}^{(1)} \right) \hat{B}^T(\tau)$$

we obtain the expression for the lossy signal state by just considering the state's mode

$$\gamma_{\text{lossy}}^{(1)} = (1 - \tau) \gamma_{\text{state}}^{(1)} + \tau \gamma_{\text{vacuum}}^{(1)}. \quad (3.7)$$

We will use this to manufacture squeezed states with well-defined quadrature noise, since the state's purity from Equation (3.2) is affected by optical losses. Hence, different squeezing and anti-squeezing values can be obtained.

To describe the total state preparation we simply multiply all occurring transformation matrices and apply them to the initial state.

### 3.3 Reconstruction of a State's Covariance Matrix

To characterize an experimentally generated Gaussian quantum state, it is convenient to reconstruct the state's covariance matrix. Its entries consist of the variance of each mode (\*), the covariance of the same quadrature of different modes (o), the covariance of different quadratures of different modes (•) and the covariance of different quadratures of the same mode (x), as depicted in Equation (3.8) for the two-mode case:

$$\gamma^{(2)} = \begin{pmatrix} * & \times & \circ & \bullet \\ & * & \bullet & \circ \\ & & * & \times \\ & & & * \end{pmatrix}. \quad (3.8)$$

Since the covariance matrix is symmetric, we simply need to consider the upper triangular matrix. By recording data sets from different quadrature measurements, we are able to calculate the variances (\*) and the covariances of different modes (o, •) directly. Since we cannot measure different quadratures of the same mode (x) at the same time due to Heisenberg's Uncertainty Relation, we need to reconstruct it by time correlation independent measurements.

The covariance matrix is fully determined by the state's second moments  $\hat{a}^2$ ,  $\hat{a}^{\dagger 2}$  and  $\hat{a}^{\dagger}\hat{a}$ ; so too are the correlations of different quadratures of the same mode (x).



Although we cannot measure the moments directly, we can reconstruct them by measuring quadrature variances. We choose three different quadratures, obtaining

$$4 \langle (\Delta \hat{x}(0))^2 \rangle = \langle \hat{a}^2 \rangle + \langle \hat{a}^{\dagger 2} \rangle + 2 \langle \hat{n} \rangle + 1, \quad (3.9)$$

$$4 \langle (\Delta \hat{x}(\pi/2))^2 \rangle = -\langle \hat{a}^2 \rangle - \langle \hat{a}^{\dagger 2} \rangle + 2 \langle \hat{n} \rangle + 1, \quad (3.10)$$

$$4 \langle (\Delta \hat{x}(\pi/4))^2 \rangle = -i \langle \hat{a}^2 \rangle + i \langle \hat{a}^{\dagger 2} \rangle + 2 \langle \hat{n} \rangle + 1 \quad (3.11)$$

from Equations (2.41), (2.31) and (2.34) and extract the second moments by linear combination of Equations (3.9), (3.10) and (3.11):

$$\begin{aligned} \frac{(3.9) + (3.10)}{2} &= 2 \langle \hat{n} \rangle + 1, \\ \frac{(3.9) - (3.10)}{2} &= \langle \hat{a}^2 \rangle + \langle \hat{a}^{\dagger 2} \rangle, \\ (3.11) - \frac{(3.9) + (3.10)}{2} &= -i \langle \hat{a}^2 \rangle + i \langle \hat{a}^{\dagger 2} \rangle. \end{aligned} \quad (3.12)$$

Using the Weyl correspondence from Equation (3.3) allows us to express the entries of the covariance matrix of different quadratures of the same mode ( $\times$ ) as

$$\gamma_{i,i+1}^{(N)} = \langle (\hat{\xi}_i \hat{\xi}_{i+1} + \hat{\xi}_{i+1} \hat{\xi}_i) / 2 \rangle, \quad \forall i \text{ odd}. \quad (3.13)$$

As an example we calculate the case for ( $\hat{\xi}_1 = \hat{x}_1, \hat{\xi}_2 = \hat{p}_1$ ):

$$\begin{aligned} \gamma_{1,2}^{(N)} &= \langle (\hat{\xi}_1 \hat{\xi}_2 + \hat{\xi}_2 \hat{\xi}_1) / 2 \rangle \\ &= \frac{1}{2} \left\langle \frac{1}{2} (\hat{a}^\dagger + \hat{a}) \frac{i}{2} (\hat{a}^\dagger - \hat{a}) + \frac{i}{2} (\hat{a}^\dagger - \hat{a}) \frac{1}{2} (\hat{a}^\dagger + \hat{a}) \right\rangle \\ &= \frac{1}{4} (i \langle \hat{a}^{\dagger 2} \rangle - i \langle \hat{a}^2 \rangle). \end{aligned}$$

Thus, the correlations between a mode's amplitude and phase quadrature ( $\times$ ) can be expressed through a measurement of three quadrature variances, according to Equation (3.12). Provided that the prepared state does not vary in time, we are able to reconstruct its covariance matrix. In Chapter 5 we will discuss the required measurements and reconstruct the  $8 \times 8$  covariance matrix of a bound entangled state of light.

### 3.4 Verifying Gaussianity

Some criteria used within this thesis are valid only for Gaussian states. Although the physical mechanisms of the setups used are solely based on Gaussian operations,

unstable control loops or beam fluctuations could introduce phase noise. This would lead to a non-Gaussian statistic. Therefore, we discuss some methods to confirm the Gaussianity of the considered states.

In the experiment the raw data of the homodyne detectors are recorded and analyzed. Here, we use simulated raw data, drawn from a Gaussian distribution and apply phase noise that is normally distributed. It is hence describable by its standard deviation  $\sigma$ :

$$\Phi(\theta) = \frac{1}{\sigma\sqrt{2\pi}} e^{-\frac{\theta^2}{2\sigma^2}} .$$

The state's Wigner function is affected by the phase jitter in the form [56]

$$W_{\Phi}(\xi') = \int W(\xi') \Phi(\theta) d\theta ,$$

where the elements of  $\xi'$  are rotated randomly

$$\begin{aligned} x'_i &= x_i \cos(\theta_i) + p_i \sin(\theta_i) , \\ p'_i &= p_i \cos(\theta_i) - x_i \sin(\theta_i) . \end{aligned}$$

The projection of the Wigner function onto one quadrature axis (see Equation (3.1)) corresponds to the data that is measured by the homodyne detector; it exhibits the phase noise.

By building a histogram of the raw data, a first estimate of the underlying statistics can be made. Figure 3.3 shows two histograms of simulated data: one pure Gaussian and one Gaussian with a phase noise of  $\sigma = 0.1$ . No significant deviation from a Gaussian is visible for small phase noise.

The cumulative distribution function (CDF) allows a closer look at the difference between the data and a perfect distribution. It cumulates the area under the probability distribution, i.e. the histogram:

$$\text{CDF}(x) = \int_{-\infty}^x f(t) dt .$$

The CDFs of the simulated data (black curves in Figure 3.4) appear to be identical with the CDF of a Gaussian distribution (red curve, left side). The difference of both (red curve, right side) unveils deviations. In the case without phase noise, the deviation occurs due to the limited sample size ( $4 \times 10^6$ ) and numerical errors. With the presence of phase noise, a clear signature becomes visible. Interestingly, this appears at the CDF's biggest slope, where numerical errors are more likely. To ensure that no other numerical artifacts spoil the analysis, another graphical test is used: the QQ-plot.

The QQ-plot compares a measured distribution to a Gaussian one. The sample quantiles of the measured data are plotted against the theoretical quantiles of a perfect

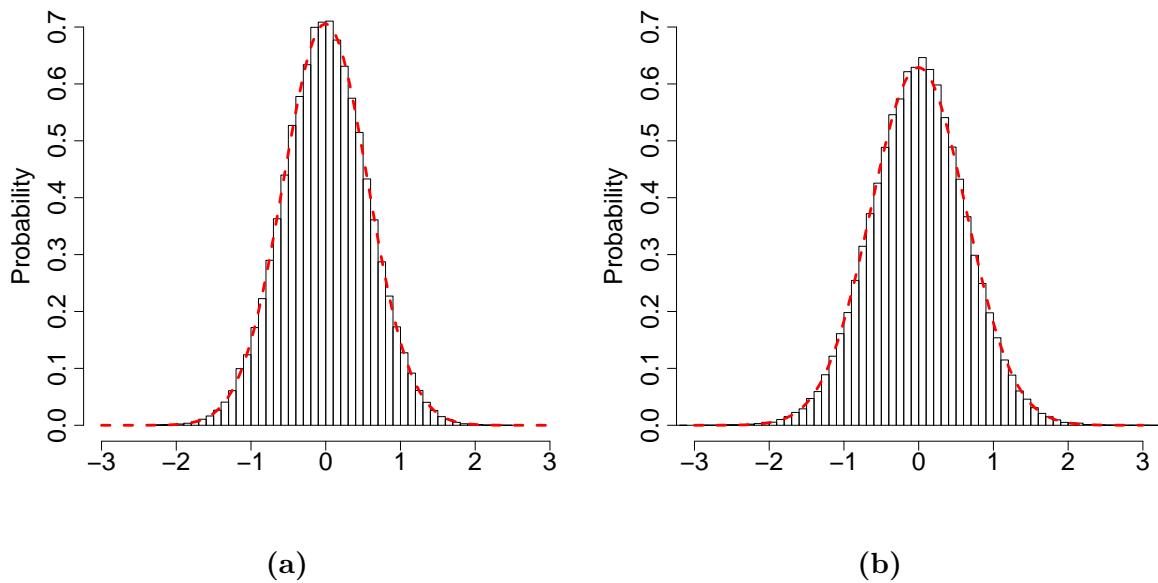
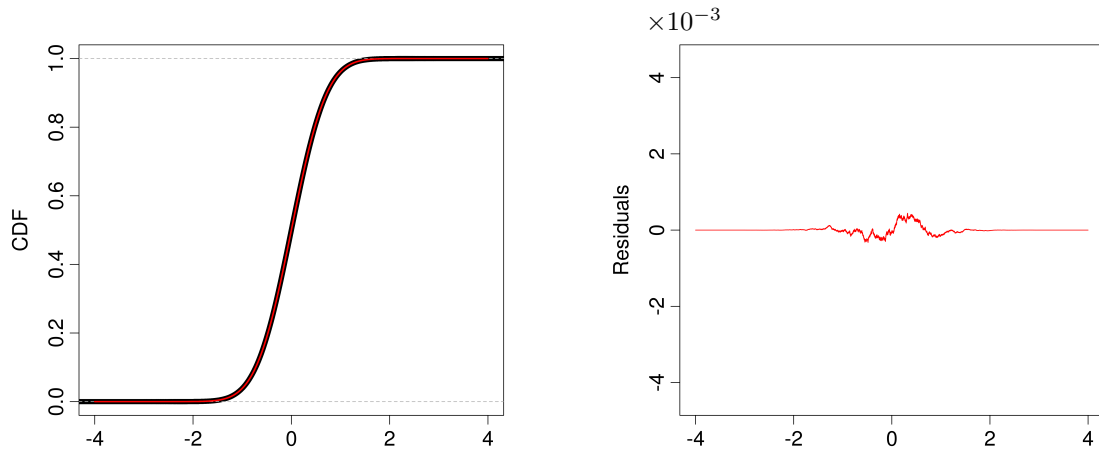


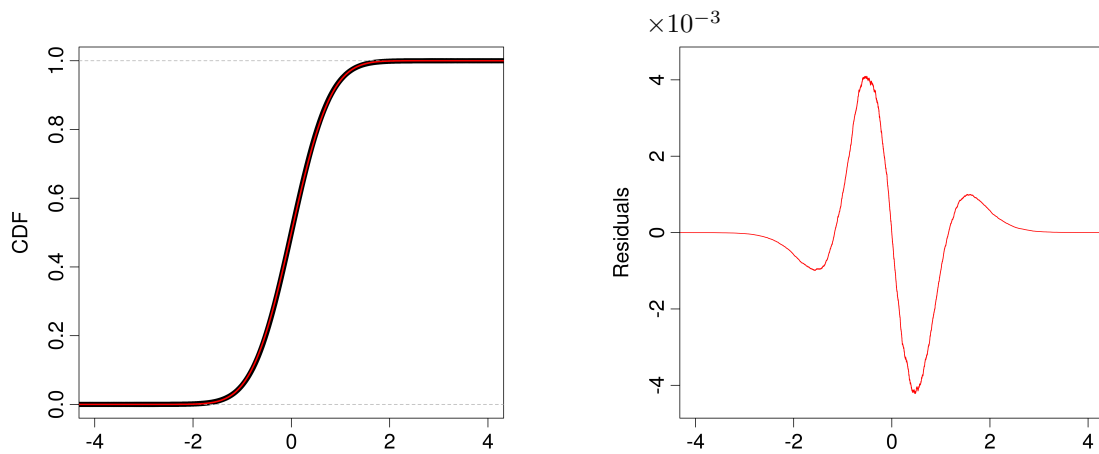
**Figure 3.3** – Histograms of simulated data without (a) and with (b) phase noise ( $\sigma = 0.1$ ). No significant deviation from a Gaussian fit (red) is visible.

Gaussian distribution. A perfect Gaussian distribution results in a straight line, while random numbers with a Gaussian statistic are distributed along that line, as shown for example in Figure 3.5a. Figure 3.5b shows the QQ-plot of the data with a phase noise of  $\sigma = 0.1$ . A clear deviation is visible and indicates a non-Gaussian statistic.

Small phase fluctuations can hence be unveiled by using graphical tests such as the CDF's residual or the QQ-plot.



(a) Simulated data drawn from a Normal distribution. No phase noise was introduced.



(b) Simulated data drawn from a Normal distribution with phase noise of  $\sigma = 0.1$ .

**Figure 3.4** – Cumulative distribution function (CDF) of simulated data without phase noise (left, black) and a perfect Gaussian CDF (left, red). The residuals (right) do not vanish due to limited sample size ( $4 \times 10^6$ ) and numerical errors (a). The deviation becomes significant with introduced phase noise ( $\sigma = 0.1$ ) (b).

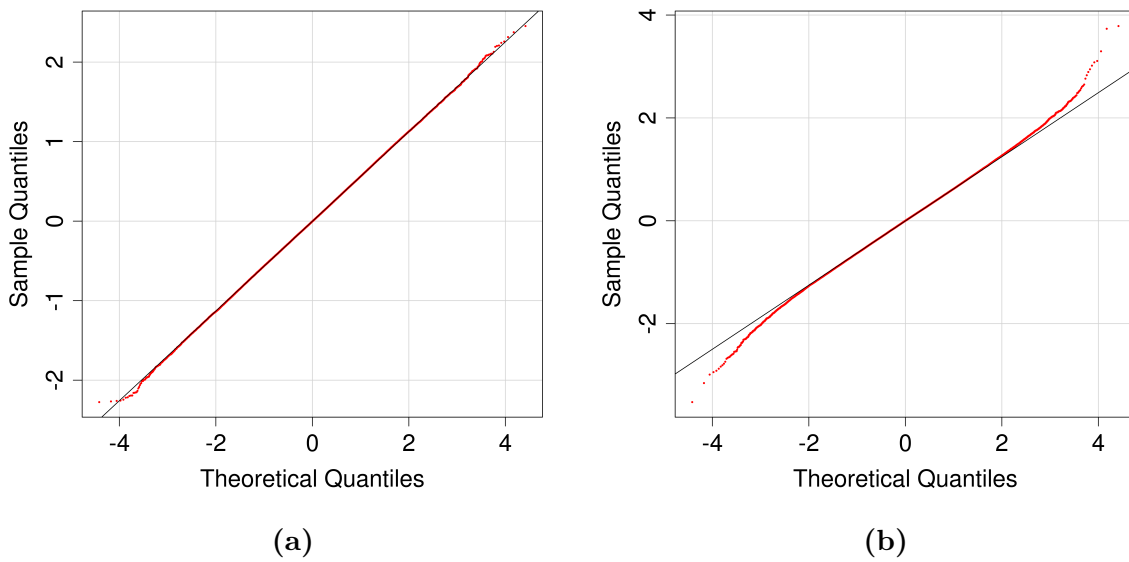


**Figure 3.5** – QQ-Plots of simulated data without (a) and with (b) phase noise ( $\sigma = 0.1$ ). A clear deviation from a Gaussian distribution (black line) is visible for the latter.



## CHAPTER 4

---

### Experimental Techniques

---

In this chapter we will review some experimental techniques that were used for conducting the experiments.

#### 4.1 Homodyne Detection

Homodyne detection is used to analyze the field fluctuation of a (quantum) state. With a *balanced homodyne detector* an arbitrary quadrature of the state is accessible. A simplified version is the *self homodyne detector*, which only allows observation of the fluctuations in the amplitude quadrature of a bright field.

##### Balanced Homodyne Detection

The principle of optical balanced homodyne detection was developed by Horace Yuen and Jeffrey Shapiro [57] in 1980: the signal field of interest ( $\hat{a}_{\text{sig}}$ ) is superimposed with a much stronger (at least an order of magnitude in intensity) optical local oscillator ( $\hat{a}_{\text{LO}}$ ) at a 50/50 beam splitter. The output fields ( $\hat{a}_{1,2}$ ) are detected with photo-detectors that measure the difference current, as shown in Figure 4.1. The observed quadrature is determined by the phase  $\theta$  between the two input fields.

According to the input/output relation of a beam splitter (Equation (C.1)), we

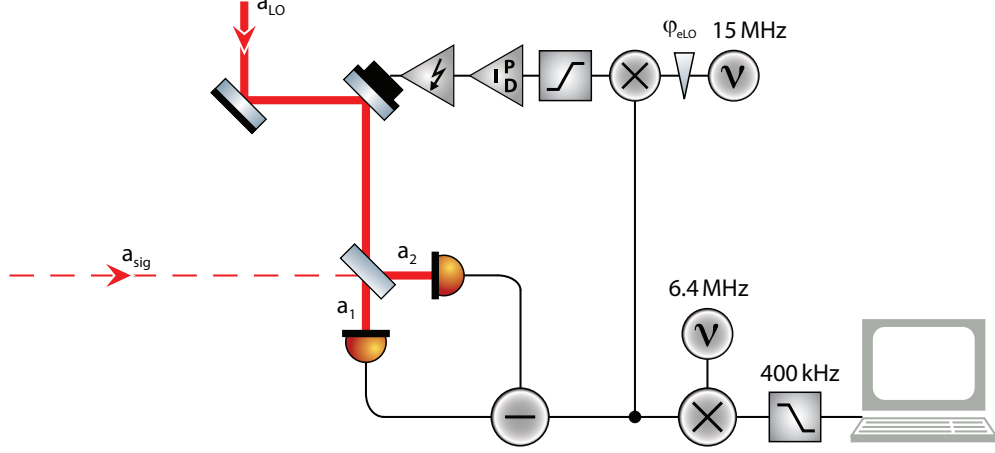


**Figure 4.1** – Schematic of a balanced homodyne detector, as used for analyzing the bound entangled states. It includes a phase control loop operating at a sideband frequency of 15 MHz and data acquisition at 6.4 MHz. The phase control loop is described in Section 4.2.

obtain for the output fields of the 50/50 beam splitter

$$\begin{aligned}\hat{a}_1 &= \frac{1}{\sqrt{2}} (\hat{a}_{\text{sig}} + e^{i\theta} \hat{a}_{\text{LO}}), \\ \hat{a}_2 &= \frac{1}{\sqrt{2}} (\hat{a}_{\text{sig}} - e^{i\theta} \hat{a}_{\text{LO}}).\end{aligned}$$

Writing the operators as a sum of their coherent amplitude and quantum fluctuations ( $\hat{a} = \alpha + \delta\hat{a}$ ), neglecting second order fluctuation products ( $\delta\hat{a} \cdot \delta\hat{b} \approx 0$ ) and assuming a perfect quantum efficiency of the photo-diodes ( $\eta_{\text{pd}} = 1$ ) we obtain the photo-currents

$$\begin{aligned}\hat{i}_{1,2} &\propto \hat{a}_{1,2}^\dagger \cdot \hat{a}_{1,2} \\ &= \frac{1}{2} [\hat{a}_{\text{sig}}^\dagger \pm e^{-i\theta} \hat{a}_{\text{LO}}^\dagger] [\hat{a}_{\text{sig}} \pm e^{i\theta} \hat{a}_{\text{LO}}] \\ &\approx \frac{1}{2} \left\{ |\alpha_{\text{sig}}|^2 + |\alpha_{\text{LO}}|^2 \pm 2\alpha_{\text{sig}}\alpha_{\text{LO}} \cos \theta \right. \\ &\quad \left. + \alpha_{\text{sig}} (\delta\hat{x}_{\text{sig}} \pm \delta\hat{x}_{\text{LO}}^{-\theta}) + \alpha_{\text{LO}} (\delta\hat{x}_{\text{LO}} \pm \delta\hat{x}_{\text{sig}}^\theta) \right\}.\end{aligned}\tag{4.1}$$

If we assume  $|\alpha_{\text{LO}}| \gg |\alpha_{\text{sig}}|$  we can neglect products containing only  $\alpha_{\text{sig}}$ . The difference of the photo-currents reads

$$\begin{aligned}\hat{i}_- &\propto 2\alpha_{\text{sig}}\alpha_{\text{LO}} \cos \theta + \alpha_{\text{sig}}\delta\hat{x}_{\text{LO}}^{-\theta} + \alpha_{\text{LO}}\delta\hat{x}_{\text{sig}}^\theta \\ &\approx 2\alpha_{\text{sig}}\alpha_{\text{LO}} \cos \theta + \alpha_{\text{LO}}\delta\hat{x}_{\text{sig}}^\theta.\end{aligned}$$



Considering the radio frequency (RF) spectrum

$$i_-(\omega, \theta) \propto \alpha_{\text{LO}} \langle \delta \hat{x}_{\text{sig}}^\theta(\omega) \rangle$$

we see that the signal is proportional to the quantum noise of quadrature  $\hat{x}_{\text{sig}}^\theta$ , scaled by the coherent amplitude of the LO. The phase  $\theta$  between the signal field and LO determines the observed quadrature. By stabilizing the phase to a certain value (as described in Section 4.2), the quantum noise of the desired quadrature can be recorded constantly.

### Self Homodyne Detection

Self homodyne detection is a simple scheme to analyze the amplitude fluctuations of a bright beam. By removing the local oscillator of a balanced homodyne detector, i.e. replacing it by a vacuum field, we obtain from Equation (4.1) for the single photo-detector currents

$$\begin{aligned} \hat{i}_{1,2} &\propto \hat{a}_{1,2}^\dagger \cdot \hat{a}_{1,2} \\ &\approx \frac{1}{2} \left[ |\alpha_{\text{sig}}|^2 + \alpha_{\text{sig}} (\delta \hat{x}_{\text{sig}} \pm \delta \hat{x}_{\text{vac}}) \right]. \end{aligned}$$

The sum of the photo-detector currents gives information about the fluctuations in the amplitude quadrature, while the difference results in the reference vacuum noise depending on the coherent amplitude  $\alpha_{\text{sig}}$ :

$$\begin{aligned} \hat{i}_+ &= |\alpha_{\text{sig}}|^2 + \alpha_{\text{sig}} \delta \hat{x}_{\text{sig}}, \\ \hat{i}_- &= \alpha_{\text{sig}} \delta \hat{x}_{\text{vac}}. \end{aligned}$$

Hence, no mode matching of the signal field and a local oscillator and no phase control loop is needed to compare the signal's amplitude noise with the vacuum fluctuation. This method was used in Chapter 6 to analyze the amplitude correlations of two bright twin beams.

## 4.2 Single Sideband Modulation – A Phase-Locking Scheme

To analyze a quantum state, it is necessary to stabilize the phase of a balanced homodyne detector to any quadrature at will. A convenient way to achieve this is to add a single sideband (outside the measurement band) to the signal field. This can either be achieved by amplitude and phase modulating the signal field or overlapping the signal field with a frequency-shifted field, e.g. introduced by an acousto-optical modulator (AOM) or by a second offset phase-locked laser. This corresponds to a

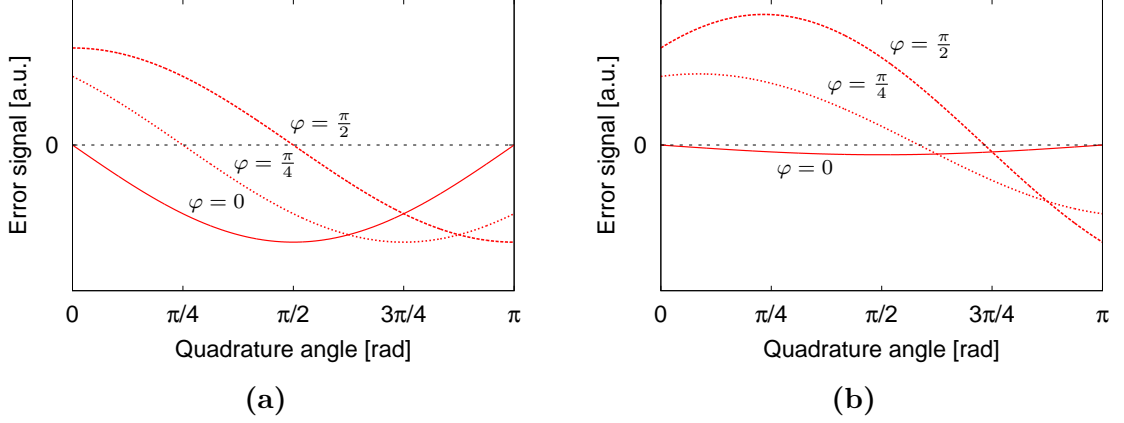


**Figure 4.2** – Error signal for balanced homodyne detectors and phase gates. (a) Correct error signal obtained from the difference of two photo-detectors. The eLO phase  $\varphi$  corresponds to the zero crossing at the desired quadrature angle. (b) Error signal obtained from only one photo-detector. The zero crossings do not correspond to the desired quadrature angles.

modulation of the amplitude *and* phase quadrature and can be described as the coherent addition of both:

$$\frac{1}{2}\hat{a}_{\text{sig}}\left[1 + \frac{m}{2}\left(e^{i\omega_k t} + e^{-i\omega_k t}\right)\right] + \frac{1}{2}\hat{a}_{\text{sig}}\left[1 + \frac{m}{2}\left(e^{i\omega_k t} - e^{-i\omega_k t}\right)\right] = \hat{a}_{\text{sig}}\left[1 + me^{i\omega_k t}\right],$$

where  $m$  denotes the modulation strength and  $\omega_k$  the modulation frequency. Since we are interested in stabilizing the relative phase  $\theta$  between local oscillator  $\hat{a}_{\text{LO}}$  and signal beam  $\hat{a}_{\text{sig}}$  we drop the quantum fluctuations and simply consider the classical amplitudes as

$$\begin{aligned}\hat{a}_{\text{sig}}(\omega_k) &\rightarrow \alpha_{\text{sig}} \cdot \left[1 + me^{i\omega_k t}\right], \\ \hat{a}_{\text{LO}}(\theta) &\rightarrow \alpha_{\text{LO}} \cdot e^{i\theta}.\end{aligned}$$

According to the input/output beam splitter relation (Equation (C.1)), the interference of these beams at a 50/50 beam splitter yields the output fields

$$\begin{aligned}\alpha_1 &= \frac{1}{\sqrt{2}}\left[\alpha_{\text{sig}}\left(1 + me^{i\omega_k t}\right) + \alpha_{\text{LO}}e^{i\theta}\right], \\ \alpha_2 &= \frac{1}{\sqrt{2}}\left[\alpha_{\text{sig}}\left(1 + me^{i\omega_k t}\right) - \alpha_{\text{LO}}e^{i\theta}\right].\end{aligned}$$

By detecting the photo-currents  $i_j \propto \alpha_j \alpha_j^*$ , taking their difference and considering the alternating current (AC) part, we obtain the expression

$$\Delta i_{\text{AC}} = 2\alpha_{\text{sig}}\alpha_{\text{LO}}m \cos(\omega_k t - \theta).$$

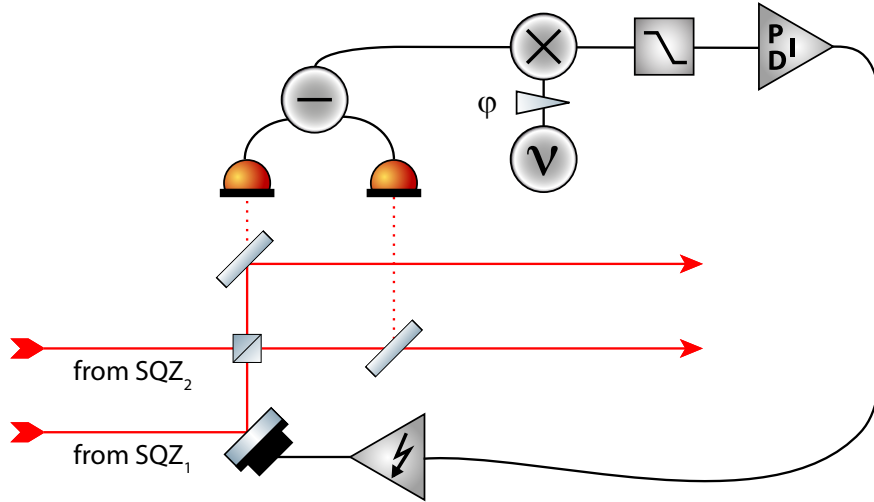


**Figure 4.3** – The phase stabilization at a phase gate works in the same manner as at a balanced homodyne detector, but only a small fraction of the beam splitter’s output ports is tapped off behind mirrors and is detected. Hence, the quantum states are barely attenuated.

Mixing this signal electronically with  $\sin(\omega_k t - \varphi)$  and low-pass filtering the output gives us the error signal

$$\Delta i_{AC,es} \propto \alpha_{sig} \alpha_{LO} m \sin(\theta - \varphi) ,$$

where  $\varphi$  denotes the phase of the electronic local oscillator (eLO). Setting  $\varphi$  to an arbitrary angle  $\theta$  gives a zero crossing in the error signal at that angle and allows stabilization of the homodyne detector to an arbitrary quadrature  $\hat{x}^\theta$ .

### Phase Gates

The stabilization of the phase between two signal fields can be treated in almost the same manner. The *phase gates*, as used in Chapter 5 to superimpose two quantum states under a specific angle, consist of a 50/50 beam splitter and a piezo actuated mirror (see Figure 4.3). In order not to attenuate the quantum states, only a small fraction of the output ports is tapped off at the mirrors and is detected. The photo-detectors’ signals yield the same error signal as for the balanced homodyne detector. Figure 4.2 shows the obtained error signal and an error signal produced with only one photo-detector. Although it is tempting to use only one photo-detector and hence introduce less optical loss, the latter is useless, since the error signal contains an offset term proportional to the sine of the electronic local oscillator phase  $\varphi$ :

$$i_{AC,es} \propto \alpha_{sig} \alpha_{LO} m \sin(\theta - \varphi) - |\alpha_{sig}|^2 m \sin(\varphi) .$$

### 4.3 Variable Attenuation for Specific Squeezing Settings

To prepare some quantum states, in particular bound entangled states, pairs of specific squeezing and anti-squeezing values are required. To set these parameters experimentally, a variable optical attenuator is introduced to the squeezed beam; it consists of a  $\lambda/2$ -wave plate and a polarizing beam splitter (PBS), compare with ⑦ in Figure 5.2 (a). Considering a squeezing cavity without losses, the variances of squeezing and anti-squeezing are related via  $V_S \cdot V_A = 1/16$ , as given by Equation (2.44). According to Equation (3.7), the attenuated variances, in the following denoted by a prime, are given by

$$V'_S = (1 - \tau) \cdot \frac{1}{16 \cdot V_A} + \frac{\tau}{4}, \quad (4.2)$$

$$V'_A = (1 - \tau) \cdot V_A + \frac{\tau}{4}, \quad (4.3)$$

where  $\tau$  denotes the optical loss ( $0 \leq \tau \leq 1$ ). Dividing Equation (4.3) by Equation (4.2) shows that the ratio of initially produced squeezing and anti-squeezing is equal to the ratio of the attenuated pair:

$$\frac{V'_A - \frac{1}{4}}{V'_S - \frac{1}{4}} = \frac{V_A - \frac{1}{4}}{\frac{1}{16 \cdot V_A} - \frac{1}{4}} \equiv \kappa.$$

Solving this equation for the variance of the anti-squeezing gives

$$V_A = \frac{1 - \kappa}{8} \stackrel{(+)}{=} \frac{1 + \kappa}{8} = -\frac{\kappa}{4}, \quad (4.4)$$

which is necessary to obtain the attenuated values. Subtracting Equation (4.2) from Equation (4.3) leads to the required attenuation to obtain the desired squeezing and anti-squeezing values

$$\tau = 1 - \frac{V'_A - V'_S}{V_A - \frac{1}{16 \cdot V_A}}. \quad (4.5)$$

In the case of a non-ideal squeezed light source we need to measure squeezing and anti-squeezing values and use Equation (4.4) to determine the initial squeezing value, i.e. before any cavity losses apply. Equation (4.5) gives the intrinsic loss  $\tau_i$  of the squeezing generation and detection, where  $V'$  now denotes the measured values. This loss enables us to determine how much anti-squeezing we need to produce by adjusting the optical pump field, see Equation (4.3). Since the optical efficiency is linear in  $\tau$  ( $\eta(\tau) = 1 - \tau$ ), we obtain the additionally required loss as

$$\tau_{\text{add}} = 1 - \frac{1 - \tau}{1 - \tau_i}. \quad (4.6)$$

**Example**

For the preparation of bound entanglement, one of the squeezers requires  $-2.7$  dB squeezing and  $+7.1$  dB anti-squeezing. Considering a lossless squeezing cavity, we need to start with  $+9.5$  dB anti-squeezing and introduce an attenuation of  $\tau = 47.8\%$ .

Figure 5.3 shows the measured squeezing and anti-squeezing values. Since the state is not pure, we find an intrinsic loss of  $19.5\%$  for the set of  $(-5.7$  dB,  $+9.5$  dB) at the measurement frequency  $6.4$  MHz; this corresponds to an initial squeezing value of  $-10.3$  dB. According to Equation (4.3) we need to reduce the optical pump power until we obtain  $+8.7$  dB anti-squeezing and introduce  $35.2\%$  additional loss to achieve the desired attenuation, see Equation (4.6). Alternatively, we can reduce the attenuation manually until we obtain the correct value.



## CHAPTER 5

---

### Bound Entanglement

---

The preparation of complex multimode entangled states of light is the basis of applications in quantum information processing and fundamental research in quantum physics. A prominent example of the latter is the preparation of *bound entanglement*.

Bound entanglement, which only exists in multimode quantum states, is of fundamental interest since it cannot be distilled, i.e. one is not able to extract fewer copies of more strongly entangled states by local operations and classical communication (LOCC) [58]. In contrast, “free” entanglement is distillable [24, 59, 60]. This irreversible character has triggered entire theoretical research programs [61], which try to link entanglement theory to a thermodynamical picture [28, 29]. Since bound entanglement is indistillable and seems to be unattractive for applications at first glance, it can – so far in theory – be activated and helps to improve the transmission of quantum information [30, 31]. In order to study such connections, new theoretical and experimental means of constructing multimode states must be investigated .

This chapter demonstrates the continuous unconditional preparation of one of the rarest types of multimode entanglement in the CV regime – a four-mode bipartite ( $2 \times 2$ ) bound entangled state.

### 5.1 Theoretical Description of Bound Entanglement

As stated above, bound entanglement represents entangled states which cannot be distilled. In order to identify them, we need to introduce criteria of entanglement and distillability in the CV regime.

### 5.1.1 Inseparability – An Entanglement Measure

A bipartite quantum state is said to be separable – not entangled – if we can describe the covariance matrix of the state as a direct sum of the state’s subsystems  $\gamma_A$  and  $\gamma_B$ . Their covariance matrices need to be physical according to Heisenberg’s Uncertainty Relation (Equation (3.4)) and have to obey the inequality [62]:

$$\begin{aligned} \gamma &\geq \gamma_A \oplus \gamma_B \\ &\geq \begin{pmatrix} \gamma_A & 0 \\ 0 & \gamma_B \end{pmatrix}. \end{aligned} \quad (5.1)$$

It is common to assume matrix ordering in such formulations: the matrix inequality  $A \geq B$  implies that  $A - B$  is a positive semidefinite matrix:  $\text{eig}(A - B) \geq 0$ .

If we cannot find any physical covariance matrix of the subsystems  $A$  and  $B$  with

$$\gamma_{A,B} \geq -\frac{i}{4}\Lambda \quad \Leftrightarrow \quad \text{eig}\left(\gamma_{A,B} + \frac{i}{4}\Lambda\right) \geq 0 \quad (5.2)$$

that fulfill Equation (5.1), the state is entangled; compare this with Equation (3.4). Its subsystems are therefore correlated more strongly than any classical state could be; as described by the direct sum of the covariance matrices.

This suggests a natural entanglement measure for Gaussian states by calculating “how far” the state is away from being separable [63]. By introducing a factor  $x \in \mathbb{R}^+$  in Equation (5.2)

$$\text{eig}\left(\gamma_{A,B} + \frac{ix}{4}\Lambda\right) \geq 0,$$

we can determine for which  $x$  Equation (5.1) is fulfilled. The largest possible  $x$  gives the margin “how far” the state is away from being separable. Separable states have  $x \geq 1$  and Heisenberg’s Uncertainty Relation is satisfied. For inseparable states Equation (5.1) cannot be fulfilled with physical states – Heisenberg’s Uncertainty Relation is violated and  $x$  is smaller than one. We thus introduce the entanglement measure [64]

$$E(\gamma) = 1 - \max_{\gamma_A, \gamma_B} x \quad (5.3)$$

with the constraints

$$\text{eig}\left(\gamma - (\gamma_A \oplus \gamma_B)\right) \geq 0, \quad \text{eig}\left(\gamma_{A,B} + \frac{ix}{4}\Lambda\right) \geq 0.$$

$E(\gamma) > 0$  implies that the state is entangled. The problem of solving these equations is known as a convex optimization problem that can be efficiently solved numerically; see Appendix A.



### 5.1.2 Partial Transposition – A Measure for Distillability

To obtain a measure for distillability, we consider a criterion that is commonly used as an entanglement measure for bipartite two-mode entangled states: the partial transposition of the state’s density matrix [65]. In the CV regime, the partial transposition corresponds to a mirror reflection or a “local time reversal” which only affects the  $p_B$  coordinate. The Wigner function transforms as

$$W(x_A, p_A, x_B, p_B) \rightarrow W(x_A, p_A, x_B, -p_B).$$

Expressed in covariances, the condition for separable states reads [54]

$$\text{eig}\left(\gamma^\Gamma + \frac{i}{4}\Lambda\right) \geq 0, \quad \gamma^\Gamma = M\gamma M, \quad M = \text{diag}(1, 1, 1, -1).$$

If the state remains physical under partial transposition, we obtain positive eigenvalues and the state is said to be PPT (positive partial transposition). The local subsystems can be modified individually – the state is separable. If we obtain at least one negative eigenvalue of the partial transposition (NPT) the subsystems cannot be modified locally without changing the whole state – the state is entangled.

However, this is only true for systems with  $1 \times N$  modes. For higher dimensional states, such as the bound entangled state with  $2 \times 2$  modes under discussion, the partial transposition provides only information about the state’s distillability. NPT entangled states can be distilled while PPT entangled states cannot [62]. For our bound entangled state we obtain the local time reversal by changing the sign of all momentum coordinates belonging to mode  $B$  and introduce  $M = \text{diag}(1, 1, 1, 1, 1, -1, 1, -1)$ . As a quantitative measure for the state’s distillability, we take the minimum eigenvalue of the partially transposed covariance matrix

$$P(\gamma) = \min \text{eig}\left(\gamma^\Gamma + \frac{i}{4}\Lambda\right). \quad (5.4)$$

A positive value of  $P(\gamma)$  attests that the state is not distillable.

In order to demonstrate that a state is bound entangled, we need to reconstruct the state’s covariance matrix and verify that it is entangled ( $E(\gamma) > 0$ ) and not distillable ( $P(\gamma) > 0$ ).

## 5.2 The Search for Bound Entangled States

The class of CV bipartite entangled states is in general NPT entangled and therefore distillable. Bound entangled states only exist in very small regions in phase space. In order to hit these tiny regions in phase space experimentally, we must find suitable states theoretically. This search was performed by colleagues in Potsdam and Mexico;

see the supplemental material of [66]. We will briefly sketch the techniques used to identify the regions of robust bound entanglement.

With the local unitary operations of squeezing and phase shifting (see Section 3.2) we are able to convert a covariance matrix to its bipartite normal form [67]. The advantage of rearranging the covariance matrix is a reduction from 36 to just 16 free parameters. The general bipartite normal form of the four-mode covariance matrix reads

$$\gamma = \begin{pmatrix} \lambda_1 & 0 & 0 & 0 & \lambda_5 & 0 & \lambda_9 & \lambda_{10} \\ 0 & \lambda_1 & 0 & 0 & 0 & \lambda_6 & \lambda_{11} & \lambda_{12} \\ 0 & 0 & \lambda_2 & 0 & \lambda_{13} & \lambda_{14} & \lambda_7 & 0 \\ 0 & 0 & 0 & \lambda_2 & \lambda_{15} & \lambda_{16} & 0 & \lambda_8 \\ \lambda_5 & 0 & \lambda_{13} & \lambda_{15} & \lambda_3 & 0 & 0 & 0 \\ 0 & \lambda_6 & \lambda_{14} & \lambda_{16} & 0 & \lambda_3 & 0 & 0 \\ \lambda_9 & \lambda_{11} & \lambda_7 & 0 & 0 & 0 & \lambda_4 & 0 \\ \lambda_{10} & \lambda_{12} & 0 & \lambda_8 & 0 & 0 & 0 & \lambda_4 \end{pmatrix}.$$

In order to obtain a bound entangled state, we vary the 16 parameters. We arbitrarily restrict them to the boundary of  $\pm 1/2$  and sample the hypercube  $[-1/2, 1/2]^{\times 16}$  uniformly. Once we find a covariance matrix describing a bound entangled state, determined by the inseparability and distillability criteria in Equations (5.3) and (5.4), respectively, we construct a random walk to improve the robustness. This is based on the  $16 \times 15/2$  two-dimensional planes, spanned by the  $\mathbb{R}^{16}$  parameter space. We either perform a rotation of an arbitrary plane – thus increasing one parameter and decreasing another by the same amount – or we perform a small displacement along a plane’s normal. After each step, we check whether the state is more bound entangled and repeat the procedure until no variation yields an improvement.

The theoretically most bound entangled state was found to be characterized by an inseparability value  $E(\gamma) = 0.054$  and a distillability value  $P(\gamma) = 0.132$ . In the experiment, however, it is too complex to engineer any arbitrary quantum state. Therefore the experimental layout and its restrictions were taken into account, as discussed in Section 5.3. We modeled the optical components directly and filtered the results allowing only covariance matrices corresponding to achievable experimental parameters.

### 5.3 Experimental Realization

In this section we discuss the experimental setup used to generate unconditional bound entangled states of light in the CV regime. Since bound entanglement only occurs in multimode quantum states, we constructed a four-mode bipartite state, i.e. two parties (Alice and Bob) possess two modes each.

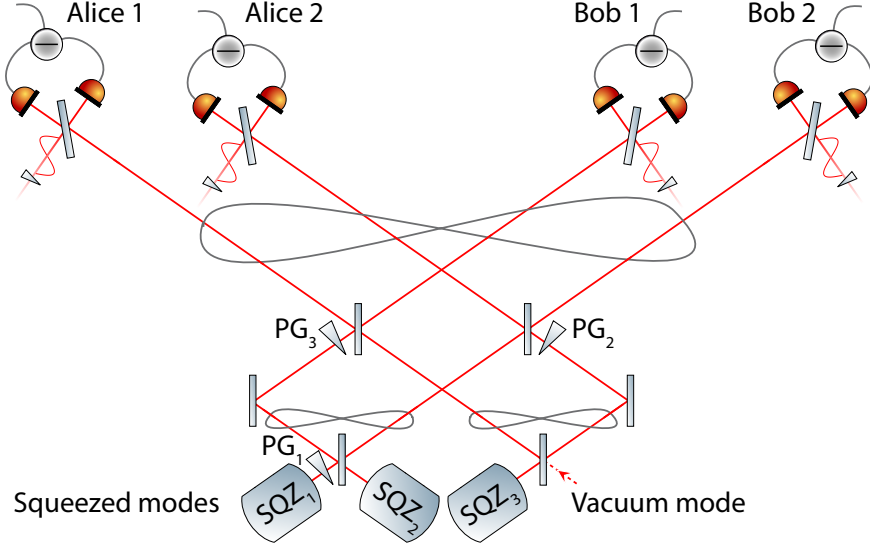


**Figure 5.1** – Overview of the experimental setup: Three squeezed-light sources ( $SQZ_{1-3}$ ) and three phase gates ( $PG_{1-3}$ ) are utilized to generate bound entanglement. Four homodyne detectors are needed to verify the state’s properties. We prepared a four-mode bipartite bound entangled state, i.e. two parties (Alice and Bob) possess two modes each.

For this purpose we used three squeezed-light fields and a vacuum mode as input states. They were superimposed on three phase gates, each of which consists of a beam splitter and a piezo mounted controllable mirror. Figure 5.1 shows a schematic overview. The four homodyne detectors are not needed for the state preparation but are necessary for its characterization.

Figure 5.2 shows the complete optical setup. In the following sections we discuss all components required to generate a bipartite bound entangled state.

### 5.3.1 Laser and Squeezer

The main laser source was a Neodymium-doped Yttrium Aluminum Garnet (Nd:YAG) solid state laser. The device used – model *Diabolo* by *Inno-Light* [68] – provided two single-mode output fields at 1064 nm and 532 nm with an optical power of 350 mW and 800 mW, respectively. They were used as control and pump fields for the squeezed light sources and served as a local oscillator for the homodyne detection.

The squeezing was generated by type I optical parametric down-conversion in a standing-wave cavity built around a nonlinear  $\chi^{(2)}$  medium. Appendix B provides a theoretical description. The  $\chi^{(2)}$  medium was a 7% Magnesium oxide doped Lithium Niobate ( $MgO:LiNbO_3$ ) crystal with a size of  $2.5 \times 5 \times 6.5 \text{ mm}^3$ . The crystal’s back ① is highly reflective ( $R > 99.96\%$ ) for 1064 nm and 532 nm light, whereas the flat front

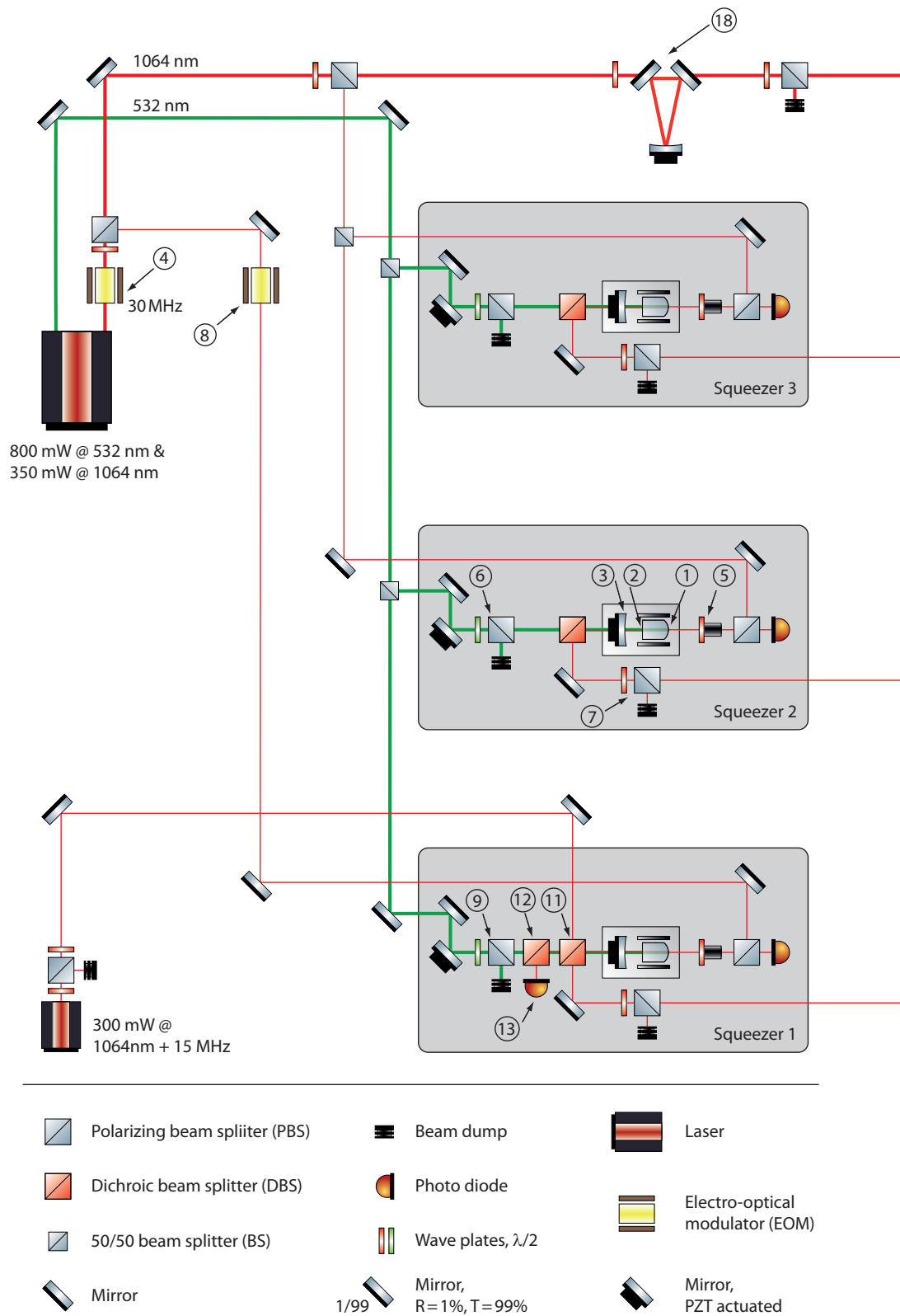


Figure 5.2 (a) – Experimental setup: Squeezing generation.

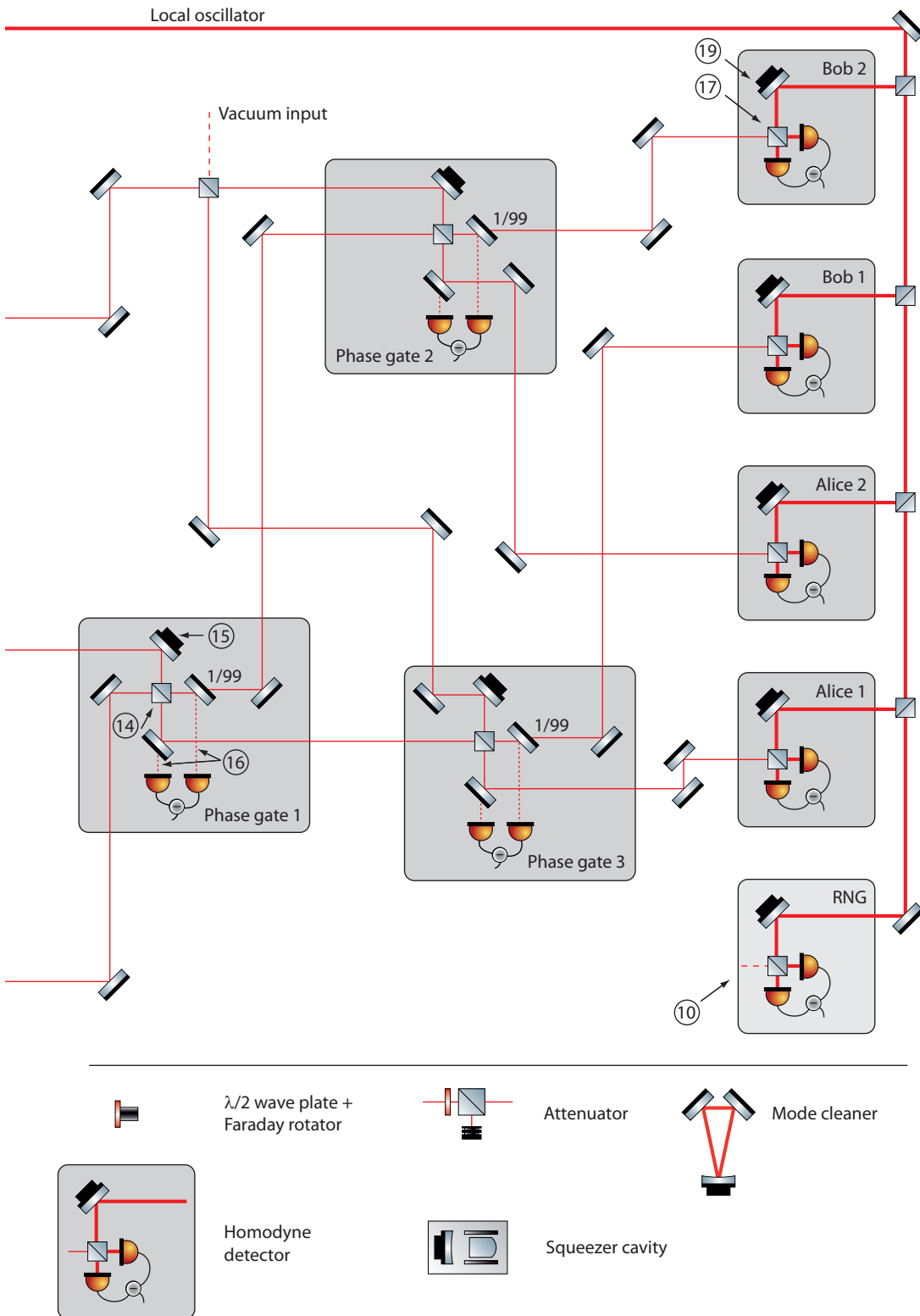
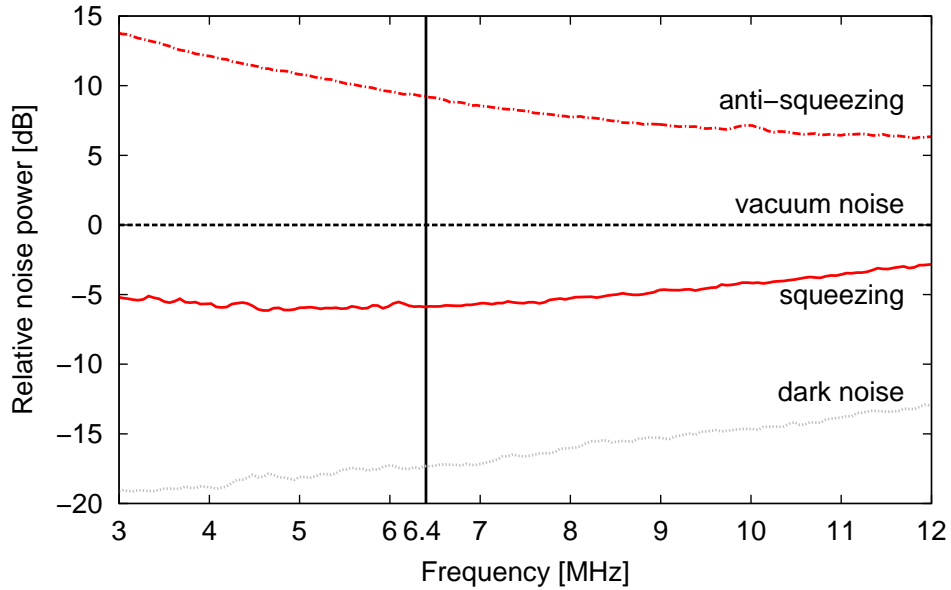


Figure 5.2 (b) – Experimental setup: Entanglement generation and detection.



**Figure 5.3** – Squeezing spectrum of Squeezer 3. The anti-squeezing and squeezing values of +9.5 dB and -5.7 dB at 6.4 MHz were obtained with 115 mW optical pump power. This is sufficient to generate the initial squeezing parameters, see Table 5.1 and Section 4.3.

② has an anti-reflective coating ( $R < 0.05\%$ ) for both wavelengths (for numbers see Figure 5.2). The front mirror ③ is mounted on a piezo-electric transducer (PZT) and has a reflectance of  $R_{1064} = 94\%$  and  $R_{532} = 25\%$ . This yielded a finesse of  $\mathcal{F}_{1064} = 100$  and  $\mathcal{F}_{532} = 4.3$ , respectively. The length of the cavity determined its free spectral range (FSR) to about 4 GHz. Phase matching of the fundamental and second harmonic field was achieved at a temperature of about  $60^\circ\text{C}$ , to which the crystal was actively stabilized. To control the length of the cavity, the control field was phase modulated at 30 MHz with an electro-optical modulator (EOM) ④ and coupled into the cavity from the back ①. The reflected field experienced a  $90^\circ$  polarization change at the  $\lambda/2$ -Faraday rotator combination ⑤ and passed the polarizing beam splitter (PBS). The photo-detector signal was demodulated at the modulation frequency to obtain a Pound-Drever-Hall (PDH) error signal [69] to control the cavity's length. More detailed descriptions of the squeezed-light sources can be found in [70, 71].

Figure 5.3 shows an example of the squeezing level produced by Squeezer 3 as a function of sideband frequency. The frequency used later on is highlighted. To generate a bound entangled state, specific pairs of squeezing and anti-squeezing values are required. Therefore, the anti-squeezing level is first set to the desired value by adjusting the pump power with a  $\lambda/2$ -PBS combination ⑥. Since squeezing is more degraded by optical loss than anti-squeezing (see Equation (3.7)) an additional variable attenuator

in the squeezing path ⑦ decreased the squeezing to the required value. The procedure to set the required values is described in Section 4.3.

To verify that the values are set correctly, they were checked at the homodyne detectors. Since further losses were introduced by several beam splitters, they were measured and included in the optical layout's model, see Section 3.2. The measured optical losses from the squeezers to the homodyne detectors read about 78%.

### 5.3.2 Generation of Hot Squeezing

Among conventional squeezing, the generation of bound entanglement requires *hot squeezing*. The term *hot squeezing* denotes the case when a state's quadrature noise distribution does not fall below the vacuum noise level for any quadrature. It corresponds to a classical (thermal) state with an unequal noise distribution.

There are several ways to generate a hot squeezed state. One approach is to superimpose two amplitude-squeezed modes with a relative phase of  $90^\circ$  and different anti-squeezing values on a 50/50 beam splitter. This corresponds to producing an entangled two-mode squeezed state, but in this case one mode is discarded. A more classical approach is to displace a coherent state by an amplitude and a phase modulation with a true random noise distribution of unequal strength at the desired frequency.

We chose a hybrid way to generate a hot squeezed state by applying a random phase modulation with a second EOM ⑧ to the control field of Squeezer 1. By locking the squeezer to the amplification mode we produce a phase squeezed state. The anti-squeezing gives the noise in the amplitude quadrature, which can be controlled by the optical pump power ⑨. The strength of the random phase modulation at the measurement frequency of 6.4 MHz sets the required phase noise. To obtain a random phase modulation, the EOM is driven with the amplified output of a homodyne detector that measures vacuum noise ⑩. Pseudo-random numbers are insufficient since they could introduce unintended correlations into the final state.

### 5.3.3 Locking Scheme

In order to lock the phase gates and homodyne detectors to specific angles and quadratures, a single sideband was introduced to the squeezed output beam of Squeezer 1. For this purpose we overlapped the output of a second laser with the transmitted control field of Squeezer 1 at a dichroic beam splitter (DBS) ⑪, which reflects at 1064 nm and transmits at 532 nm. Due to imperfect coatings, about 0.5% of the infrared fields was transmitted. This was sufficient to generate a beat-note between the transmitted control field and the reflected field of the second laser. We separated the beat note from the pump field with another DBS ⑫ and detected the beat with a photo-detector ⑬. This provided an error signal for the phase-lock loop (PLL) and we locked the two

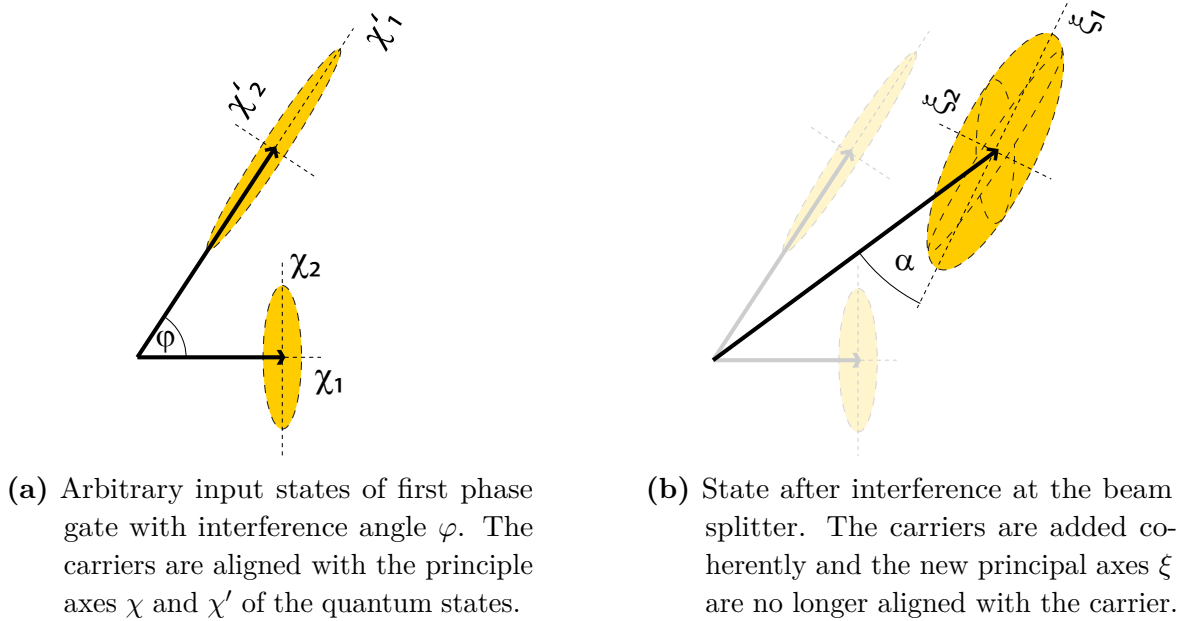


**Figure 5.4** – Interference at the phase gates. The angle  $\alpha$  between the carrier and the principal axis of the quantum noise depends on the phase difference  $\varphi$ , the coherent amplitudes and the squeezing / anti-squeezing values. Since only the carrier can be used to verify the angle between quantum noises, special care must be taken.

beams at an offset frequency of 15 MHz. A fraction of the additional laser beam was transmitted by the first DBS (11) and acted as a single sideband on the squeezed beam. Since the single sideband was present at every phase gate and homodyne detector, it was used to stabilize each device independently to an arbitrary angle by setting the electronic local oscillator (eLO) phase; see Section 4.2 for details.

### 5.3.4 Phase Gates

The phase gates (PG) were used to introduce a specific phase shift between the squeezed (PG<sub>1</sub>) and entangled fields (PG<sub>2&3</sub>). They consist of a 50/50 beam splitter (14), an actively controlled piezo mounted mirror (15), and a signal tap-off in each output port behind a highly-reflective (HR) mirror and a mirror with 1% reflectivity (16). The detected signals are subtracted and the obtained error signal provides a control signal that is fed back to the controllable mirror, see Section 4.2.

We are interested in a precisely set interference angle of the quantum noise distribution. Since the photo-detectors can only detect the classical carrier fields, we need to pay special attention here. Figure 5.4 depicts the problem. If we interfere two arbitrary



**Table 5.1** – Initial parameters of the experimentally realized bound entangled state.

(a) Squeezing variances			(b) Phase gate settings	
Squeezer	Squeezing	Anti-Squeezing	Phase gate	Angle
1	0.50 (+3.0 dB)	0.87 (+5.4 dB)	1	90°
2	0.16 (−2.0 dB)	0.64 (+4.0 dB)	2	41°
3	0.14 (−2.7 dB)	1.29 (+7.1 dB)	3	140°

squeezed states with a relative phase of  $\varphi$  at the first phase gate – e.g. an amplitude and a phase squeezed state as in Figure 5.4a – the carriers of the input fields are aligned with the principal axis  $\chi$  and  $\chi'$  of the quantum noise distribution. Depending on the interference angle  $\varphi$ , the carriers' coherent amplitudes and the squeezing / anti-squeezing strengths, the principal axes of the quantum noise distribution get rotated by the angle  $\alpha$  as shown in Figure 5.4b and are no longer aligned with the carrier. Proceeding with this state at the subsequent phase gates requires a precise knowledge of these parameters, since a small deviation can easily lead to a large error.

### 5.3.5 Measurement Process

To reconstruct the state's covariance matrix, we measured the noise of different quadratures of the four-mode state, as described in Section 3.3. Therefore, we used a balanced homodyne detector for each mode, see Section 4.1. They consist of a 50/50 beam splitter (BS) [\(17\)](#) where the signal field and a strong local oscillator (LO) are interfered. The spatial beam profile of the LO is cleaned with a three mirror ring cavity [\(18\)](#); its linewidth of 55 kHz ensured a vacuum noise limited field at the measurement frequency of 6.4 MHz. The phase between both beams is controlled with a piezo mounted mirror [\(19\)](#). With the single sideband modulation all homodyne detectors were stabilized independently; for details see Section 4.2. The detected signals were subtracted, electronically mixed with a 6.4 MHz electronic local oscillator (eLO) and low-pass filtered with a sixth order anti-alias filter with corner frequency of 400 kHz, see [\[71\]](#) for details. The measured homodyne data were sampled with an analog-to-digital converter (ADC). This was a 14 bit ADC *PCI-6133* from **National Instruments** with a sampling rate of 2.5 MS/s, and was controlled by a *Labview* script.

According to Section 3.3, we need to measure the noise of the amplitude, phase and 45° quadratures in order to reconstruct the covariance matrix. Since entanglement is invariant under local unitary transformations, we could choose any two arbitrary orthogonal quadratures as amplitude and phase quadratures. For experimental convenience, each mode's quadrature parallel to the carrier field was considered as the amplitude quadrature. The detectors' direct current (DC) outputs are used to identify

**Table 5.2** – Angle sign permutations of the phase gates. The angles of the phase gates need to be set to the same direction in order to preserve the entanglement properties.

Angle PG <sub>2</sub>	Angle PG <sub>3</sub>	$E(\gamma)$	$P(\gamma)$	Bound?
41°	140°	0.011	0.0097	✓
-41°	140°	0.184	-0.160	✗
-41°	-140°	0.011	0.0097	✓
41°	-140°	0.184	-0.160	✗

these angles. Another *Labview* script was used to save and recall the required eLO phases experimentally.

For each detector and quadrature measurement,  $4 \times 10^6$  data points were recorded to analyze the state.

### 5.3.6 Experimental Parameters

The theoretical search for bound entangled states in Section 5.2 produced a variety of possible parameters. To simplify the experimental complexity, we restricted the angle of the first phase gate to be 90°. Thus we could ensure that the principle axes of the quantum noise distribution are still aligned with the carrier fields at phase gates 2 and 3. Their angle settings were hence simplified drastically.

Table 5.1 shows the final set of the experimental parameters. The initial squeezing variances were verified at the homodyne detectors by modeling the setup’s losses, as described in Section 3.2. The first squeezer needs to produce a hot squeezed state. Without hot squeezing, no parameter set was found that produces a four-mode bipartite bound entangled state.

The phase gate angles were set using the homodyne detector’s DC voltages, which depend on the beam’s carrier fields. Special care needed to be taken, since 41° and -41° will not yield the same result but cannot be distinguished experimentally without reconstruction of the covariance matrix. Table 5.2 shows simulation results of sign permutations for the phase gates. As long as both phase gates are set in the same direction, the entanglement properties are preserved. Figures 5.5 and 5.6 show the full phase space of the state’s distillability and inseparability spanned by phase gates 2 and 3. Figures 5.7 and 5.8 illustrate the phase space of the product  $P(\gamma) \cdot E(\gamma)$ , which corresponds to a natural measure of bound entanglement. We set  $E(\gamma) < 0$  to zero to ensure that only areas of bound entanglement have a positive product. We see that the possible areas to obtain bound entanglement are rather rare and tiny.

Small variations of the parameters will result in completely different entanglement

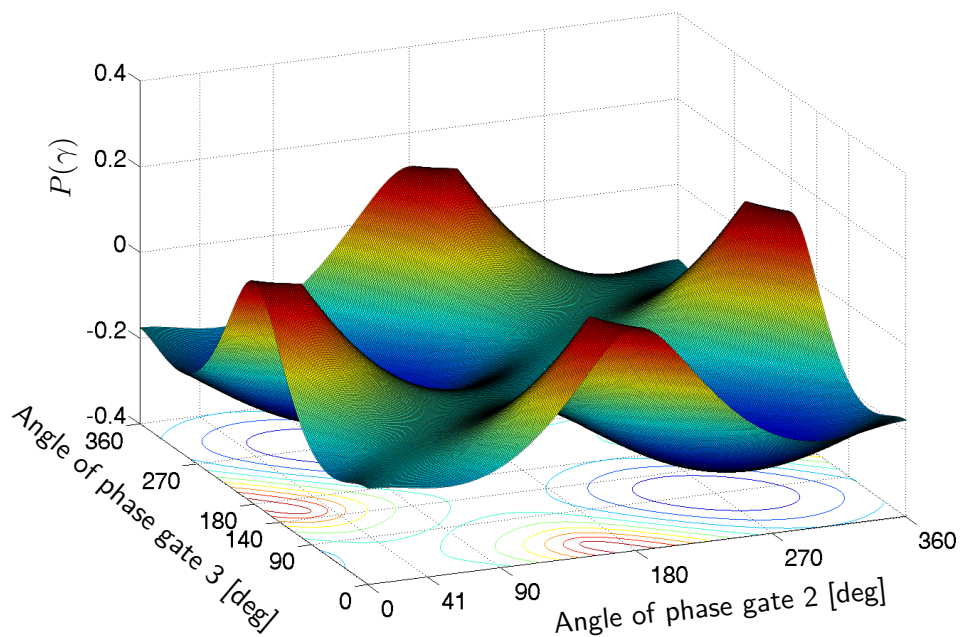


**Figure 5.5** – Phase space of distillability spanned by phase gates 2 and 3. The squeezing parameters are kept constant. The  $z$ -axis depicts the distillability  $P(\gamma)$ .

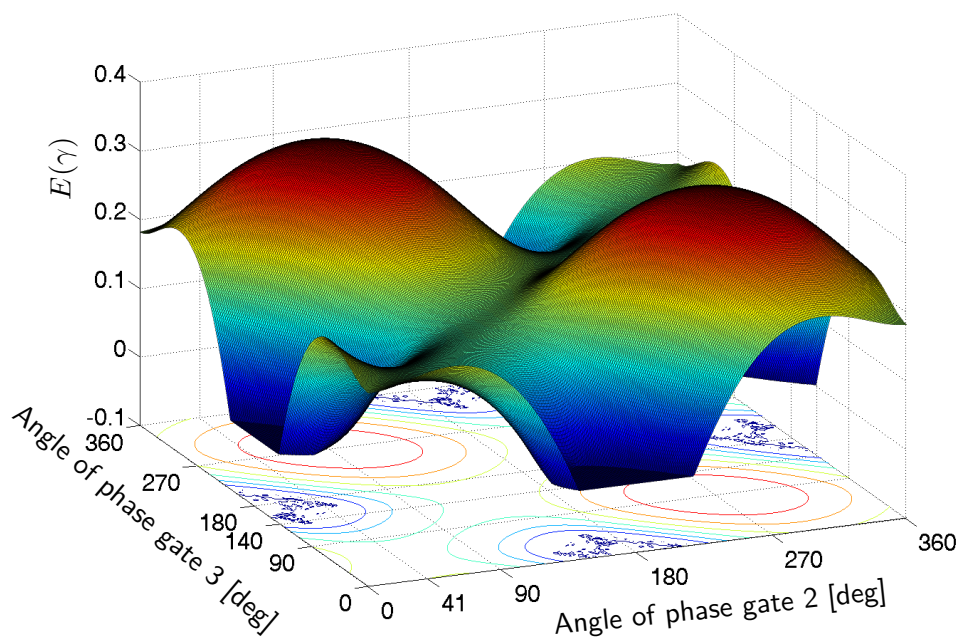


**Figure 5.6** – Phase space of inseparability spanned by phase gates 2 and 3. The squeezing parameters are kept constant. The  $z$ -axis depicts the inseparability  $E(\gamma)$ . Values for  $E(\gamma) < 0$  are set to zero.

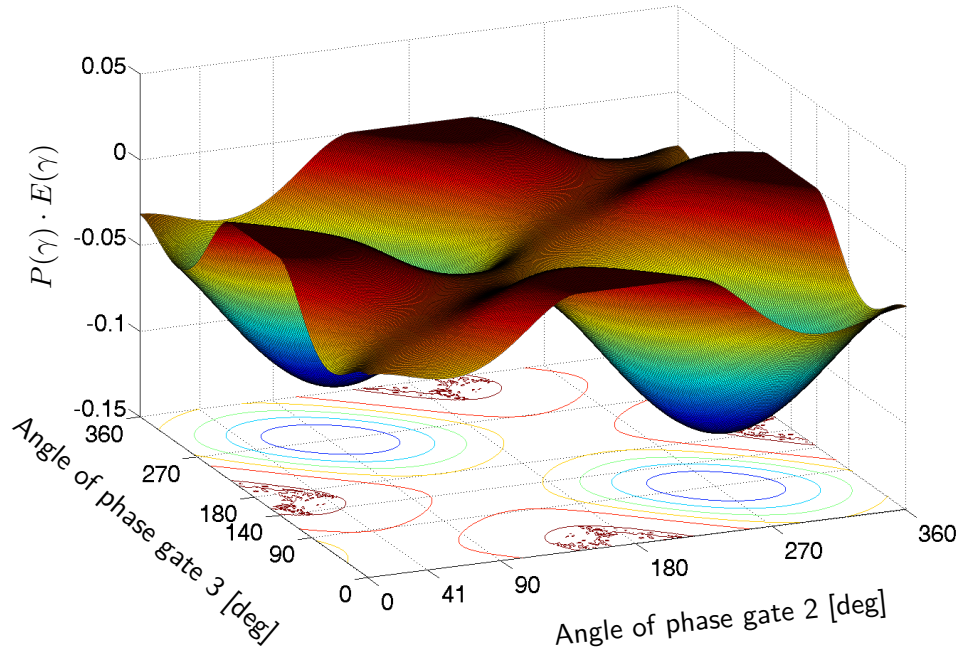


**Figure 5.7** – Phase space of bound entanglement spanned by phase gates 2 and 3, while the squeezing parameters are kept constant. The  $z$ -axis depicts the product of  $P(\gamma) \cdot E(\gamma)$ . Values for  $E(\gamma) < 0$  are set to zero to ensure that only bound entangled states have a positive product. At first, it appears that all values are smaller than zero and hence no bound entanglement occurs. Figure 5.8, however, shows only positive values and unveils tiny regions of bound entanglement.

properties. Figure 5.9 shows an example of varying one parameter, namely the phase of phase gate 3. Only in a small region (the white area) does bound entanglement occur and slight angle deviations immediately alter the separability and distillability. The properties of a generated bound entangled state can therefore not be predicted with a high accuracy. Further investigations to control and verify the initial squeezing values and phase gate settings are desirable. The results in Section 5.6 were obtained by carefully setting the initial parameters and then walking through phase space by slightly varying some parameters, reconstructing the covariance matrix and checking for bound entanglement.

## 5.4 Gaussianity of the Prepared States

The criteria for bound entanglement – distillability and inseparability – are strictly speaking valid only for Gaussian states. Although the physical mechanisms of the setup

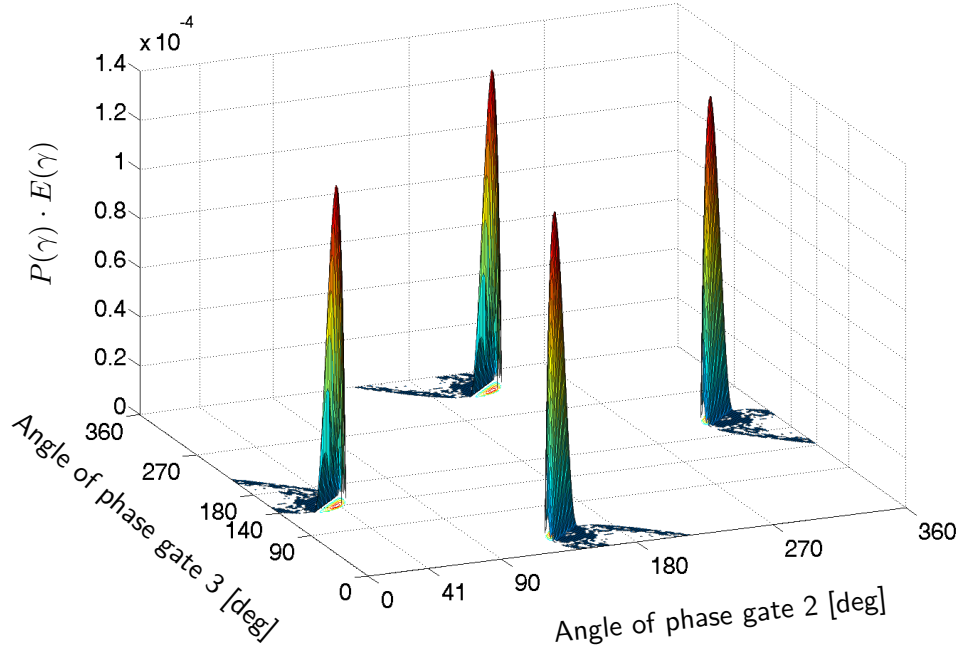


**Figure 5.8** – Zoom of Figure 5.7. Only positive values are plotted. We see that bound entanglement occurs only in a fraction of the entire phase space.

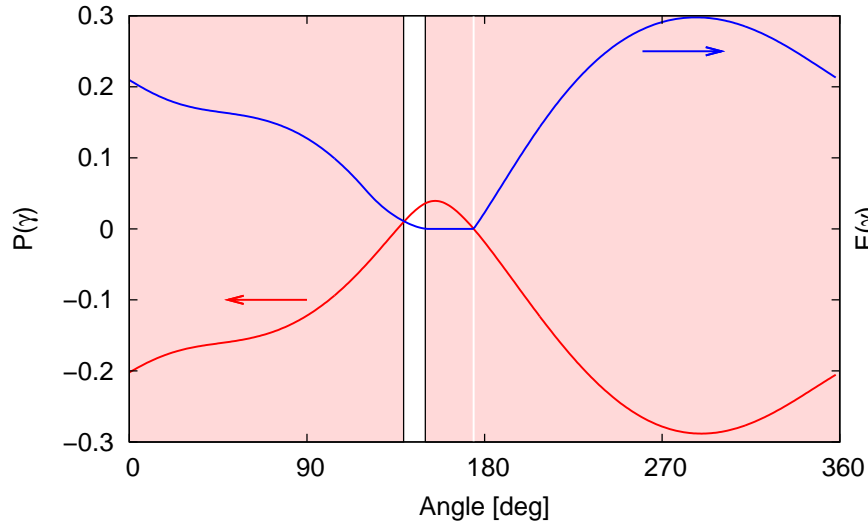


**Figure 5.9** – Occurrence of bound entanglement, depending on the angle of phase gate 3. For  $P(\gamma), E(\gamma) > 0$  (white area) bound entanglement occurs. The other parameters are kept constant as stated in Table 5.1. Additionally, at  $175^\circ$  we find a single point where bound entanglement could occur. However, this point is not experimentally accessible.

are solely Gaussian operations – vacuum squeezing, superposition on beam splitters, time-independent linear losses, phase shifts and balanced homodyne detection – phase noise could introduce a non-Gaussian statistic. To rule this out we need to verify the statistics of the prepared states. For this purpose, we take the raw data of the homodyne detectors and check their distribution for Gaussianity.

First, we analyze the raw data of a vacuum state, i.e. the signal field at the homodyne detector is blocked and hence replaced by a vacuum field. The cumulative distribution function (CDF) of the measured data looks Gaussian (Figure 5.10a). Looking at the difference between the measured and a theoretical Gaussian CDF small variations appear in the middle region, as shown by the red curve in Figure 5.10b. Since a vacuum state is per definition Gaussian, the deviation must result either from artifacts introduced by the data acquisition or from numerical errors. Since the measured quadratures of the signal fields exhibit the same behavior (the blue curve in Figure 5.10b shows, for example, the  $p$ -quadrature of Bob’s first detector) we can neglect this phenomenon.

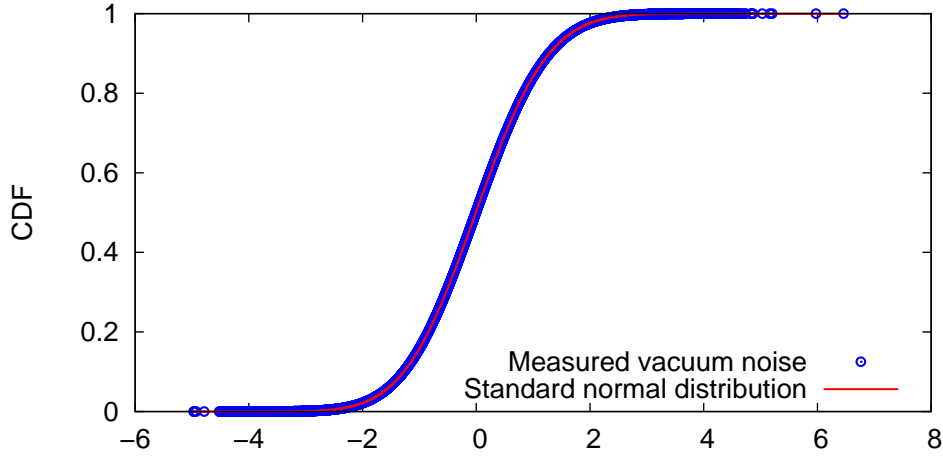
To ensure that the observed deviations from an ideal Gaussian CDF are negligible, we analyze the data with a QQ-plot. The QQ-plot of a perfect Gaussian distribution is a straight line, while random numbers drawn from a Gaussian statistic are distributed along that line (cf. Figure 3.5a). Figure 5.11 shows in red, as an example, the distribution of a  $p$ -measurement of Bob’s second homodyne detector. For comparison, quasi-random numbers with a perfect Gaussian distribution are shown in black. The dots are aligned along a straight line and strongly indicate a Gaussian distribution.

To analyze the data numerically, statistical hypothesis tests were used. A test with a strong significance is the Shapiro-Wilk-Test [72]. Since it can only handle 5000 samples, the total number of  $4 \times 10^6$  data points were randomly split into 800 blocks. Each block was confirmed by the test to follow a Gaussian distribution. The Kolmogorow-Smirnow (KS) Test [73], however, did not confirm Gaussianity for the total number of data points. Fortunately, this is obvious, because the test assumes a continuous distribution of the measured data. Since an analog-to-digital converter was used during data acquisition, the Gaussian distribution is quantized due to the resolution of the ADC. For a small sample size this does not matter but for a large sample size the test expects the values to lie closer together than experimentally possible.

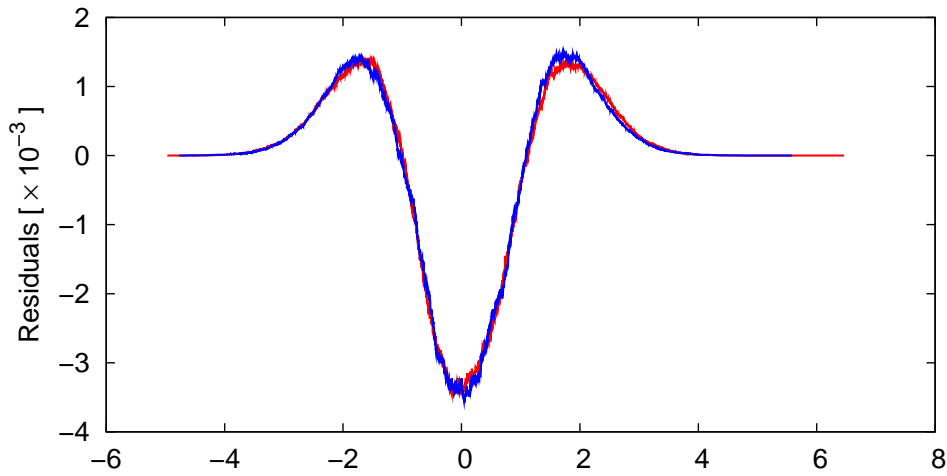
In summary, no significant contribution of phase noise could be found in the measured data and hence the prepared states are Gaussian.

## 5.5 Reconstructing the $8 \times 8$ Covariance Matrix

According to Section 3.3 we need the raw data of each homodyne detector to reconstruct the covariance matrix. In order to directly calculate the variances (\*), the covariances of the same quadrature of different modes (o) and the covariances of different



(a) Cumulative distribution function (CDF) of measured vacuum noise (blue) compared with a Gaussian curve (red). The curves seem to be identical.



(b) Difference of measured vacuum noise and Gaussian CDF (red). Small unexpected variations are observed. The blue curve shows the difference between a measured signal in the  $p$ -quadrature of Bob's first detector and a Gaussian CDF. Vacuum noise and signal show the same structure.

**Figure 5.10** – Comparison of the measured cumulative distribution functions (CDF) and the differences between theoretical and measured curves. Variations in the signal distribution show the same behavior as vacuum noise.

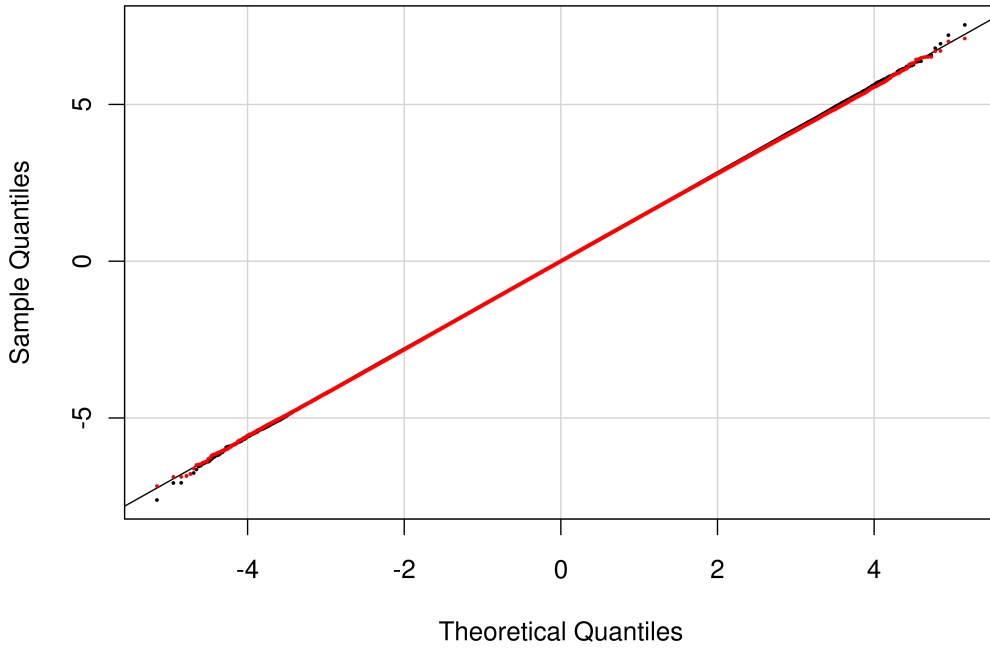


**Figure 5.11** – QQ-plot of the raw data of a typical measurement with  $4 \times 10^6$  data points (red dots). The measurement data follows a Gaussian statistic, since the points are aligned along the straight line. For comparison quasi-random numbers from a perfect Gaussian distribution are shown (black dots).

quadratures of different modes ( $\bullet$ ), we need to measure a set of different quadrature settings. Table 5.3 summarizes the eight different homodyne detector settings needed. Equation (5.5) shows the entries of the  $8 \times 8$  covariance matrix. The numbers indicate which measurement, according to Table 5.3, is needed for the given entry. More than one number indicates that the value can be calculated via multiple measurements and hence averaged:

$$\gamma^{(4)} = \begin{pmatrix} *2, 6, 7, 8 & \times & \circ 2, 7, 8 & \bullet 6 & \circ 2, 6, 8 & \bullet 7 & \circ 2, 6, 7 & \bullet 8 \\ & *4, 5 & \bullet 5 & \circ 4 & \bullet 5 & \circ 4 & \bullet 5 & \circ 4 \\ & & *2, 5, 7, 8 & \times & \circ 2, 5, 8 & \bullet 7 & \circ 2, 6, 7 & \bullet 8 \\ & & & *4, 6 & \bullet 6 & \circ 4 & \bullet 6 & \circ 4 \\ & & & & *2, 5, 6, 8 & \times & \circ 2, 5, 6 & \bullet 8 \\ & & & & & *4, 7 & \bullet 7 & \circ 4 \\ & & & & & & *2, 5, 6, 7 & \times \\ & & & & & & & *4, 8 \end{pmatrix}. \quad (5.5)$$

We express the covariances of different quadratures of the same mode ( $\times$ ) by the Weyl correspondence from Equation (3.13). The linear combination of the  $x$ ,  $p$



**Table 5.3** – Required quadrature measurements to reconstruct the  $8 \times 8$  covariance matrix.

#	Alice 1	Alice 2	Bob 1	Bob 2
1		vacuum noise		
2		$x$		
3		$45^\circ$		
4		$p$		
5	$p$	$x$	$x$	$x$
6	$x$	$p$	$x$	$x$
7	$x$	$x$	$p$	$x$
8	$x$	$x$	$x$	$p$

and  $45^\circ$  quadrature variances of the considered mode yield the desired entry; from Equation (3.12) we have

$$\gamma_{i,i+1}^{(4)} = \langle (\Delta \hat{x}^{45^\circ})^2 \rangle - \frac{\langle (\Delta \hat{x})^2 \rangle + \langle (\Delta \hat{p})^2 \rangle}{2}, \quad i \in \{1, 3, 5, 7\}.$$

Since the covariance matrix is symmetric we are able to reconstruct it by eight measurements, including one vacuum noise reference for normalization.

## 5.6 Experimental Results

To obtain the experimental results, we set the initial squeezing, anti-squeezing and phase gate settings from Table 5.1 as accurately as possible. Then, we recorded the raw data of the eight different balanced homodyne detector settings and reconstructed the covariance matrix with a *Matlab* script, as described in Section 5.5. Finally, we applied the criteria of Section 5.1 to the covariance matrix. Since we did not hit the region of bound entanglement immediately, we walked through phase space by slightly varying some parameters and repeating the procedure. The best obtained covariance matrix  $\gamma_*$  is shown in Table 5.4. Its entanglement properties are  $P(\gamma_*) = 0.0235$  and  $E(\gamma_*) = 0.0072$ . The state is strongly bound entangled:  $P(\gamma_*) \cdot E(\gamma_*) = 1.69 \times 10^{-4}$ .

In order to obtain information about the statistical error, we used the *bootstrapping* method: we randomly selected 20,000 different samples from the initial  $4 \times 10^6$  data points, reconstructed the covariance matrix, calculated distillability and inseparability and repeated this procedure 10,000 times. These results are plotted in Figure 5.12. The histograms of distillability and inseparability are depicted in Figure 5.12a while the individual bootstrapping results are represented by the black points in Figure 5.12b. The red cross shows the average calculated from the total data set. Figure 5.12a

**Table 5.4** – Covariance matrix of the best obtained bound entangled state. Its entanglement properties are  $P(\gamma_*) = 0.0235$  and  $E(\gamma_*) = 0.0072$ .

$$\gamma_* = \begin{pmatrix} 0.4827 & -0.0400 & 0.1445 & -0.1799 & -0.0207 & -0.0700 & -0.0006 & -0.1203 \\ -0.0400 & 0.3202 & -0.1706 & 0.0338 & -0.0841 & 0.0306 & 0.0636 & 0.0511 \\ 0.1445 & -0.1706 & 0.4220 & -0.0628 & 0.0436 & -0.0430 & -0.0427 & -0.1790 \\ -0.1799 & 0.0338 & -0.0628 & 0.6216 & -0.0276 & 0.2237 & -0.1419 & -0.0027 \\ -0.0207 & -0.0841 & 0.0436 & -0.0276 & 0.2510 & -0.0078 & -0.0735 & -0.0872 \\ -0.0700 & 0.0306 & -0.0430 & 0.2237 & -0.0078 & 0.6633 & -0.2895 & 0.1707 \\ -0.0006 & 0.0636 & -0.0427 & -0.1419 & -0.0735 & -0.2895 & 0.4470 & -0.1021 \\ -0.1203 & 0.0511 & -0.1790 & -0.0027 & -0.0872 & 0.1707 & -0.1021 & 0.4925 \end{pmatrix}$$

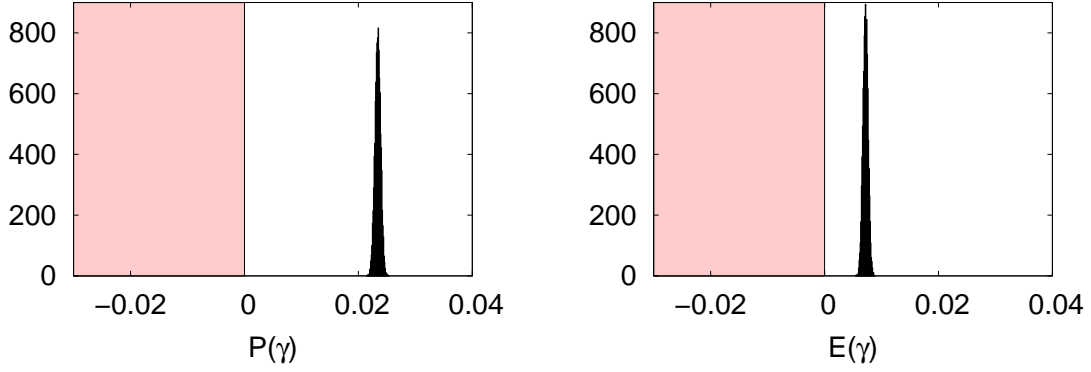
illustrates the significance of the measurement: the state is  $46\sigma$  away from being distillable ( $P(\gamma) \leq 0$ ) and  $16\sigma$  away from being separable ( $E(\gamma) \leq 0$ ). Checking Heisenberg’s Uncertainty Relation (Equation (3.4)) also confirms the physicality of the measured state:  $B(\gamma) = 0.0303 \pm 0.00057$ . It is  $53\sigma$  away from being unphysical, i.e. the setup was stable over the entire measurement time and constantly produced the same quantum state with little statistical uncertainty.

Based on this result, we optimized the parameters and found a region where we could set all three possible entanglement types by tuning phase gate 3, see Figure 5.13. At the angle setting of  $205^\circ$  the state was NPT entangled, i.e. the state was distillable (Figure 5.13a). By adding  $5^\circ$  we entered the bound entangled region (Figure 5.13b). With  $P(\gamma) = 0.0233 \pm 0.00066$  and  $E(\gamma) = 0.00168 \pm 0.00048$ , we were  $35\sigma$  and  $3.5\sigma$  away from distillability and inseparability, respectively.  $B(\gamma) = 0.0215 \pm 0.00056$  also confirms Heisenberg’s Uncertainty Relation: the state is  $38\sigma$  away from being unphysical. Adding another  $5^\circ$  the state became separable and hence indistillable (Figure 5.13c). Table 5.5 summarizes the obtained results.

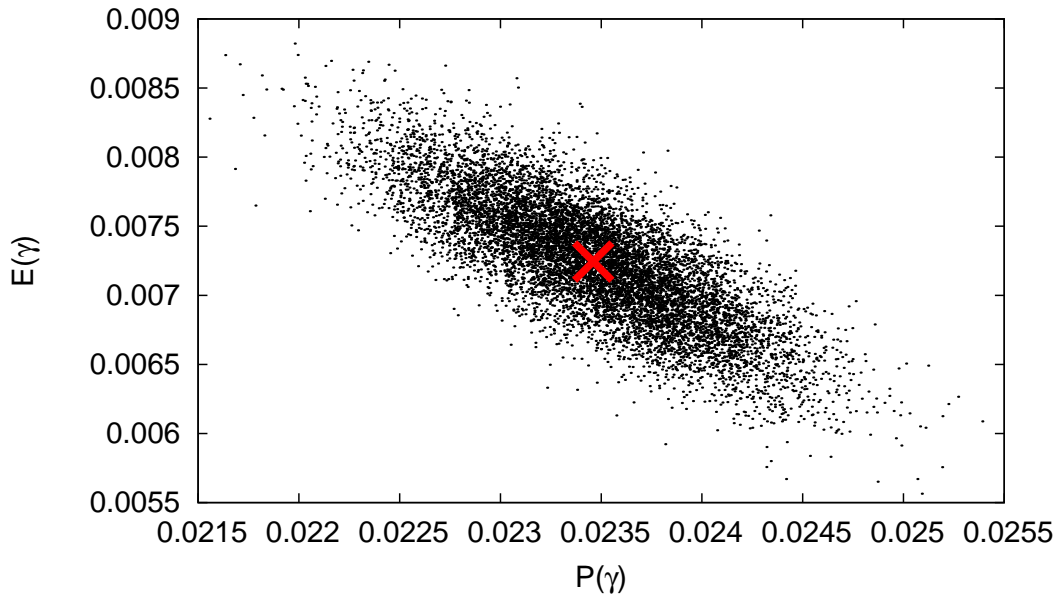
## 5.7 Discussion

The results presented in this chapter demonstrated for the first time the unconditional preparation of bound entangled states of light with high significance. The preparation of the four-mode bipartite state is independent of any postselection and can hence easily be distributed. Downstream applications could utilize the states and perform tests on their decoherence and (in-)distillability. The connection between thermodynamics and entanglement can now be studied experimentally.

The experiments presented here improved upon preparatory work conducted in cooperation with James DiGuglielmo, which unfortunately suffered from some critical issues and hence could not reconstruct a bona fide bound entangled state [74]. Not



- (a) Histograms of the measurement. The state is clearly bound entangled. The values of distillability and inseparability are  $P(\gamma_*) = 0.0235 \pm 0.0005$  and  $E(\gamma_*) = 0.0072 \pm 0.00046$ , respectively. The state is  $46\sigma$  away from being distillable and  $16\sigma$  away from being separable ( $P(\gamma), E(\gamma) \leq 0$ , red area).



- (b) 2D illustration of the measurement. The  $10^4$  black points represent the individual bootstrapping results. The red cross depicts the average value, calculated from the total data set.

**Figure 5.12** – Measurement results of the best bound entangled state obtained.

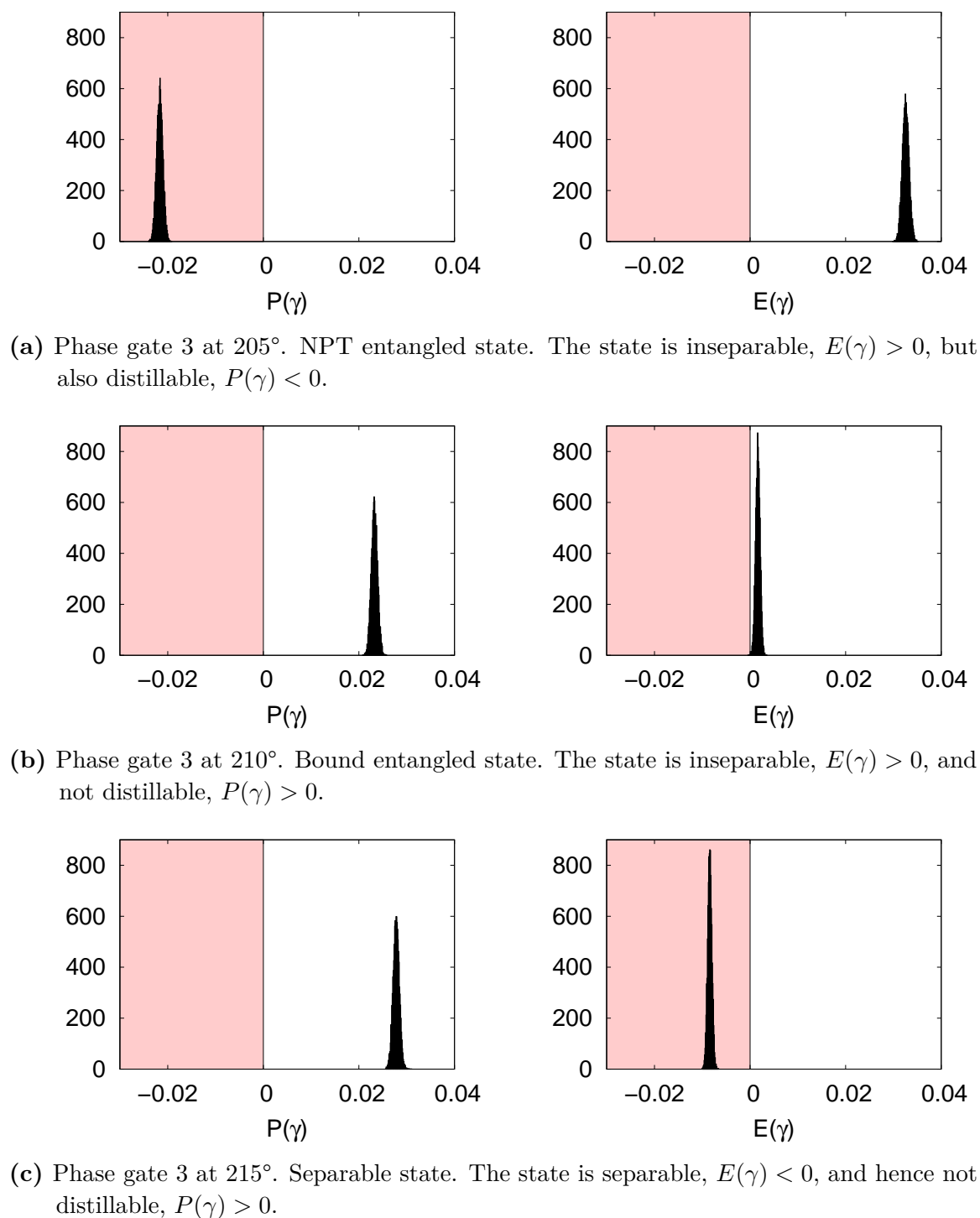


**Figure 5.13** – Mapping the phase space of phase gate 3. By tuning the angle of phase gate 3 we can tune the entanglement properties of the state.

**Table 5.5** – Experimental results. All three entanglement properties can be obtained by tuning the angle of phase gate 3.

Angle	Type	$P(\gamma)$	$E(\gamma)$	$B(\gamma)$
205°	NPT	$-0.0216 \pm 0.00067$	$0.0326 \pm 0.00071$	$0.0236 \pm 0.00059$
210°	BE	$0.0233 \pm 0.00066$	$0.00168 \pm 0.00048$	$0.0215 \pm 0.00056$
215°	Sep	$0.0279 \pm 0.00066$	$-0.00838 \pm 0.00046$	$0.0277 \pm 0.00054$

only were we able to correct these issues, but we also achieved a high degree of experimental control in multimode quantum state preparation. Hence, it is shown that the unconditional continuous variable regime is appropriate for fundamental research in quantum information science.



---

### Twin Beams – Entanglement between 810 nm and 1550 nm

---

Entangled states of light are the fundamental resource of many quantum communication and information protocols [75]. To use these protocols between remote parties, the entangled states are usually distributed by existing telecommunications fiber networks operated at a wavelength of 1550 nm. Even though standard telecommunications fibers have reached very low attenuation values [33], quantum repeaters are necessary to bridge distances of several hundred kilometers. Alkaline atoms having transition lines at wavelengths around 810 nm may be used to establish quantum memories [36, 37] that are an essential requirement in quantum repeaters. To connect these two wavelengths, entangled twin beams between 810 nm and 1550 nm could be used to transfer the quantum states from one wavelength to the other via entanglement swapping.

In this chapter we discuss the operation of a non-degenerate optical parametric oscillator above threshold and demonstrate the generation of bright bipartite entanglement between its twin beams at the wavelengths of 810 nm and 1550 nm.

#### **6.1 Theory of Optical Parametric Oscillation above Threshold**

In order to describe the effects of an optical parametric oscillator above threshold, we consider the process of difference-frequency generation. This process leads to an amplification of the signal input field and generates an idler field due to conservation of energy (Section 2.1.3). Hence, it is also known as optical parametric amplification.

With the coupled wave equations (2.24) and (2.25) we obtain, analogously to Section 2.1.3, the evolution of the field amplitude for the difference-frequency generation

(see [47] for details):

$$E_1(z) = \left[ E_1(0) \left( \cosh(gz) - \frac{i\Delta k}{2g} \sinh(gz) \right) + \frac{\kappa_1}{g} E_2^*(0) \sinh(gz) \right] e^{i\Delta k z/2},$$

$$E_2(z) = \left[ E_2(0) \left( \cosh(gz) - \frac{i\Delta k}{2g} \sinh(gz) \right) + \frac{\kappa_2}{g} E_1^*(0) \sinh(gz) \right] e^{i\Delta k z/2}.$$

The wave vector mismatch is given by  $\Delta k = k_3 - k_1 - k_2$  and we have used the quantities

$$g = \sqrt{\kappa_1 \kappa_2^* - (\Delta k/2)^2} \quad \text{and} \quad \kappa_i = \frac{2i\omega_i^2 d_{\text{eff}} E_3}{k_i c^2}.$$

If the nonlinear medium is placed inside a cavity, which provides suitable optical feedback, the gain of this amplification can lead to an oscillatory behavior: an optical parametric oscillation (OPO). The threshold condition for such an OPO can be obtained from the constraint that signal and idler fields must replicate themselves after each cavity round trip. For intensity reflectivities  $R_1$  and  $R_2$  of signal and idler field, respectively, and perfect wave vector matching,  $\Delta k = 0$ , we obtain

$$E_1(0) \stackrel{!}{=} \left[ E_1(0) \cosh(gL) + \frac{\kappa_1}{g} E_2^*(0) \sinh(gL) \right] (1 - l_1),$$

$$E_2^*(0) \stackrel{!}{=} \left[ E_2^*(0) \cosh(gL) + \frac{\kappa_2^*}{g} E_1(0) \sinh(gL) \right] (1 - l_2),$$
(6.1)

where  $l_i = 1 - R_i e^{-\beta_i L}$  is the amplitude loss per round trip and  $\beta_i$  the crystal's intensity absorption coefficient at frequency  $\omega_i$ . Since both equations must be satisfied we find

$$\cosh(gL) = 1 + \frac{l_1 l_2}{2 - l_1 - l_2}.$$

For high reflectivities and low absorption, i.e.  $l_i \ll 1$ , we obtain the approximation

$$g^2 L^2 = l_1 l_2.$$

Taking a non-perfect wave vector matching into account,  $\Delta k \neq 0$ , we replace  $g^2$  by  $g^2 \text{sinc}(\Delta k L/2)$  [47]. Knowing all these parameters, we can calculate the threshold pump power

$$P_{\text{thr}} = \frac{\pi w_0^2}{2} \cdot \frac{c \epsilon_0 n}{2} |E_3|^2,$$

where the cavity's waist  $w_0$  determines the intensity of the light field.

Figure 6.1 shows the Airy functions of a doubly resonant cavity for two twin beams at 810 nm (yellow) and 1550 nm (red) and the gain profile of the wave vector matching (black, dashed). A simultaneous resonance of both fields is only given at specific



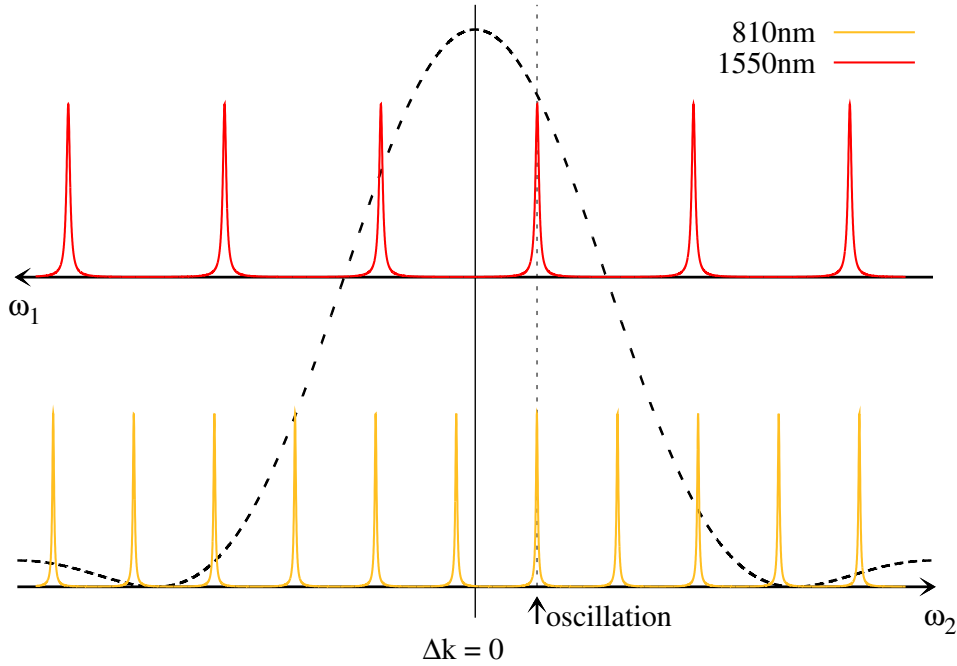


**Figure 6.1** – The cavity’s amplitude transmittances at 810 nm (yellow) and 1550 nm (red) and the wave vector matching profile (black, dashed). The axes of the frequencies  $\omega_1$  and  $\omega_2$  increase in opposite directions. Thus, the sum of all frequencies lying upon each other is constant and given by the pump field  $\omega_3 = \omega_1 + \omega_2$  due to conservation of energy. An oscillation can only occur if both wavelengths are on resonance and lie within the amplification region of proper wave vector matching.

frequencies. Only one simultaneous resonance occurs inside the gain profile due to the non-integer frequency spacing of the fields. The frequencies  $\omega_1$  and  $\omega_2$  increase in opposite directions, since the sum of two frequencies lying upon each other is given by the pump field  $\omega_3 = \omega_1 + \omega_2$ . An optical parametric oscillation can only occur if both wavelengths are on resonance and within the amplification region of proper wave vector matching. Figure 6.2 shows the product of both Airy functions and the gain profile. The better the overlap between all three factors, the higher the probability that the OPO will oscillate at that specific frequency. To tune the resonance condition experimentally, we controlled the cavity’s length. The experimental setup is discussed in Section 6.3.3. Figure 6.3 visualizes the occurrence of mode hops and cluster jumps of a doubly resonant OPO [76].

As stated in Equations (6.1), the OPO needs an initial signal field (seed) to start the oscillation. If no external field is present, spontaneous fluorescence is sufficient to provide this trigger. A fraction of about  $10^{-9}$  of the pump photons spontaneously

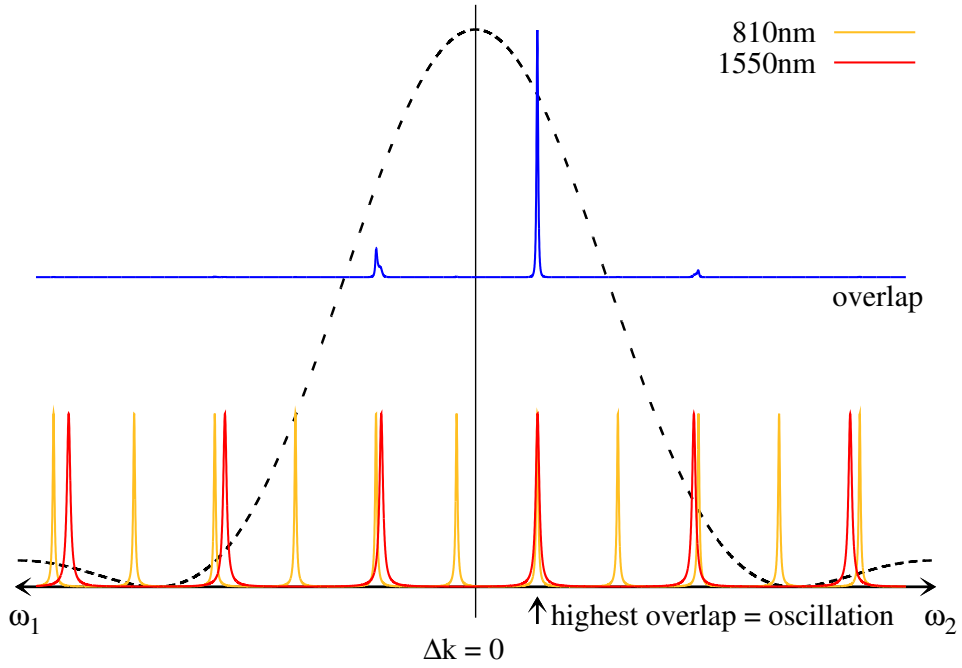


**Figure 6.2** – Product (blue) of the cavity’s amplitude transmittances (yellow and red) and amplification profile (black, dashed). The blue curve shows the frequencies at which the OPO will most likely oscillate.

decay and create pairs of signal and idler photons [77]. Some of these photons are emitted into the cavity mode and can serve as the required seed.

## 6.2 Quantum Correlations between the Twin Beams

The quantum correlations produced by an OPO can be understood intuitively: the nonlinear crystal emits pairs of photons, according to the interaction Hamiltonian

$$\hat{H}_{\text{int}} = i\hbar d_{\text{eff}} \left( \hat{a}_3^\dagger \hat{a}_1 \hat{a}_2 - \hat{a}_3 \hat{a}_1^\dagger \hat{a}_2^\dagger \right).$$

Each time a pump photon  $\omega_3$  is annihilated two twin photons are created which have the same photon statistics; hence, there is no noise in the intensity difference. The energy conservation  $\omega_1 + \omega_2 = \omega_3$  (depicted in Figure 6.4a), leads to an anti-correlation in the frequency (phase): if the frequency of one twin fluctuates, the frequency of the other must fluctuate in the opposite direction. The cavity around the nonlinear crystal introduces decoherence between the twin beams. The number of photons in the output beams is expected to be nearly equal only when they are counted during a long time compared to the cavity storage time, i.e. the quantum noise reduction only occurs within the cavity bandwidth.

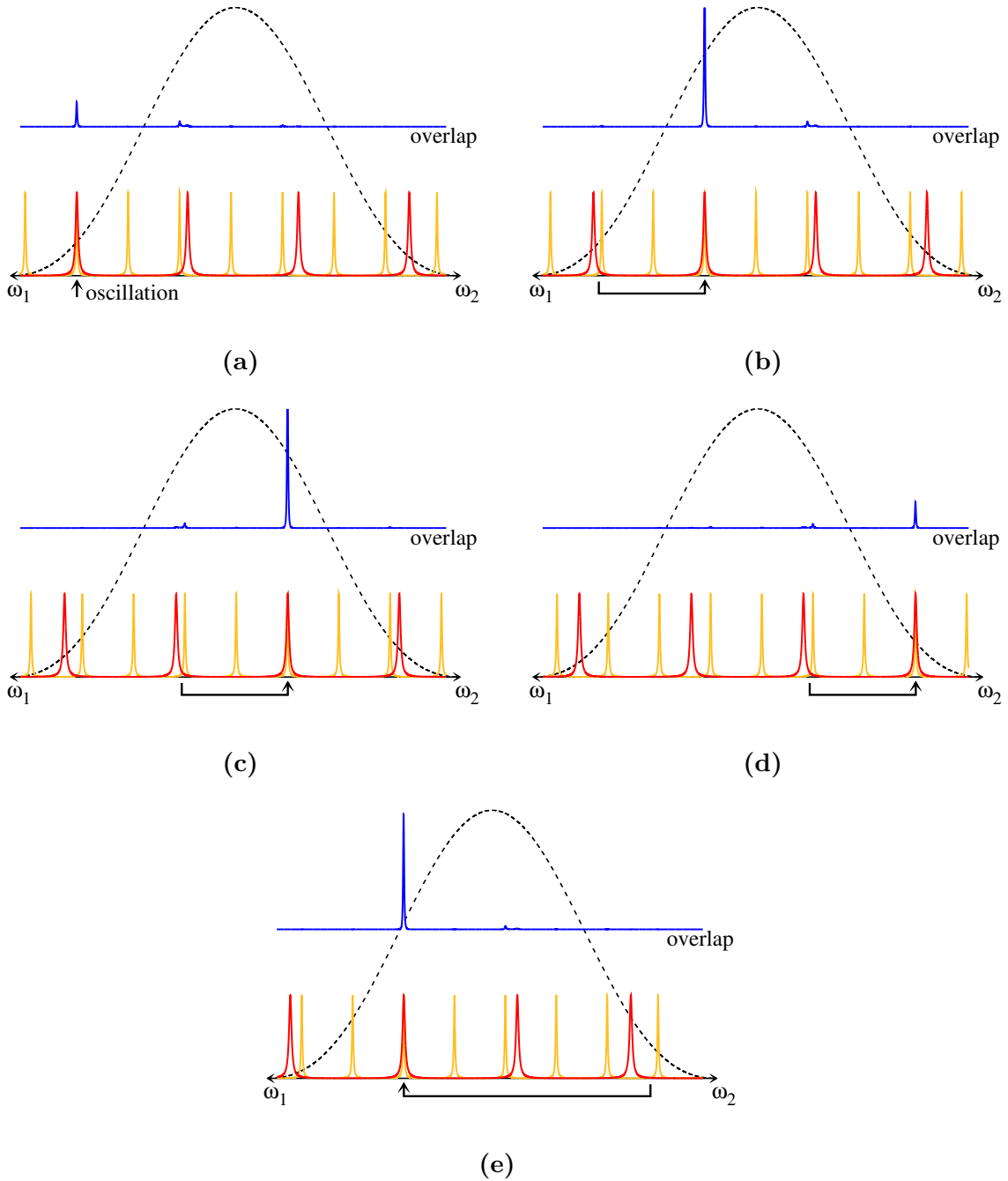


**Figure 6.3** – Visualization of mode hops and cluster jumps. At the initial resonance condition, the OPO oscillates at high  $\omega_1$  (red) and low  $\omega_2$  (yellow) frequencies (a). Altering the resonance condition, e.g. by tuning the cavity's length, lets adjacent longitudinal cavity modes become resonant simultaneously: a mode hop occurs. The oscillation frequency  $\omega_1$  decreases and  $\omega_2$  increases, (b)  $\rightarrow$  (d). Further tuning (e) leads to a cluster jump. Two distant longitudinal cavity modes become resonant simultaneously and the oscillation frequencies jump back.

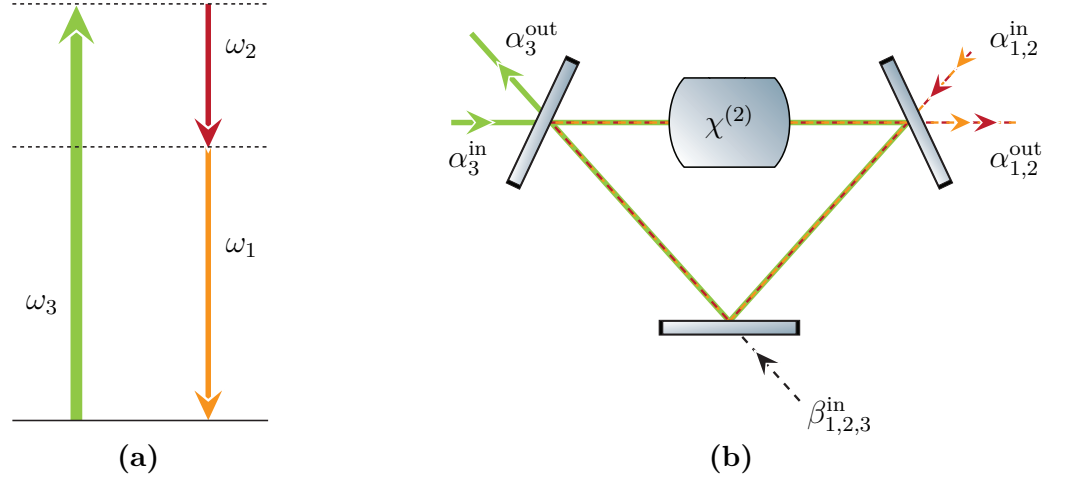


**Figure 6.4** – Energy level diagram of difference-frequency generation (a) and an optical parametric oscillator cavity with the fields involved (b).  $\alpha_{0,1,2}^{\text{in/out}}$  are the incoming / outgoing pump and signal fields.  $\beta_i$  are the incoupling vacuum fields, associated with the internal losses of each mode. The pump photons at  $\omega_3$  are down-converted in a  $\chi^{(2)}$  medium and amplify a potential input field at  $\omega_2$ . An idler field at  $\omega_1$  is created, due to conservation of energy.

The quantum correlations of an OPO have been calculated in a fully quantum mechanical treatment [78]. Nevertheless, a semi-classical treatment yields the same results [79, 80], which we will sketch here. We start with the equations of motion of a cavity (see Appendix B for a derivation):

$$\begin{aligned}\tau\delta\dot{\alpha}_1 + (\gamma_1 + \mu_1)\alpha_1 &= 2d_{\text{eff}}\alpha_3\alpha_2^* + \sqrt{2\gamma_1}\alpha_1^{\text{in}} + \sqrt{2\mu_1}\beta_1^{\text{in}}, \\ \tau\delta\dot{\alpha}_2 + (\gamma_2 + \mu_2)\alpha_2 &= 2d_{\text{eff}}\alpha_3\alpha_1^* + \sqrt{2\gamma_2}\alpha_2^{\text{in}} + \sqrt{2\mu_2}\beta_2^{\text{in}}, \\ \tau\delta\dot{\alpha}_3 + (\gamma_3 + \mu_3)\alpha_3 &= -2d_{\text{eff}}\alpha_1\alpha_2 + \sqrt{2\gamma_3}\alpha_3^{\text{in}} + \sqrt{2\mu_3}\beta_3^{\text{in}},\end{aligned}$$

with cavity round trip time  $\tau = \frac{1}{\text{FSR}}$ , field amplitudes  $\alpha_i = \bar{\alpha}_i + \delta\alpha_i$ , one pass losses  $\gamma_i$  and  $\mu_i$  associated with the output mirror and the remaining loss mechanisms, respectively. The linewidth reads  $\Delta\omega = \frac{2\gamma'_i}{\tau}$  with  $\gamma'_i = \gamma_i + \mu_i$ . The input fields  $\alpha_{\text{in}}$  and  $\beta_{\text{in}}$  are the incoupling vacuum fields related to the coupling mirror and the losses, respectively.

Assuming high mirror reflectivities, we can write  $r_i \approx 1 - \gamma_i$  and  $t_i \approx \sqrt{2\gamma_i}$  for  $\gamma \ll 1$ . The fluctuations of the field amplitudes  $\delta\alpha_i$  are coupled via

$$\begin{aligned}\tau\delta\dot{\alpha}_1 + \gamma'_1\delta\alpha_1 &= \sqrt{\gamma'_1\gamma'_2}\delta\alpha_2^* + \sqrt{\gamma'_3\gamma'_1}(\sigma - 1)\delta\alpha_3 + \sqrt{2\gamma_1}\delta\alpha_1^{\text{in}} + \sqrt{2\mu_1}\delta\beta_1^{\text{in}}, \\ \tau\delta\dot{\alpha}_2 + \gamma'_2\delta\alpha_2 &= \sqrt{\gamma'_2\gamma'_1}\delta\alpha_1^* + \sqrt{\gamma'_3\gamma'_2}(\sigma - 1)\delta\alpha_3 + \sqrt{2\gamma_2}\delta\alpha_2^{\text{in}} + \sqrt{2\mu_2}\delta\beta_2^{\text{in}}, \\ \tau\delta\dot{\alpha}_3 + \gamma'_3\delta\alpha_3 &= -\sqrt{\gamma'_3\gamma'_2}(\sigma - 1)\delta\alpha_2 - \sqrt{\gamma'_3\gamma'_1}(\sigma - 1)\delta\alpha_1 + \sqrt{2\gamma_3}\delta\alpha_3^{\text{in}} + \sqrt{2\mu_3}\delta\beta_3^{\text{in}},\end{aligned}$$

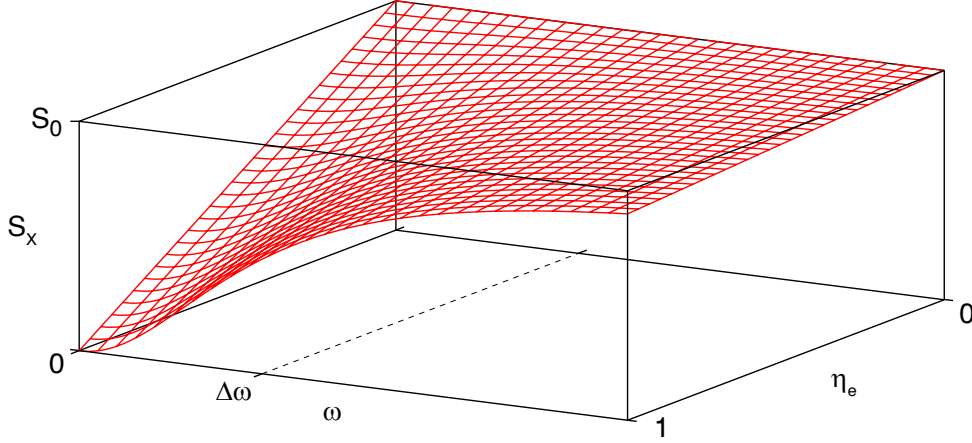


**Figure 6.5** – Variance of the twin beams' amplitude difference, as a function of sideband frequency  $\omega$  and escape efficiency  $\eta_e$ . For symmetric cavity parameters of signal and idler field the noise spectrum of the amplitude difference is permanently below the vacuum noise variance  $S_0$ . The effect is independent of the pump power and perfect correlation can theoretically be obtained at sideband frequency  $\omega = 0$ .

where  $\sigma = \sqrt{\frac{P}{P_{\text{thr}}}}$  contains the nonlinear coupling within the optical threshold power  $P_{\text{thr}}$ . The output field is given by Equation (B.4)

$$\alpha_i^{\text{out}} = \sqrt{2\gamma_i} \alpha_i - \alpha_i^{\text{in}}.$$

The noise spectra of the amplitude and phase quadratures are directly given by the variances of the output field fluctuations (compare with Equation (2.38))

$$S_{x_i}(\omega) = \langle (\delta x_i^{\text{out}})^2 \rangle, \quad S_{p_i}(\omega) = \langle (\delta p_i^{\text{out}})^2 \rangle.$$

For the amplitude difference  $X = (x_1 - x_2)/\sqrt{2}$  the cavity equation of motion is independent of pump fluctuations, which cancel in the difference. In the symmetric case, i.e. signal and idler cavity are identical ( $\gamma = \gamma_i, \mu = \mu_i$ ), the amplitude difference noise spectrum reads

$$S_X(\omega)/S_0 = \frac{4\mu\gamma' + \omega^2\tau^2}{4\gamma'^2 + \omega^2\tau^2} = 1 - \frac{\eta_e}{1 + \left(\frac{\omega}{\Delta\omega}\right)^2}, \quad (6.2)$$

where  $\eta_e = \frac{1-R}{1-R+L}$  is the cavity escape efficiency,  $\Delta\omega$  the linewidth and  $S_0$  the vacuum noise reference. In Figure 6.5 the amplitude difference is depicted as a function of sideband frequency  $\omega$  and escape efficiency  $\eta_e$ .

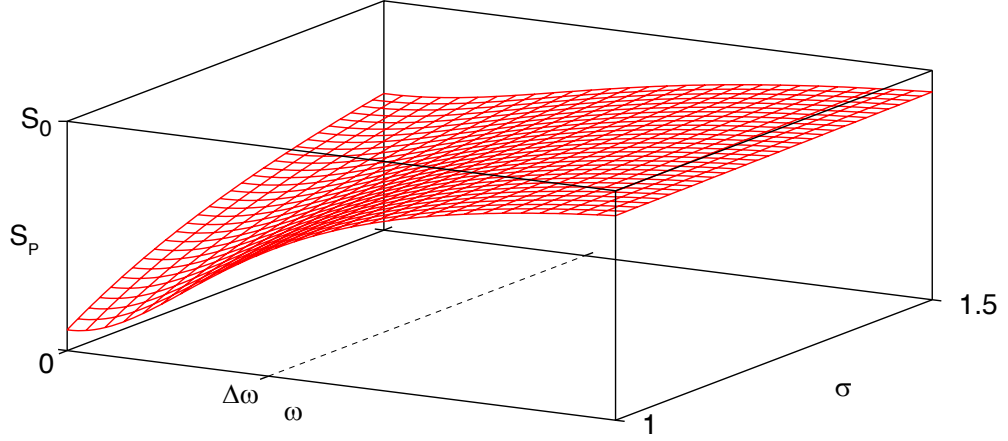


**Figure 6.6** – Variance of the phase sum in the symmetric case, as a function of sideband frequency  $\omega$  and pump power  $\sigma$ . For the same cavity parameters of signal and idler field the noise spectrum of the phase difference drops below vacuum noise variance  $S_0$ . The escape efficiency is set to  $\eta_e = 0.91$ .

The phase sum, given by  $P = (p_1 + p_2) / \sqrt{2}$ , is sensitive to pump fluctuations and depends on the pump power ratio  $\sigma$

$$S_P(\omega)/S_0 = 1 + \frac{4\gamma\gamma'}{\omega^2\tau^2 + 4\gamma'^2\sigma^2} = 1 - \frac{\eta_e}{\left(\frac{\omega}{\Delta\omega}\right)^2 + \sigma^2}. \quad (6.3)$$

Thus, we expect the best correlation at threshold.

An interesting feature occurs for single beams at high pump powers. The intensity fluctuation spectrum of a single beam is given by

$$\begin{aligned} S_{x_1}(\omega) &= \frac{S_0}{2} \left( 1 - \frac{8\gamma\gamma'^3\sigma(\sigma-2)}{(\omega^2\tau^2 + 4\gamma'^2) [\omega^2\tau^2 + 4\gamma'^2(\sigma-1)^2]} \right) \\ &= \frac{S_0}{2} \left( 1 - \frac{\eta_e \cdot \sigma(\sigma-2)}{2 \left[ 1 + \left(\frac{\omega}{\Delta\omega}\right)^2 \right] \left[ (\sigma-1)^2 + \left(\frac{\omega}{\Delta\omega}\right)^2 \right]} \right). \end{aligned}$$

Hence, each beam of the twins is separately squeezed in its amplitude for pump powers higher than four times the threshold power. Figure 6.7 shows the spectrum over sideband frequency and pump power.  $S_0/2$  denotes the vacuum noise limit for a single beam. At pump powers  $\sigma > 2$  the noise spectrum falls below the vacuum reference. The maximum obtainable noise reduction is a factor of two, i.e.  $-3$  dB, for  $\sigma \rightarrow \infty$  and  $\eta_e = 1$ .

For unequal signal and idler cavities, we obtain a noise enhancement for low frequencies. Figure 6.8 shows the amplitude difference noise of the twin beams in the

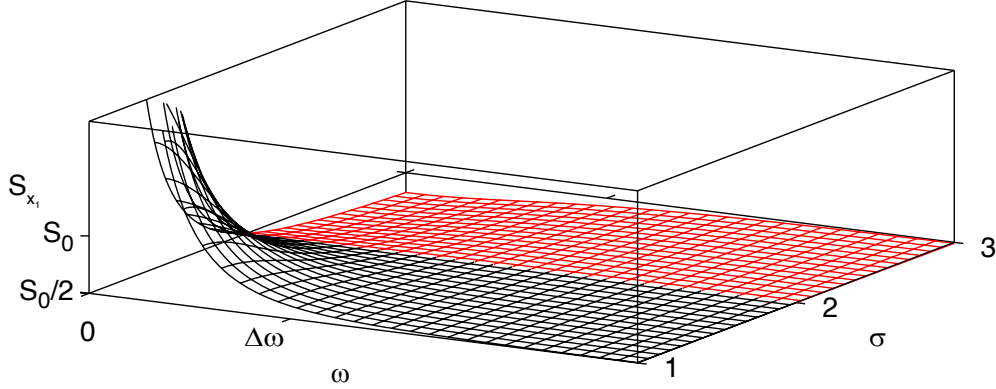


**Figure 6.7** – Amplitude noise spectrum of a single twin beam. At pump powers higher than four times the threshold ( $\sigma > 2$ ) the noise falls below the vacuum reference of a single beam  $S_0/2$  (red area).

asymmetric case, plotted as a function of sideband frequency  $\omega$  and difference factor between the cavities linewidth  $\delta\Delta\omega = \frac{\Delta\omega_1}{\Delta\omega_2}$ . The more the cavities differ, the higher the noise at small frequencies. For equal cavity parameters ( $\delta\Delta\omega = 1$ ), we obtain the result of the symmetric case. For the sake of completeness we state the asymmetric intensity difference spectrum

$$S_I(\omega) = 1 + \frac{N}{D}, \quad (6.4)$$

with the abbreviation  $N$  and  $D$  given as

$$\begin{aligned} N = & 8\gamma'_1\gamma'_2 \left\{ \left[ \omega^2\tau^2 + (1+b)^2(\gamma'_1 + \gamma'_2)^2 \right] \left[ g_d^2 - b^2g_s^2 - \omega^2\tau^2\gamma_1\gamma_2 \right] \right. \\ & + \Phi(\Phi - b\Phi_3) \left[ \omega^2\tau^2(1+2b)(\gamma_1\gamma_2)(\gamma_1\gamma_2'^2 - \gamma_2\gamma_1'^2) \right. \\ & \quad \left. \left. + g_d^2(\gamma'_1 - \gamma'_2)^2 + (1+2b)(\gamma'_1 + \gamma'_2)^2 g_d^2 \right] \right. \\ & + b\Phi_3(b\Phi_3 - \Phi) \left[ \omega^2\tau^2(g_s^2 + \gamma_1\gamma_2(\gamma'_1 + \gamma'_2)^2) - 2b(1+b)g_s^2(\gamma'_1 + \gamma'_2)^2 - 4\gamma'_1\gamma'_2 g_d^2 \right] \\ & \left. + (\Phi - b\Phi_3)^2 \left[ (\gamma'_1 - \gamma'_2)^2 g_d^2 \Phi^2 - (\gamma'_1 + \gamma'_2)^2 g_s^2 \Phi_3^2 b^2 \right] \right\}, \end{aligned}$$

$$\begin{aligned} D = & g_s \left\{ \omega^2\tau^2 \left[ \omega^2\tau^2 - 4b\gamma'_1\gamma'_2 - (\gamma'_1 + \gamma'_2)^2 \left[ (1+b)^2 + (\Phi - b\Phi_3)^2 \right] + 4\gamma'_1\gamma'_2\Phi(\Phi - b\Phi_3) \right] \right. \\ & \left. + 4(\gamma'_1 + \gamma'_2)^2 \left[ (\omega^2\tau^2 - 2b\gamma'_1\gamma'_2)(1+b) + 2\gamma'_1\gamma'_2 b\Phi_3(\Phi - b\Phi_3) \right]^2 \right\}, \end{aligned}$$

with  $b = \sqrt{\gamma'_1\gamma'_2}(\sigma - 1)/(1 + \Phi_3^2)$ ,  $g_s = \gamma_1\gamma'_2 + \gamma_2\gamma'_1$ ,  $g_d = \gamma_1\gamma'_2 - \gamma_2\gamma'_1$  and the pump and signal field resonance detunings  $\Phi_3 = \varphi_3/\gamma'_3$  and  $\Phi = \varphi_1/\gamma'_1 = \varphi_2/\gamma'_2$ .

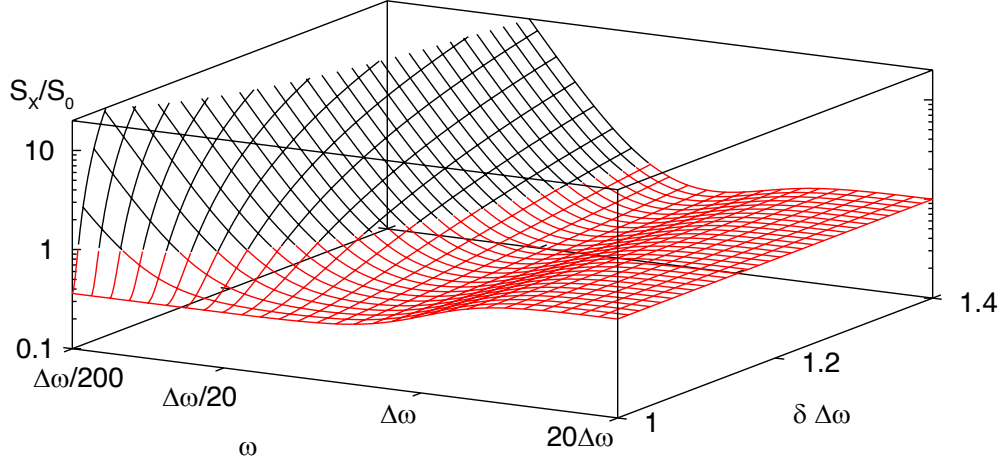


**Figure 6.8** – Variance of the amplitude difference in the asymmetric case, as a function of sideband frequency  $\omega$  and difference factor between the cavities linewidth  $\delta\Delta\omega$ . The more the cavities differ, the higher the noise at small frequencies. For the same cavity parameters ( $\delta\Delta\omega = 1$ ), we obtain the result of the symmetric case. The escape efficiency is set to  $\eta_e = 0.66$ .

In the case of two unequal cavities, the resonance condition of signal, idler and pump field is important. An operation of the signal and idler cavities not exactly on-resonance worsens the effect, as depicted in Figure 6.9.

### 6.2.1 A Bipartite Entanglement Criterion

The presence of quantum correlations in the amplitude and phase quadrature of the twin beams also imply the presence of entanglement. In order to verify this, we use a necessary and sufficient entanglement criterion suitable for bipartite Gaussian states that was introduced by L. M. Duan *et al.* in 2000 [81]. They considered the EPR-like operators

$$\begin{aligned}\hat{u} &= |a| \hat{x}_A + \frac{1}{a} \hat{x}_B, \\ \hat{v} &= |a| \hat{p}_A - \frac{1}{a} \hat{p}_B\end{aligned}$$

for the two parties Alice (A) and Bob (B) and proved that the sum of the variances of these operators must be larger than a specific bound for separable states

$$\langle(\Delta\hat{u})^2\rangle + \langle(\Delta\hat{v})^2\rangle \geq \frac{1}{2} \left( a^2 + \frac{1}{a^2} \right).$$

For  $a = 1$  we obtain the criterion in its strongest and most intuitive form

$$\mathcal{I} = \langle(\Delta(\hat{x}_A + \hat{x}_B))^2\rangle + \langle(\Delta(\hat{p}_A - \hat{p}_B))^2\rangle \geq 1. \quad (6.5)$$



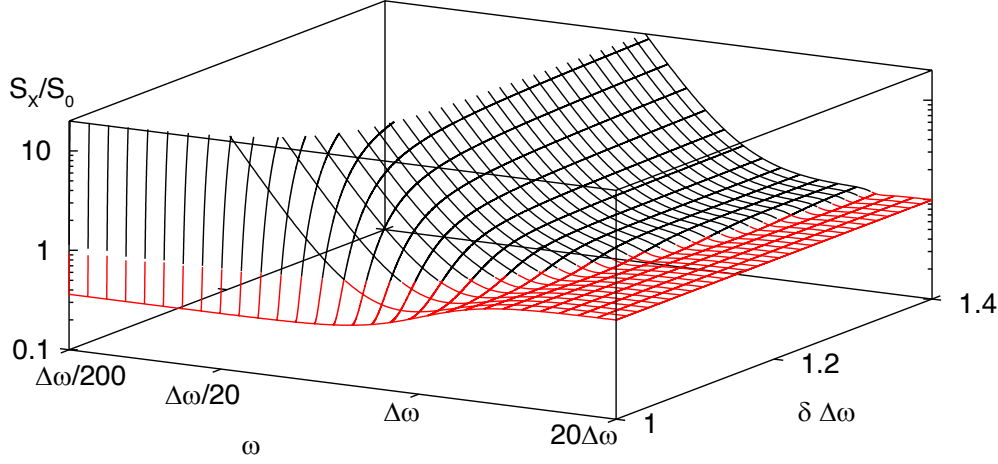


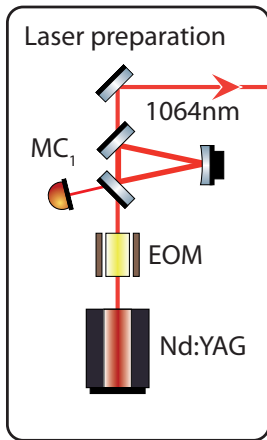
**Figure 6.9** – Variance of the amplitude difference in the asymmetric case, where the cavities are not on-resonance ( $\Phi = 0.1$ ). A strong degradation is visible; compare with Figure 6.8. Again, the resonance condition is not important for the same cavity parameters ( $\delta\Delta\omega = 1$ ).

Introducing uncorrelated vacuum noise with individual variances  $\langle(\Delta\hat{x}_{\text{vac}}^\theta)^2\rangle = 1/4$  gives a bound value of  $\mathcal{I} = 1$ . Entangled states are more strongly correlated than vacuum noise and lead to an inseparability value  $\mathcal{I} < 1$ .

## 6.3 Experimental Components

In this section we will review the experimental components used to generate amplitude correlations and bipartite entanglement between the bright twin beams at 810 nm and 1550 nm.

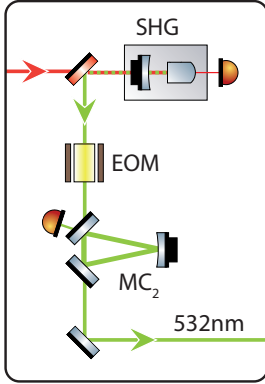
### 6.3.1 Laser



The output of 1.6 W was sent directly to the second-harmonic generation (SHG) cavity.

The main laser source was a Neodymium-doped Yttrium Aluminum Garnet (Nd:YAG) solid state laser. The device used – model *Mephisto* by *Inno-Light* – provided a single-mode output field at 1064 nm with an optical power of 2.1 W. The laser beam was first sent through a three-mirror ring cavity ( $MC_1$ ) with a finesse of  $\mathcal{F} = 260$ , corresponding to a linewidth of 2.7 MHz. Reduction of mode distortions of the laser's  $TEM_{00}$  spatial mode profile and technical noise at frequencies much higher than the cavity's linewidth were ensured. The cavity length was controlled using the Pound-Drever-Hall (PDH) locking scheme [69] with a phase modulation at a sideband frequency of 15 MHz. The

### 6.3.2 Second-Harmonic Generation (SHG)



The SHG was made of a 7% doped  $\text{MgO}:\text{LiNbO}_3$  crystal. The curved back surface of the crystal had a high-reflection coating ( $R = 99.96\%$ ) whereas the flat surface had an anti-reflection coating ( $R < 0.05\%$ ) for both wavelengths. The SHG had an out-coupling mirror with power reflectivities of  $R_{1064\text{nm}} = 90\%$  and  $R_{532\text{nm}} < 4\%$ . The modulation sidebands transmitted through  $\text{MC}_1$  at 15 MHz were used to control the cavity length with the PDH locking scheme. The second-harmonic field thus generated had a power of 1 W.

A second filter cavity ( $\text{MC}_2$ ) was used to ensure a  $\text{TEM}_{00}$  spatial mode profile and to suppress technical noise of the pump beam. The finesse was  $\mathcal{F} = 560$ , corresponding to a linewidth of 1.3 MHz. An EOM was used to provide a phase modulation at either 29.5 MHz or 1.36 MHz to generate error signals to stabilize the length of  $\text{MC}_2$  and subsequent cavities, again using the PDH locking scheme.

### 6.3.3 Optical Parametric Oscillator

The entanglement between 810 nm and 1550 nm was generated in a monolithic standing wave nonlinear cavity. The nonlinear medium inside the cavity was a periodically poled Potassium Titanyl Phosphate (PPKTP) crystal. The wave vector matching was given at a temperature of  $68^\circ\text{C}$ , to which the crystal was stabilized actively. The length of the crystal was 8.9 mm and the coatings were chosen to form a cavity with a finesse of  $\mathcal{F} = 100$  for the twin beams. The linewidth of both modes was hence 91 MHz and the free spectral range was 9.15 GHz. The radii of curvature of 8 mm led to a waist size of  $24\ \mu\text{m}$  for the 532 nm pump beam, which simply double-passed the crystal. The threshold power varied between 70 mW and 130 mW, depending on the spatial mode matching, longitudinal mode and wave vector matching, i.e. crystal temperature. The bright output fields were co-propagating and spatially separated with a dichroic beam splitter (DBS). Figure 6.10 shows a measurement of one output wavelength produced by the OPO. The cavity's length was changed by constantly heating the nonlinear crystal. Wavelengths from 808 nm (1557 nm) up to 817 nm (1525 nm) could be produced in a reasonable temperature range from  $35^\circ\text{C}$  to  $80^\circ\text{C}$ . The wavelength was measured with the spectrometer *AVA AvaSpec-3648-USB2* by *Avantes*. The grating had 300 lines/mm and could resolve light from 360 nm to 1100 nm. The  $10\ \mu\text{m}$  slit allowed a resolution of 0.5 nm. At first, it seems that Figure 6.10 describes a linear relationship with wavelength  $\lambda(T) = -0.22 \cdot T \frac{\text{nm}}{^\circ\text{C}} + 825\ \text{nm}$ ,  $T$  measured in  $^\circ\text{C}$ . Looking closer, however, the temperature dependence uncovers the occurrence of several mode hops and cluster jumps, as shown in Figure 6.11.

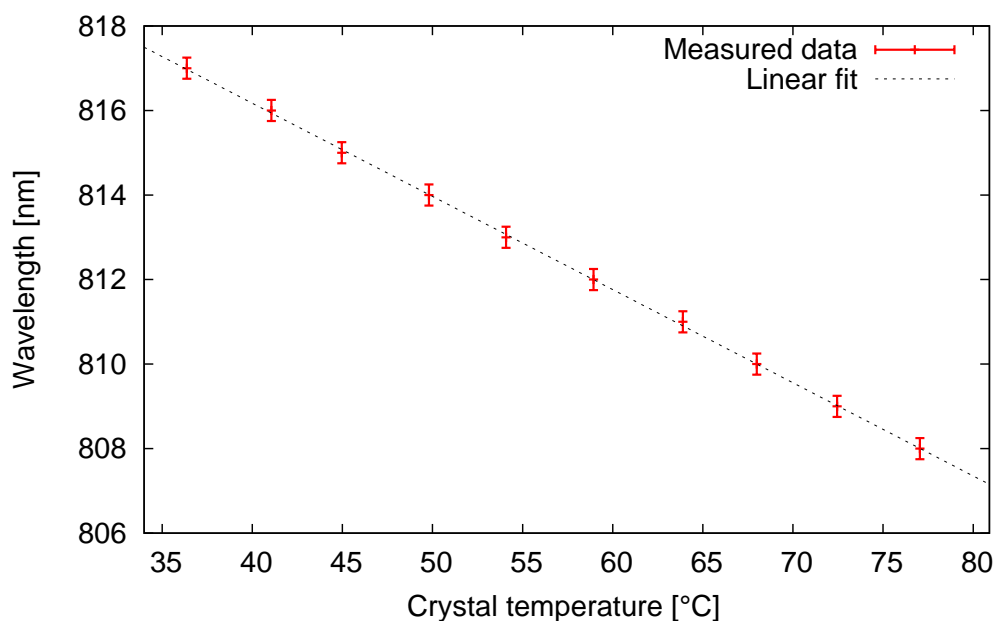


**Figure 6.10** – Measurement of one output wavelength produced by the OPO. The cavity’s length was changed by constantly heating the nonlinear crystal. At first, this seems to be a linear relationship.

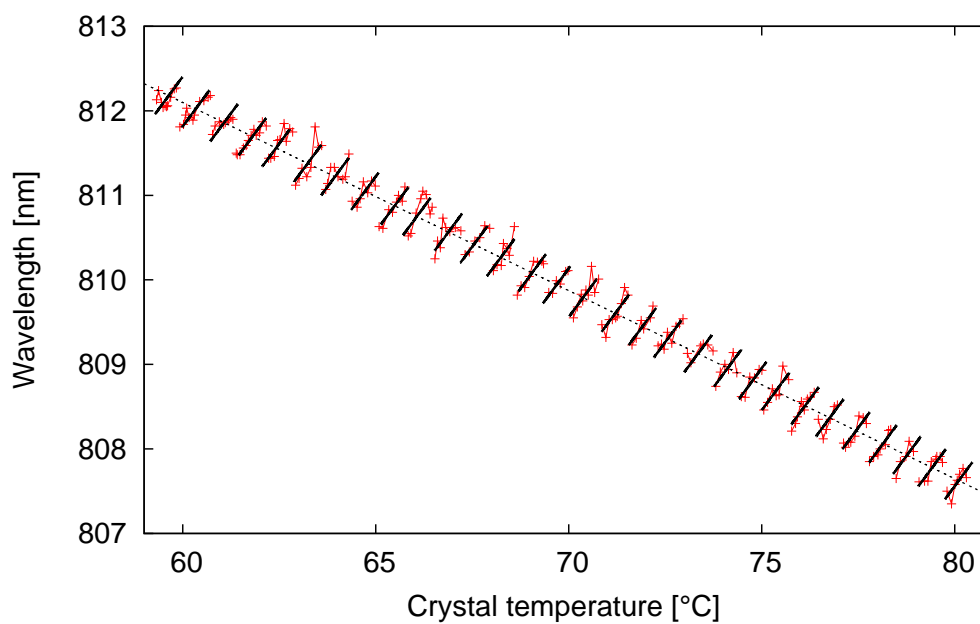


**Figure 6.11** – Measurement of one output wavelength produced by the OPO. The cavity’s length was changed by tuning its temperature. As illustrated in Figure 6.3, several mode hops and cluster jumps occur. Each cluster is marked with a solid black line. The spacings between the red measurement points within one cluster represent mode hops.

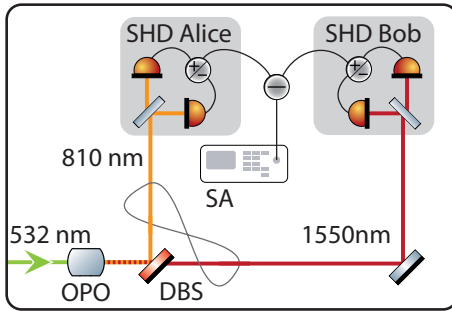
Figure 6.12 depicts the output power of the twin beams at 810 nm over input pump power at 532 nm. Special care was taken to avoid mode hops during pump power increase. The two traces depict measurements at different crystal temperatures, i.e. at different longitudinal modes. The resulting conversion efficiency, given by the ratio of output over input photons

$$\eta_c = \frac{n_{810}}{n_{532}} = \frac{P_{810} \cdot 810}{P_{532} \cdot 532},$$

is shown in Figure 6.13. Depending on the mode and pump power, conversion efficiencies greater than 74% were obtained.

## 6.4 Amplitude Correlation Measurement

### 6.4.1 Experimental Setup



The amplitude correlations of the twin beams were measured with the adjoining setup. The co-propagating fields were separated with a dichroic beam splitter (DBS), which reflects 810 nm (yellow, signal) and transmits 1550 nm (red, idler). The noise was measured with a self homodyne detector (SHD) at each party. The SHD consists of a 50/50 beam splitter and two photo-detectors. Subtracting the detector's signals yields the vacuum noise, adding them yields to the amplitude fluctuations of the considered field, as described in Section 4.1. Silicon PIN diodes *S5971* from Hamamatsu and Indium Gallium Arsenide diodes *FCI-InGaAs-300* from OSI Optoelectronics were used for detecting the signal and idler field, respectively. The electrical difference and sum signals were obtained with the passive power combiner *PMT-1+* from Mini-Circuits. Passive variable voltage dividers were implemented to equalize the electrical gain of each detector. The electronic signals were analyzed and recorded with the spectrum analyzer (SA) *FSP* from Rohde & Schwarz. The common mode rejection ratio of the difference was measured to be greater than 40 dB.

### 6.4.2 Results

Figure 6.14 shows the measurement results of the best obtained amplitude correlation. The output power of the signal field was slightly above threshold ( $P_{810} = 2.4$  mW) and the measurement frequency was chosen as 20 MHz. The traces are normalized to the vacuum noise (black, dashed), which was obtained from the detectors' difference signals. The detectors' dark noise is different for the difference (grey, dashed) and the sum (grey, dotted) signal due to the power combiner. Taking both into account and

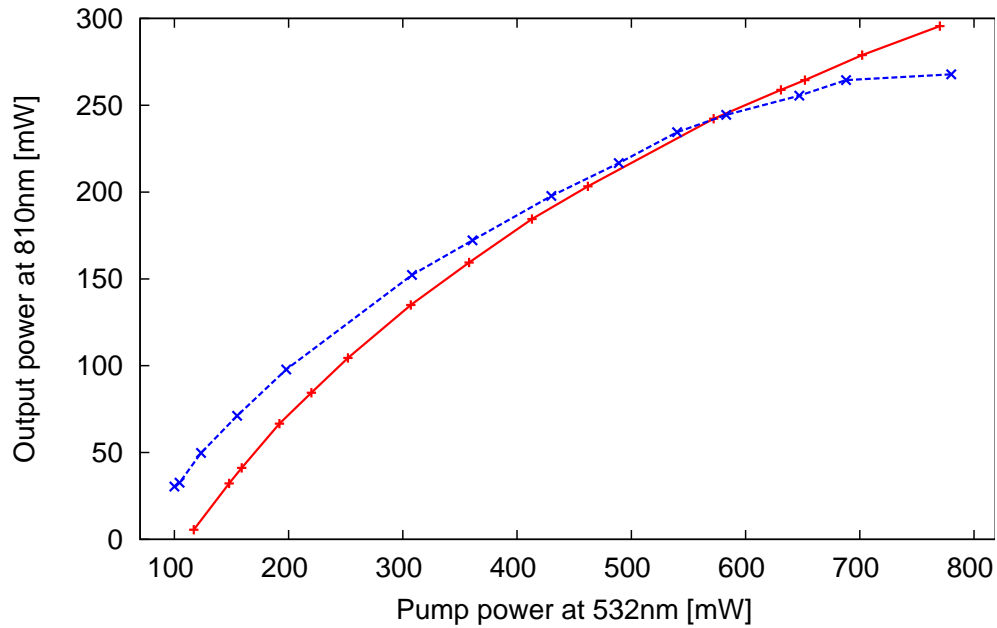


**Figure 6.12** – OPO output power at 810 nm over 532 nm pump power. Special attention was paid to avoid mode hops during pump power increase. The two traces depict measurements at different crystal temperatures, i.e. at different longitudinal modes.

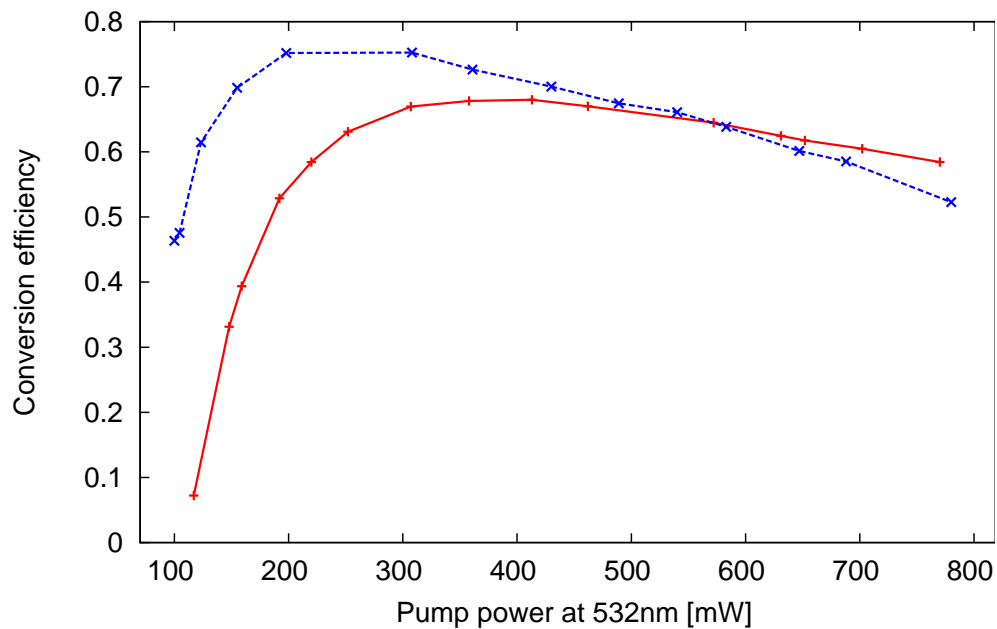


**Figure 6.13** – OPO photon number down-conversion efficiency deduced from Figure 6.12.

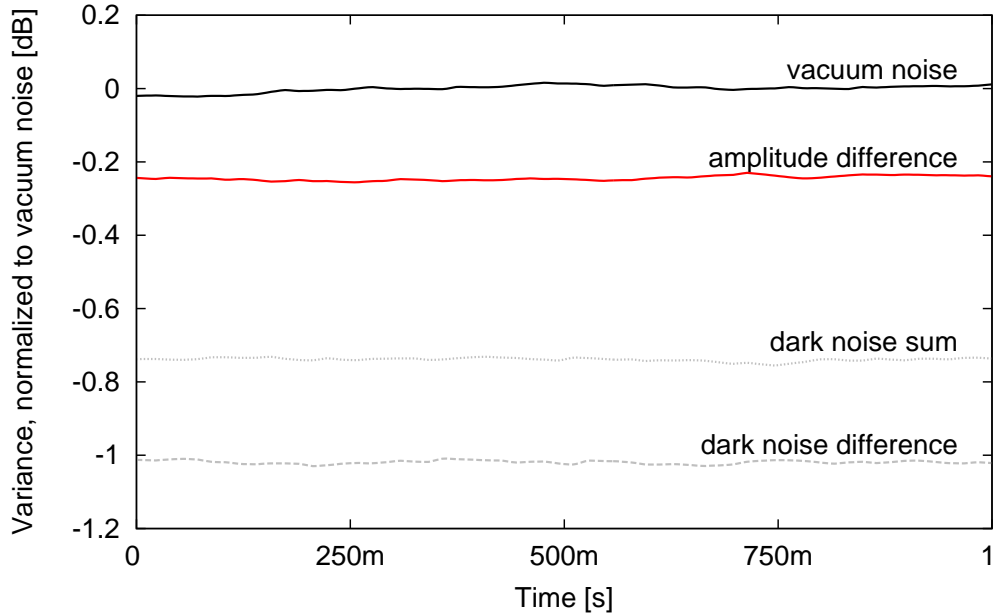


**Figure 6.14** – Zero span measurement of the amplitude difference (red) with signal power  $P_{810} = 2.4$  mW at 20 MHz. The measured signal is averaged 20 times. The vacuum noise (black, dashed) is obtained from the detectors’ difference signals. The dark noise is different for the difference (grey, dashed) and the sum (grey, dotted) signal due to the power combiner.

correcting the obtained signals for the dark noise contribution, the amplitude difference falls approximately 3 dB below the vacuum noise reference (see Figure 6.15). Due to fluctuations of the OPO cavity it was impossible to obtain a constant output below 2.4 mW signal power. Since a constant level is needed to obtain a reliable vacuum noise reference, noise properties closer to threshold could not be analyzed. Furthermore, the dark noise clearance decreases for smaller light powers and impairs the measurement quality.

The correlation’s dependence on the signal field power is shown in Figure 6.16. The higher the signal field power, the smaller the quantum correlation. The amplitude correlation of a perfect system should be independent of the threshold ratio  $\sigma$  (Equation (6.2)). As soon as the cavity parameters differ and the fields are not exactly on-resonance of the cavity modes, however, the fluctuation spectrum depends on the threshold ratio  $\sigma$ , see Section 6.2. The measurements have not been averaged but were dark noise corrected.

A spectrum of the amplitude difference is shown in Figure 6.17. It was recorded with a signal power of  $P_{810} = 4.8$  mW and is dark noise corrected. At frequencies above 12 MHz the amplitude fluctuations fall below the vacuum noise reference. This seems surprising since the correlations should get stronger at smaller sideband frequencies

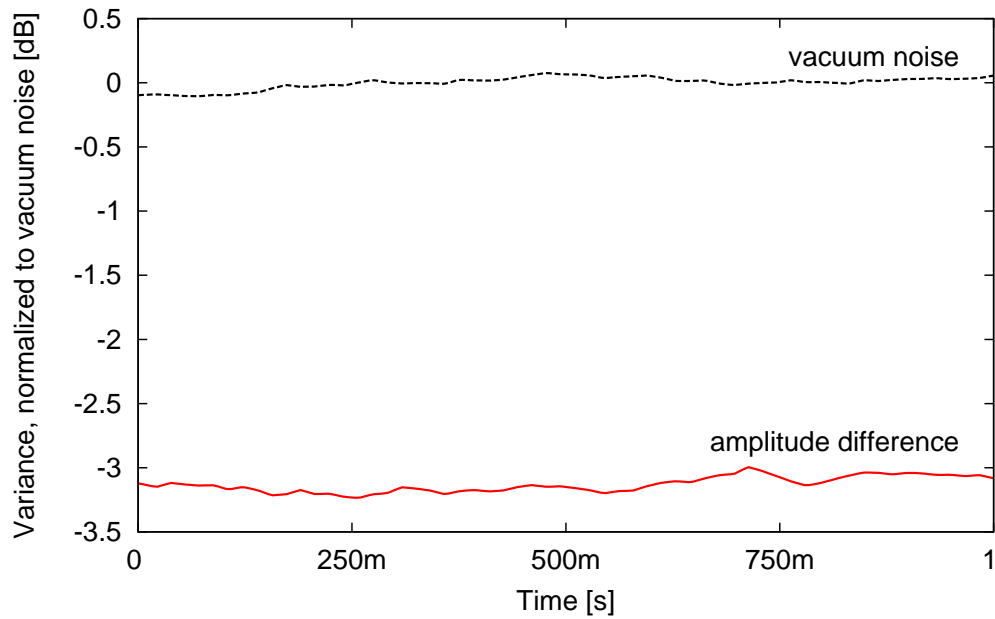


**Figure 6.15** – Dark noise corrected result from Figure 6.14. Taking the different dark noise contributions into account yields an amplitude difference of about 3 dB below the vacuum noise reference.

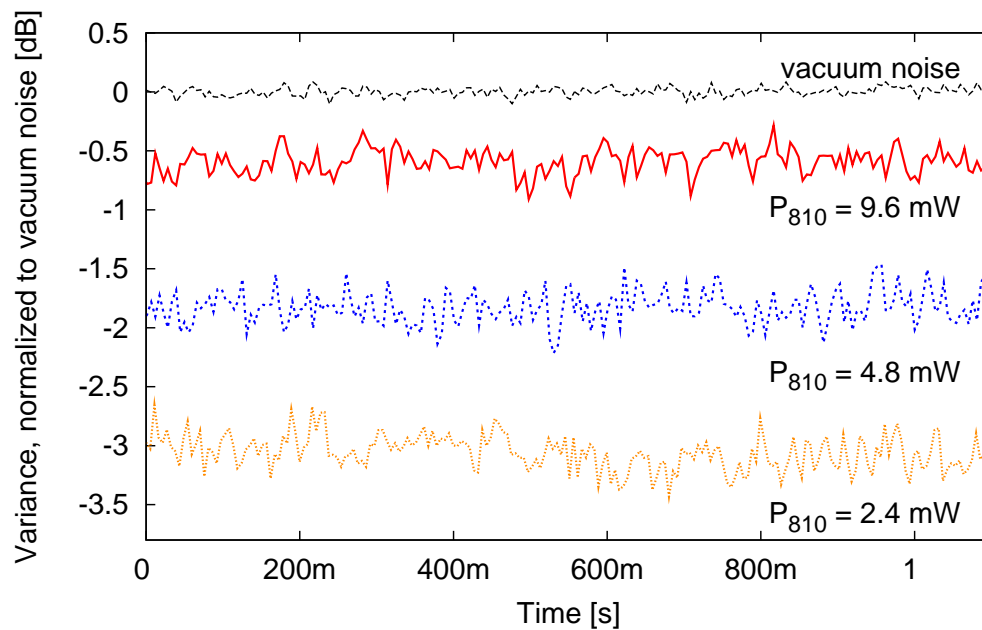


**Figure 6.16** – Amplitude difference measurement over signal power at 20 MHz. The higher the signal field power the smaller the quantum correlation. The data is not averaged but corrected for dark noise.

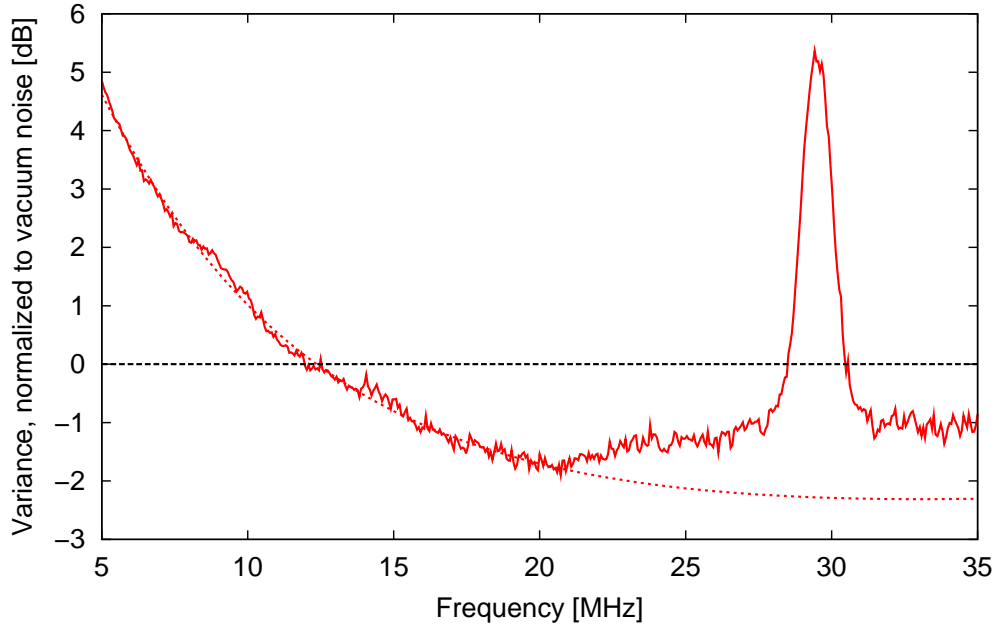


**Figure 6.17** – Spectrum of the amplitude difference with  $P_{810} = 4.8$  mW. The measured data (red, solid) is in good agreement with the theory (red, dashed) for frequencies below 20 MHz. Above 20 MHz the frequency-dependent power combiners and the photo-detectors’ bandwidth cause a noise increase. The peak at 29.5 MHz originates from a phase modulation.

(compare with Figure 6.5). According to Equation (6.4) this is, however, possible if the cavities’ signal and idler linewidth differ by about 0.2% and the fields are thus not exactly on-resonance but detuned by  $\Phi = 1.02$ . In terms of linewidth this corresponds to a tiny fraction of  $\frac{\varphi}{\Delta\omega} = \frac{\Phi}{2\text{FSR}} \ll 1$ . The threshold ratio is set to  $\sigma = 1.2$  and the quantum efficiency of the photo-detectors is estimated to be  $\eta_q = 85\%$ . The dashed red line shows the expected fluctuation spectrum according to Equation (6.4). At frequencies above 20 MHz the noise increases. This is caused by a frequency-dependent behavior of the power combiners, different transfer functions of the photo-detectors at higher frequencies and their limited bandwidth. The peak at 29.5 MHz arose from the locking phase modulation for  $\text{MC}_2$ .

## 6.5 Entanglement Measurement

### 6.5.1 Experimental Setup

To measure the entanglement between the bright twin beams, balanced homodyne detectors (BHDs, see Section 4.1 for details) were used to analyze the amplitude and phase quadratures of the two fields. To provide local oscillators (LOs) for the



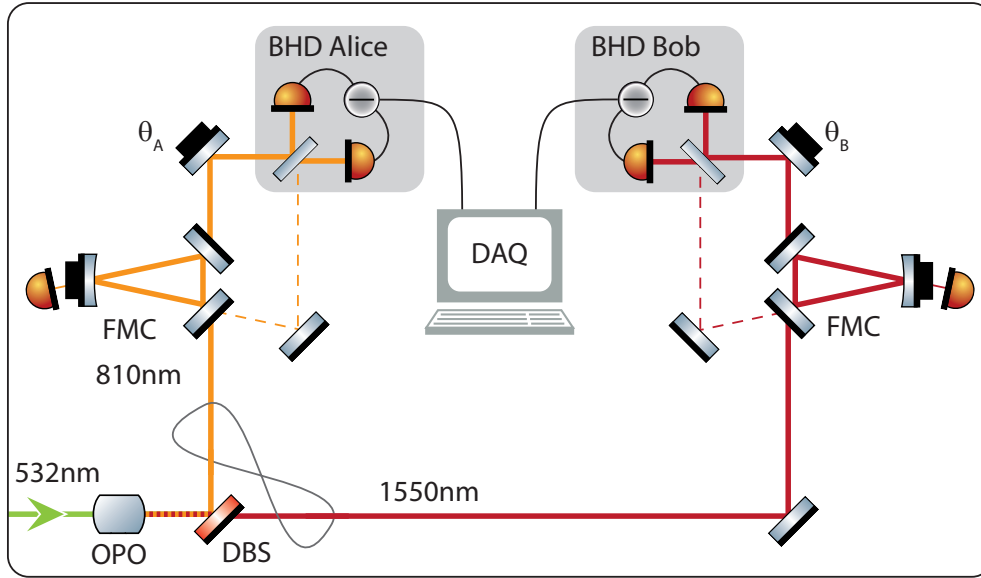


**Figure 6.18** – Schematic of the entanglement setup. The generated twin beams are sent to filter cavities (FMCs) in order to spatially separate the sideband and carrier fields. The latter are transmitted through the FMCs and serve as local oscillators for the balanced homodyne detection (BHD). The reflected sidebands of the twin beams are probed. A data acquisition system (DAQ) is used to record and analyze the data.

BHDs, filter mode cleaners (FMCs) were introduced to separate the carrier from the sideband fields [82]. The experimental setup is shown in Figure 6.18. The filter cavities were triangular ring resonators with a finesse of  $\mathcal{F} \approx 400$  for signal and idler modes, respectively. The twin beams were separated by a dichroic beam splitter (DBS), sent to their corresponding filter cavity and analyzed in a BHD. An error signal was generated with the PDH scheme [69] using the down-converted phase modulation of the green pump field at 1.36 MHz. The transmitted beam served as optical LO. The reflected part – containing the quantum properties of interest – and the LO were superimposed at the 50/50 beam splitter. The detection took place with a purpose-built photodetector, where the photo-currents were directly subtracted and resonantly enhanced at 63.9 MHz on the circuit board. Both BHD signals were demodulated, low pass filtered at 50 kHz and sampled with the 14 bit analog-to-digital converter *PCI-6133* from **National Instruments**. The calculation of the variances of each signal and the variance of the difference of the two signals were conducted by a *Labview* script, without correcting the data for the contribution of electronic dark noise. To verify a constant LO power, the DC voltages of the FMCs were monitored.

To perform the measurement, the OPO was pumped with 130 mW and operated

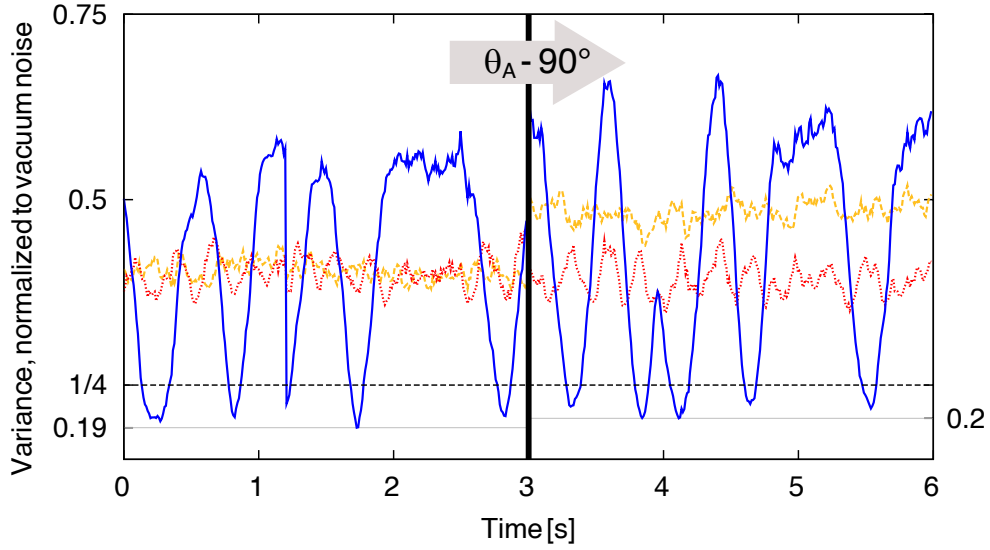


**Figure 6.19** – Demonstration of entanglement between the twin beams at Alice’s and Bob’s sites. Bob’s BHD phase is repeatedly ramped and Alice’s phase is switched from  $\hat{x}$  (left) to  $\hat{p}$  (right). The dotted green and dashed red traces correspond to the variances measured on the individual beams at Alice’s and Bob’s site, respectively. The minima of the two blue traces correspond to half the variances in Equation (6.5) thereby fulfilling the inequality with  $\mathcal{I} = 0.78 < 1$ .

slightly above threshold. 2.7 mW and 1.4 mW LO powers were obtained, which led to a dark noise clearance of 4 and 6 dB for the 810 nm and 1550 nm detectors, respectively.

### 6.5.2 Results

Figure 6.19 presents the measurement results. Time series of Alice’s variance (dashed yellow), Bob’s variance (dotted red), and half the variance of the two mode’s difference ( $1/2 \cdot \langle (\Delta(\hat{x}_A^\varphi - \hat{x}_B^\theta))^2 \rangle$ , blue) are shown. The BHD phase  $\theta_B$  at Bob’s site was repeatedly ramped and Alice’s site was switched from an amplitude (left) to a phase measurement (right). The vacuum noise levels of the detectors were measured and used to normalize the traces. The individual variances show a non-uniform noise distribution among the quadratures. According to Equation (6.3), the fluctuation spectrum of the phase sum depends on the pump power ratio  $\sigma$ . Hence, we expect a larger noise contribution in the phase quadrature.

In order to verify the state’s entanglement properties, the inseparability criterion from Equation (6.5) was checked. The minima of the blue trace on the left side correspond to measurements where Alice and Bob were set to their amplitude quadrature (yellow and red trace, lower noise) with  $1/2 \cdot \langle (\Delta(\hat{x}_A - \hat{x}_B))^2 \rangle = 0.19$ . On the right side the minima

of the blue trace correspond to measurements where Alice and Bob were set to their phase quadrature (yellow and red trace, high noise) with  $1/2 \cdot \langle (\Delta(\hat{p}_A + \hat{p}_B))^2 \rangle = 0.2$ . In both cases the mode's difference noise (blue) drops below the vacuum noise reference. The sum of the minima yields an inseparability value of  $\mathcal{I} = 2 \cdot (0.19 + 0.2) = 0.78 < 1$ ; this corresponds to a quadrature entanglement of about  $-1$  dB.

## 6.6 Discussion

In this chapter, an optical parametric oscillator was operated above threshold to generate light with non-classical properties. Quantum amplitude correlations between its twin beams at 810 nm and 1550 nm were observed and their characteristics understood. Furthermore, quantum phase correlations were shown and bipartite entanglement between the bright fields was verified.

From a practical point of view, the operation above threshold holds some disadvantages. The correlations are largest close to threshold. Unfortunately, small perturbations, e.g. in the temperature, crystal length or pump power, cause fluctuations in the optical output power of the twin beams. This impeded the correct acquisition of a vacuum noise reference. In the worst case the operation point of the OPO went below threshold and no bright output beams were produced. This led to a loss of lock of the following filter cavities and the data acquisition was interrupted. More sophisticated stabilization schemes of pump power, crystal temperature or length should be investigated in the future to overcome this problem. Close to threshold, optical light power is quite low and the detector's electronic dark noise plays a significant role. Either more sensitive detection electronics is desirable or external local oscillators are needed to probe the fields independently of their power and fluctuations. External local oscillators also allow the operation of the OPO below threshold. This causes, however, the problem to stabilize the local oscillators to the optical frequencies of the dim signal and idler fields.

The diversity of the twin beams' cavities led to a noise increase at small sideband frequencies. An increase in the cavities' linewidth changes this behavior dramatically and could be used to overcome this problem.

Furthermore, the generation of bright twin beams at 810 nm and 1550 nm is useful to implement a quantum frequency converter, which we discuss in the following chapter.



---

## Quantum Frequency Conversion

---

In the field of metrology, the measurement sensitivity of laser interferometers can be enhanced by employing quantum states. This was recently realized in the gravitational wave (GW) detector GEO 600 by combining ultra-stable coherent light with squeezed vacuum states at a laser wavelength of 1064 nm [40]. Assuming a fixed laser power, the sensitivity of such interferometers can still be improved by increasing the squeezing factor and by reducing the laser wavelength. The combination of both approaches is not easy to achieve, since material properties of the nonlinear squeezing media limit the generation of squeezed vacuum states at short, e.g. visible, wavelengths. One solution is the frequency up-conversion of squeezed states from near-infrared wavelengths.

In this chapter the experimental frequency up-conversion of a dim continuous-wave coherent light field from 1550 nm to 532 nm is demonstrated with a high conversion efficiency. We discuss the potential to generate strongly squeezed vacuum states at 532 nm with this technique.

### 7.1 Quantum Theory of Sum-Frequency Generation

In Section 2.1.2 we discussed the classical sum-frequency generation. To see that the quantum properties of a converted state are preserved, we take the Hamiltonian of the interaction [83]

$$\hat{H}_{\text{int}} = i\hbar\chi' (\hat{a}_3^\dagger \hat{a}_1 \hat{a}_2 - \hat{a}_3 \hat{a}_1^\dagger \hat{a}_2^\dagger)$$

and consider the case of sum-frequency generation: two photons of frequency  $\omega_1$  and  $\omega_2$  annihilate and combine to a photon of frequency  $\omega_3$ .  $\chi'$  denotes the nonlinear coupling constant and is proportional to the nonlinear susceptibility  $\chi^{(2)}$ . Considering a strong

pump field  $\omega_2$ , which we assume not to be affected by the interaction and can therefore be treated classically, yields the reduced Hamiltonian

$$\hat{H}_{\text{int}} = i\hbar\chi \left( \hat{a}_3^\dagger \hat{a}_1 - \hat{a}_3 \hat{a}_1^\dagger \right),$$

where the coupling constant is now proportional to the pump field  $\chi = \chi' \cdot \langle \hat{a}_2 \rangle$ . The time evolution is given by Heisenberg's equation of motion

$$\frac{d\hat{a}}{dt} = \frac{i}{\hbar} [\hat{H}, \hat{a}] + \frac{\partial \hat{a}}{\partial t}$$

and yields the coupled wave equations for  $\hat{a}_1$  and  $\hat{a}_3$ , which do not have an explicit time dependence ( $\partial_t \hat{a}_1 = \partial_t \hat{a}_3 = 0$ ),

$$\begin{aligned} \frac{d\hat{a}_1}{dt} &= \frac{i}{\hbar} [\hat{H}_{\text{int}}, \hat{a}_1] + \frac{\partial \hat{a}_1}{\partial t} & \frac{d\hat{a}_3}{dt} &= \frac{i}{\hbar} [\hat{H}_{\text{int}}, \hat{a}_3] + \frac{\partial \hat{a}_3}{\partial t} \\ &= \frac{i}{\hbar} i\hbar\chi [\hat{a}_3^\dagger \hat{a}_1 - \hat{a}_3 \hat{a}_1^\dagger, \hat{a}_1] & &= \frac{i}{\hbar} i\hbar\chi [\hat{a}_3^\dagger \hat{a}_1 - \hat{a}_3 \hat{a}_1^\dagger, \hat{a}_3] \\ &= -\chi \hat{a}_3, & &= \chi \hat{a}_1. \end{aligned}$$

The solution of these differential equations is given by

$$\begin{aligned} \hat{a}_1(t) &= \hat{a}_1(0) \cos(\chi t) - \hat{a}_3(0) \sin(\chi t), \\ \hat{a}_3(t) &= \hat{a}_3(0) \cos(\chi t) + \hat{a}_1(0) \sin(\chi t). \end{aligned} \tag{7.1}$$

This results in a complete conversion of the quantum states at time  $t = \frac{\pi}{2\chi}$

$$\hat{a}_1(t = \pi/2\chi) = -\hat{a}_3(0), \quad \hat{a}_3(t = \pi/2\chi) = \hat{a}_1(0).$$

Depending on the interaction time and on the strength of the coupling – and hence on the pump power's square root – an entire energy and quantum state transfer can occur between the interacting fields. Figure 7.1 shows the characteristic of the single pass conversion efficiency. For a high nonlinear coupling ( $\chi'_1$ ) the pump power  $P_1$  is needed to reach the maximum of the conversion efficiency. Reducing the nonlinear coupling ( $\chi'_2$ ), e.g. by increasing the wave vector mismatch, more pump power ( $P_2$ ) is needed to reach the maximum. The curve thus becomes flatter.

## 7.2 Frequency Conversion of a Coherent State

This section describes the experimental realization and characterization of the sum-frequency converter. The conversion efficiency of the device was investigated by converting a coherent light field from 1550 nm to 532 nm.

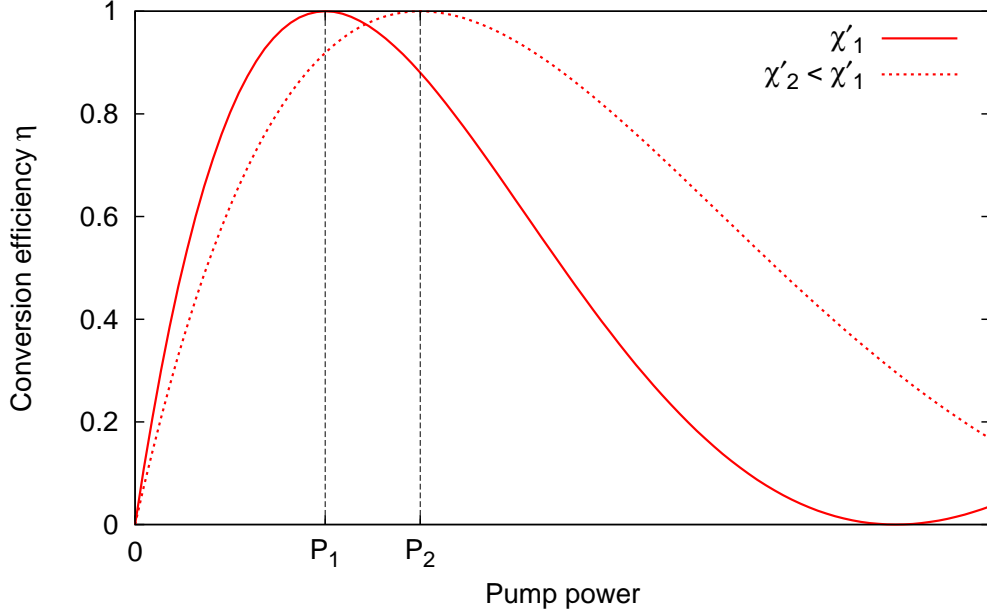


**Figure 7.1** – Conversion efficiency dependence on pump power for a single pass through the crystal. The smaller the nonlinear coupling  $\chi'$ , the more pump power is needed to reach the conversion maximum. Hence, a flatter curve is obtained for a larger wave vector mismatch.

### 7.2.1 Experimental Setup

To convert a signal field from 1550 nm to 532 nm a strong pump field at 810 nm is needed. The pump and signal fields were produced as described in Section 6.3. The monolithic OPO was operated far above threshold and light powers of up to 200 mW at 810 nm and 104 mW at 1550 nm were available.

The pump field at 810 nm was sent through a variable attenuator ( $\lambda/2$ -wave plate and polarizing beam splitter (PBS)) and coupled into the sum-frequency generator (SFG). The SFG was built as a standing-wave two-mirror nonlinear cavity. The nonlinear medium inside the cavity was a PPKTP crystal. The phase matching for 810 nm and 1550 nm was given at a temperature of 67°C, to which the crystal was stabilized actively. The length of the crystal was 9.3 mm and the cavity was defined by two external mirrors with reflectivities of  $R_{\text{in}} = (96.5 \pm 0.5)\%$  (left mirror) and  $R_{\text{trans}} > 99.9\%$  (right mirror) for signal and pump beam, as depicted in Figure 7.2. The mirrors' radii of curvature of 25 mm and the air gaps of 17 mm between mirrors and crystal led to a waist size of about  $w_0 = 50 \mu\text{m}$  for the pump beam. Furthermore, the mirrors had reflectivities at 532 nm of  $R > 99.9\%$  (left) and  $R < 0.1\%$  (right) to ensure that all the converted light leaves the SFG to the right. The length of the cavity was actively controlled with the PDH scheme [69], using a frequency modulation of the pump light at 24.5 MHz. The

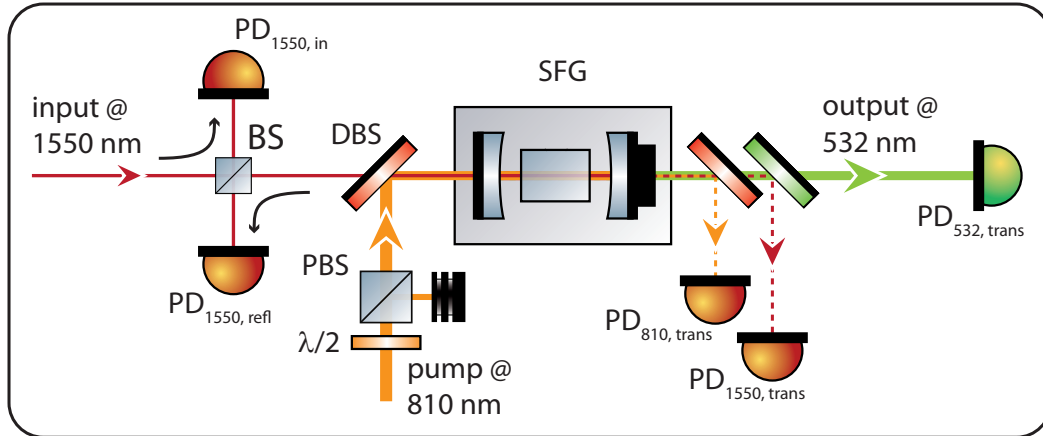


**Figure 7.2** – Schematic of the setup. The pump beam at 810 nm (yellow) with tunable power is sent into the sum-frequency generator (SFG). A 4 mW signal beam at 1550 nm (red) is sent through a 50/50 beam splitter (BS) to monitor the input power with the photo-detector  $PD_{1550,in}$ . Half of the signal is overlapped with the pump beam at a dichroic beam splitter (DBS) and coupled into the SFG. Half of the light power reflected off the cavity is detected at  $PD_{1550,refl}$ . In transmission of the SFG, the optical fields are separated by another set of DBSs and detected with the corresponding photo-detectors  $PD_{532,trans}$ ,  $PD_{810,trans}$  and  $PD_{1550,trans}$ . All signals from the photo-detectors are recorded with a data acquisition system and analyzed with PC software.

losses in the system are mainly due to the anti-reflective coatings of the crystal surfaces and the absorption of the crystal itself. They can be combined to a total cavity round trip loss that was measured to be  $\mu_{810} = 0.99\%$  and  $\mu_{1550} = 0.42\%$ .

The signal field at 1550 nm (red) was attenuated using a  $\lambda/2$ -wave plate and a PBS (not shown in the figure) and its power was monitored with photo-detector  $PD_{1550,in}$  (see Figure 7.2). 2 mW were overlapped with the pump beam at a dichroic beam splitter (DBS) and coupled into the SFG cavity. Half of the light power reflected off the cavity was detected at  $PD_{1550,refl}$ . In transmission of the SFG cavity, the optical fields were separated by a set of DBSs and detected with the corresponding photo-detectors  $PD_{532,trans}$ ,  $PD_{810,trans}$  and  $PD_{1550,trans}$ . All signals from the photo-detectors were recorded with a data acquisition system (*PCI-6133* from **National Instruments**) and analyzed with PC software (*Labview*). Figure 7.3 shows the photo-detector's signal of transmitted pump (yellow) and signal (red) field for two distinct resonance conditions. On simultaneous resonance of both wavelengths (right side) conversion occurs and the signal field collapses.



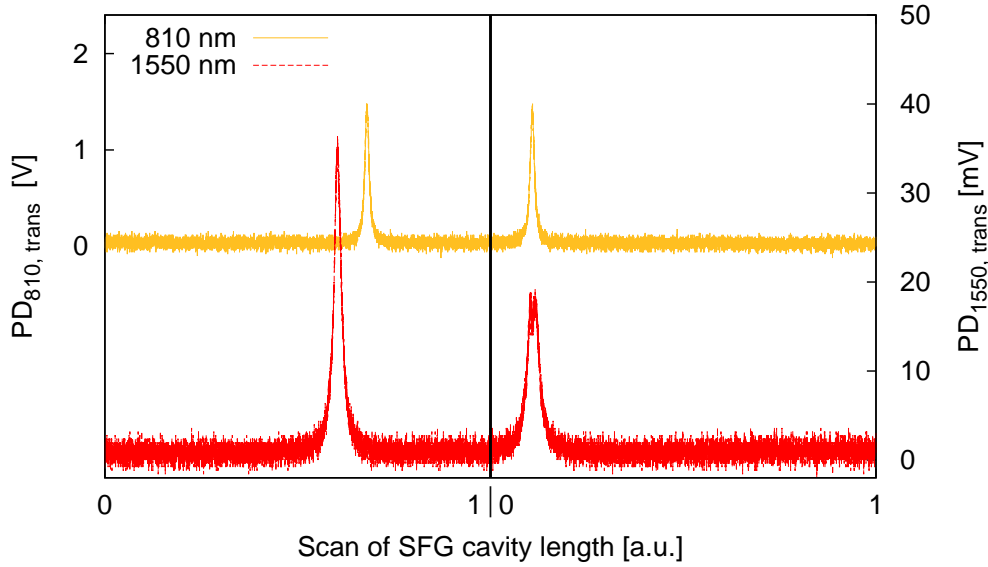


**Figure 7.3** – Airy peaks of the SFG cavity’s transmitted pump (top) and signal field (bottom). Depending on the crystal’s temperature, consecutive (left) or simultaneous (right) resonance is given. On both sides the cavity is scanned over the same length. For simultaneous resonance, the signal field collapses and is converted to 532 nm. A reduction of the pump field is not visible, since the field is much more intense.

### Cavity Properties

The cavity of the SFG was formed by two meniscal lenses with radii of curvature of 25 mm at the inside and 20 mm at the outside. The outside had an anti-reflective (AR) coating, specified with a reflectivity smaller than 0.1% at a wavelength of 1550 nm. Although the reflectivities of the AR coatings are small, parasitical cavities occur at perpendicular incidence. Assuming 0.1% reflectivity and perfect mode overlap, the impedance matching is affected substantially. Figure 7.4 shows a simulation (implemented in *Finesse* [84]) of the impedance matching. The reflected light power is normalized to the input power and plotted against the phase detunings (i.e. length change) of the parasitical cavities. Depending on the length change of each mirror, between 71% and 77% of the input light is reflected. This effect must be taken into account when measuring the relative depletion of the signal field (see Section 7.2.2). A calibration on maximal reflectance and transmittance is important prior to each measurement. The simulation was performed for mirrors with reflectivities of 99.72% and 96.31%.

Since the wavelength tunability of the OPO’s output fields exceeded several nanometers, the wavelength dependence of the SFG cavity’s mirror coatings had to be taken into account. According to the design reflectivities, the anti-reflective coating of the

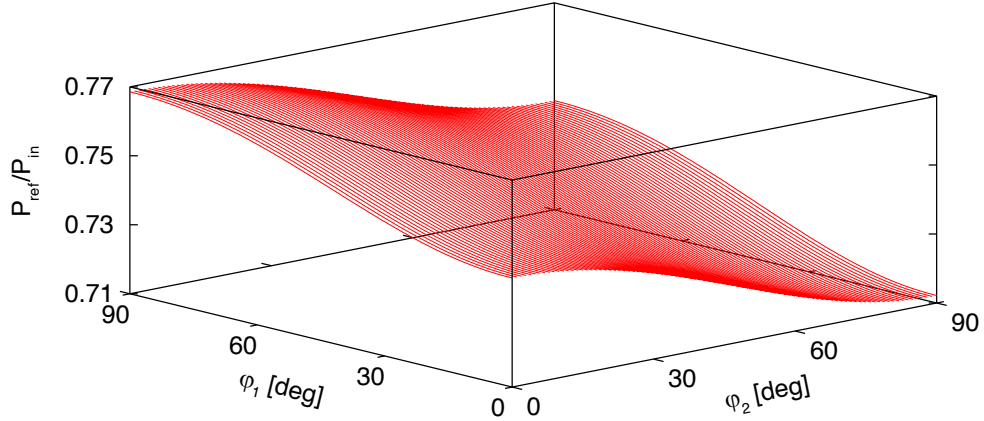


**Figure 7.4** – Optical impedance of the SFG cavity with parasitical cavities due to the mirrors’ AR coatings of 0.1%. The SFG cavity is assumed to be lossless and the mirror reflectivities are 99.72% and 96.31%. Depending on the phases of the parasitical cavities, between 71% and 77% of the input light is reflected.

signal field was the most sensitive. Figure 7.5 shows design reflectivities of signal and pump field against the wavelength detuning with respect to 810 nm. The pump field reflectivity is rather constant, whereas the signal field reflectivity exhibits a strong alteration. This could lead to small variations in the signal’s round trip loss and affect the conversion efficiency.

### 7.2.2 Measurement Methods

To characterize the conversion efficiency, the light powers of the optical fields were measured with the photo-detectors mentioned above; these being calibrated with power meters. The SFG cavity’s conversion efficiency, based on the respective photon number ratio, is given by

$$\eta = \frac{n_{532}}{n_{1550}} = \frac{532 \cdot P_{532}}{1550 \cdot P_{1550}} = \gamma \cdot \frac{532 \cdot P_{532}^{\text{meas}}}{1550 \cdot P_{1550}^{\text{meas}}}. \quad (7.2)$$

The calibration factor  $\gamma$  compensates the errors in the absolute calibration of the power meters and thus the actually measured power levels  $P_{\lambda}^{\text{meas}}$ .

To determine  $\gamma$ , the depletion of the signal field at 1550 nm was measured in reflection and in transmission of the cavity, respectively. When no pump light was coupled into the SFG, the light reflected by the cavity far from its resonance, corresponding to the total incident power, and the light transmitted by the cavity on resonance were

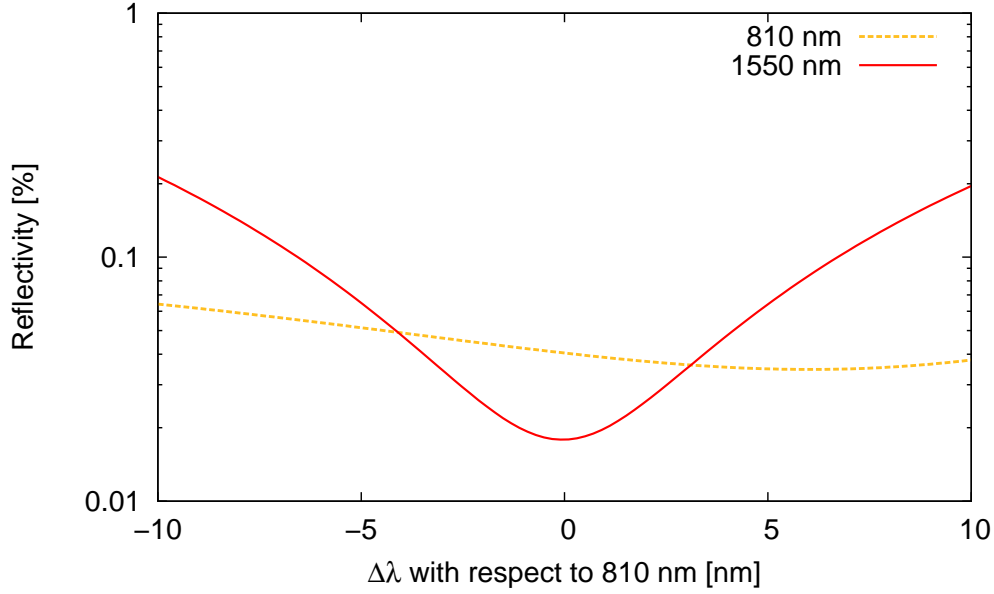


**Figure 7.5** – Design AR coatings of the SFG cavity’s coupling mirrors. Changing the wavelength results in an alteration of the intra-cavity loss.

measured and normalized to unity. The relative depletion

$$\begin{aligned} \delta &= 1 - \left( \frac{P_{\text{refl}} + P_{\text{trans}}}{P_{\text{in}}} \right) \\ &= 1 - \left( \frac{P_{\text{refl}}}{P_{\text{refl,max}}} + \underbrace{\frac{P_{\text{trans,max}}}{P_{\text{refl,max}}}}_{\kappa} \cdot \frac{P_{\text{trans}}}{P_{\text{trans,max}}} \right) \end{aligned} \quad (7.3)$$

depends on the normalized signals and on the ratio of the maximal transmitted and reflected power  $\kappa$ . In low loss systems, the relative depletion is a measure for the conversion efficiency [85] and Equation (7.3) yields the same results as Equation (7.2). Due to the finesse of  $\mathcal{F}_{1550} = 150$  and to the round trip loss  $\mu_{1550} = 0.41\%$ , the two differ. However, the relative depletion is used to provide a better fit to the theoretical model and to obtain the correction factor  $\gamma$  from Equation (7.2). Thus, both methods were required to obtain an accurate value for the conversion efficiency.

To measure the conversion efficiency the pump power was varied. For each pump power, time series of all photo-detectors were recorded simultaneously and analyzed in a *Labview* script.

### 7.2.3 Numerical Simulations

To compare the measured data with a theoretical model, the system was simulated numerically. Therefore, the PC software *nics*, a numerical nonlinear cavity simulator

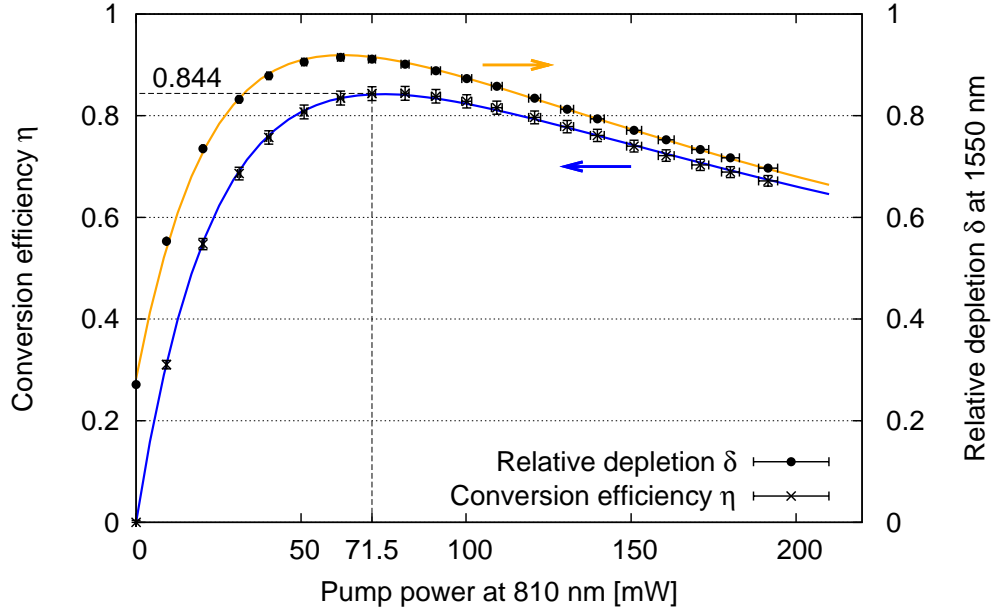


**Figure 7.6** – Measurement results. The conversion efficiency (blue) and relative depletion (yellow) are shown as a function of pump power. The conversion efficiency reaches its maximum of  $(84.4 \pm 1.5)\%$  at 71.5 mW pump power. The solid lines correspond to a numerical simulation of the system.

written by Nico Lastzka [86], was utilized. By providing the system’s parameters – in particular the wavelengths, light powers, waist size, mirror reflectivities and the crystal’s index of refraction, nonlinearity, absorptions and wave vector mismatch – the expected output fields were calculated.

To fit the model to the experimental data, all these parameters needed to be adjusted. To speed up the procedure, a *Python* script was written that implemented the *Nelder-Mead* fitting algorithm [87]. Taking the power- or depletion-measurement on their own, several possible parameter sets were found and no unique solution was identifiable. Hence both measurements were fitted simultaneously. Since the depletion-measurement depends only on relative power measurements, the power-measurement’s calibration factor  $\gamma$  could be obtained and reasonable unique solutions were found for each measurement.

#### 7.2.4 Measurement Results

Figure 7.6 shows the first measurement result. The conversion efficiency (blue) and the relative depletion (yellow) are plotted against the pump power. The solid lines depict the numerical simulations of the system fitted to the data. The simulations are in excellent agreement with the measurements and support the experimentally obtained

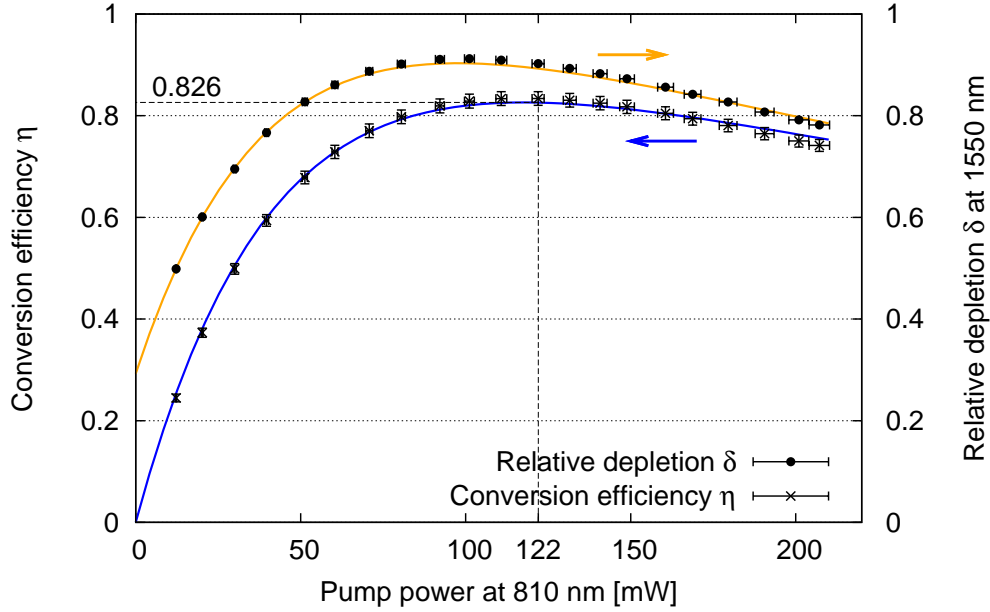


**Figure 7.7** – Another measurement set with phase mismatch  $\Delta\varphi = 0.28\pi$ . The curve’s shape is stretched and the conversion efficiency reaches its maximum of  $(82.6 \pm 1.5)\%$  at 122 mW pump power.

conversion efficiency of  $(84.4 \pm 1.5)\%$ . As predicted for sum-frequency generation, energy is transferred back and forth between the interacting fields (Equation (7.1)). Hence, the conversion efficiency drops after reaching its maximum at a pump power of 71.5 mW. The numerical simulation of conversion efficiency and relative depletion determined the calibration factor of the power meters to  $\gamma = 1.03$ , which is within the specified error range of the power meters. These measurements were taken with a phase mismatch of  $\Delta\varphi = 0.12\pi$ , where  $\Delta\varphi = \Delta kL/2$  is the wave vector mismatch set with respect to the crystal’s length  $L$  (see Section 6.1).

Changing the phase mismatch by selecting another longitudinal mode (cf. Figure 6.3) results in the measurement depicted in Figure 7.7. The phase mismatch is  $\Delta\varphi = 0.28\pi$  and the conversion efficiency reaches its maximum of  $(82.6 \pm 1.5)\%$  at 122 mW pump power. The curve’s shape is stretched, since the nonlinear coupling is decreased. More pump power was needed to obtain the conversion maximum.

The absolute conversion efficiency changes because the temperature of the SFG crystal was tuned as well as the temperature of the monolithic OPO in order to find an optimal operation point. Hence slightly different signal and idler wavelengths were produced, the AR coatings exhibited different reflectivities and the total round trip loss changed. This led to a small change in the conversion efficiency. Table 7.1 compares the fitted parameters of the two measurements.

**Table 7.1** – Comparison of the two measurements’ fit results. The phase vector matching  $\Delta\varphi$  shows the most significant difference. The steep curve shape of Figure 7.6 exhibits a better phase matching than the flat curve shape of Figure 7.7.

Parameter	Steep curve shape	Flat curve shape
$\gamma$	1.033	1.024
$\mu_{1550}$ [%]	0.42	0.45
$\Delta\varphi$ [ $\pi$ ]	0.124	0.276
$\eta$	0.844	0.826

### 7.3 Discussion

In this chapter, the process of sum-frequency generation was used to convert a coherent light field from 1550 nm to 532 nm. The conversion efficiency was found to be greater than 84% by the combination of two independent measurement methods. In order to verify the system’s parameters, it was simulated numerically and fitted to the measurements. Interestingly, the best fit results were obtained with mirror reflectivities that differed from the design reflectivities. The signal field’s end mirror was supposed to have a reflectivity of 99.97%. Instead, best fit results were obtained with an assumed reflectivity of 99.72%. An analysis showed that the present system could reach conversion efficiencies of more than  $\eta = 93\%$  if a mirror with reflectivity  $R_{1550,\text{in}} = 0.9$  would be used for the signal field.

With the obtained results it should be possible to convert a quantum state from 1550 nm to 532 nm with a high fidelity. The conversion efficiency of  $\eta = 84.4\%$  solely introduces  $\tau = 1 - \eta = 15.6\%$  losses, i.e. vacuum noise contribution. Considering the conversion of a squeezed state, more than  $-6$  dB squeezing should be obtainable at 532 nm if we use an input state at 1550 nm with a noise suppression of  $-10$  dB [41] (see Equation (3.7)).

Figure 7.8 depicts a possible setup to convert squeezed states from 1550 nm to 532 nm. In principle it works like the frequency conversion of a coherent state. In order to avoid any kind of loss the beam splitter at the input needs to be removed (cf. Figure 7.2). The 532 nm photo-detector at the output of the SFG cavity will be replaced by a homodyne detector to analyze the amplitude and phase quadratures of the converted state. The coherent input field at 1550 nm will be replaced by a squeezed field generated in a separate experiment. To ensure that all involved laser fields are set to the same frequency, a phase-lock loop (PLL) is needed. The OPO’s bright output field at 1550 nm will be superimposed with a part of the main laser of the squeezing generation on a 50/50 beam splitter. The beat note is detected with a photo-detector ( $\text{PD}_{1550,\text{PLL}}$ ) and used to generate an error signal for the phase-lock.

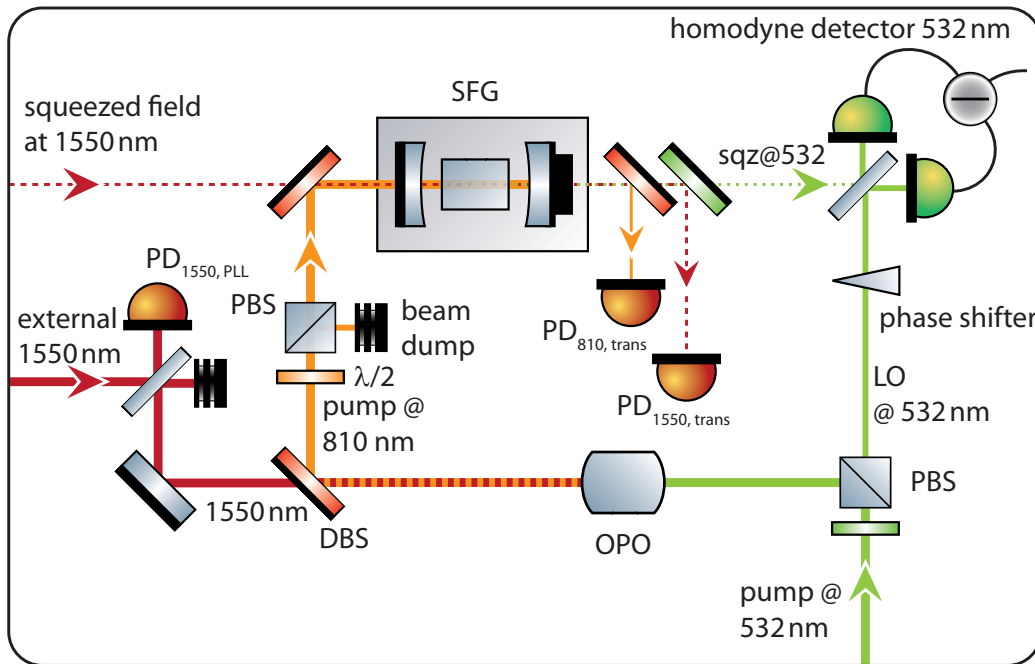


**Figure 7.8** – Squeezing conversion setup. The core of the squeezing conversion remains the SFG cavity. The 532 nm pump light produces bright twin beams at 810 nm and 1550 nm within the OPO and serves as a LO for the homodyne detection of the converted state. The generated 810 nm field is used to pump the SFG. The required power is adjusted at a variable attenuator ( $\lambda/2$ -wave plate and polarizing beam splitter (PBS)). The generated 1550 nm field is phase-locked to the carrier field of the experiment that produces the squeezed states by superimposing the two fields on a beam splitter. The beat signal provides the error signal. The externally generated squeezed field is then coupled into the SFG and the converted field is probed with a balanced homodyne detector.

Without phase-locking the two lasers, the local oscillator at 532 nm cannot be used as a stable phase reference for the squeezed field. As a last preparation step, the coherent control beam of the squeezer cavity will be converted to 532 nm. Thereby, optimal phase matching settings, i.e. crystal temperature, and the required pump power need to be figured out. Finally, the squeezed field will be converted.





## CHAPTER 8

---

### Summary and Outlook

---

Specific tasks in quantum information science and quantum metrology require the precise preparation of different quantum states. Within this thesis, states with a high potential for applications and fundamental research have been prepared and experimental techniques were demonstrated. These particular states were: an unconditional bound entangled state of light, and a bipartite entangled state between bright twin beams at the wavelengths of 810 nm and 1550 nm. The technique of sum-frequency generation was shown to convert a coherent field from 1550 nm to 532 nm. All states and techniques were performed in the CV regime with continuous-wave, quasi-monochromatic laser fields.

#### **Bound Entanglement**

Although there were claims of the experimental generation of bound entanglement in 2009 with a four-qubit bound entangled Smolin state [88, 89], the first convincing experiments, conducted in the DV regime, were published in 2010: an unconditional preparation with ions [90] and a conditional preparation with single photons [91]. Simultaneously, the generation of unconditional bound entanglement presented here was demonstrated [66]. It was the first experimental realization in the CV regime. The high significance of the state preparation ( $46\sigma$  away from being distillable,  $16\sigma$  away from being separable and  $53\sigma$  away from unphysical) demonstrated the high precision of the experimental platform, since bound entanglement in the CV regime was shown to be a rare phenomenon [92]. All predicted entanglement properties (NPT entangled, bound entangled and separable) were realized by moving through phase space. Unlike conditional preparation in the DV regime, unconditional preparation

opens the possibility to conduct further experiments with the generated state. The “superactivation” of channels with zero quantum capacity can now be realized, although the experimental challenge is still high [30, 31]. The experimental techniques, however, can be used for the accurate and precise control of further quantum state preparations. Furthermore, the investigation of general entanglement properties is of fundamental interest: the irreversible character of bound entanglement has triggered entire theoretical research programs [61], which try to link entanglement theory to a thermodynamical picture [28, 29]. The experimental realization can help to verify theoretical findings.

### **Twin Beam Entanglement**

In order to connect the optical wavelengths suitable for quantum memories and standard telecommunications fibers, a non-degenerated OPO was set up and operated above threshold. The quantum properties of its output fields at 810 nm and 1550 nm were investigated. Quantum amplitude correlations between the twin beams in the order of  $-3$  dB with respect to vacuum noise were observed and their characteristics understood. Furthermore, quantum phase correlations were shown and bipartite entanglement between the bright twin beams at 810 nm and 1550 nm in the order of  $-1$  dB was verified. A decreasing amount in quantum correlations at small sideband frequencies was observed. This effect was caused by the diversity of the twin beams’ cavity linewidth. Either equalizing the cavities’ linewidth or increasing the linewidth in general leads to an increase of quantum correlations at small frequencies. This was also demonstrated, at almost the same time, in a similar type of experiment by Li *et al.* [93, 94]. In order to improve the operation stability close to threshold, more sophisticated stabilization schemes of pump power, crystal temperature or length should be investigated. Future experiments could use this type of OPO to further close the gap between the DV and CV regimes. Hybrid experiments, with single photon counting modules (SPCMs) and homodyne detection, were used in the past to generate peculiar quantum states. Subtracting a single photon from a squeezed vacuum state or performing homodyne detection on number states led to the generation of Schrödinger kitten states [95, 96]. Operating the OPO below threshold, SPCMs could be used to detect single photons at 810 nm while the output field at 1550 nm is probed with high efficient homodyne detection. Heralded single photons at 1550 nm or single-photon-added quantum states could be realized.

### **Quantum Frequency Conversion**

In order to convert quantum states from one optical frequency to another, a sum-frequency generation was experimentally realized. A coherent light field at 1550 nm was converted to 532 nm with a conversion efficiency of more than 84%. The obtained

measurement results were in excellent agreement with the numerical model of the system. An analysis showed that reducing the reflectivity of the signal field's coupling mirror would increase the expected conversion efficiency to over 93%. Hence, the expected quantum fidelity of a converted squeezed state is rather high. Introducing a squeezed state with a noise suppression of  $-12.3$  dB at 1550 nm [41] should result in a noise suppression of over  $-9$  dB at 532 nm. This could be used to enhance the sensitivity of future gravitational wave detectors operating at 532 nm, such as *DECIGO* [42]. The sum-frequency generation can also be used to convert arbitrary quantum states, such as entangled states or single photons. The photon statistics of high quality quantum states, prepared at 1550 nm, can be investigated at 532 nm or implemented in hybrid experiments using SPCMs.

Although the field of quantum optics arose three and a half decades ago, it is still growing rapidly. Several papers are published every day all over the world and new theoretical ideas and proposals and experimental realizations appear. Arguably, the first “real” application of non-classical light was implemented last year in the gravitational wave detector GEO 600 in order to improve its sensitivity for a novel kind of astronomy [40]. When the first application suitable for daily use appears is uncertain. This work, however, contributes a small piece in the big puzzle of how to handle the “spooky action at a distance”.



# APPENDIX A

---

## Convex Optimization Problems

---

Convex optimization solves problems of the form

$$\begin{aligned} & \text{minimize } f_0(x) \\ & \text{subject to } f_i(x) \leq b_i, \quad i = 1, \dots, m. \end{aligned}$$

Let the functions  $f_0, \dots, f_m : \mathbb{R}^n \rightarrow \mathbb{R}$  be convex. They therefore satisfy the condition

$$f_i(\alpha x + \beta y) \leq \alpha f_i(x) + \beta f_i(y), \quad \forall x, y \in \mathbb{R}^n, \forall \alpha, \beta \in \mathbb{R}$$

with  $\alpha + \beta = 1, \alpha \geq 0, \beta \geq 0$ .

Ref. [97] gives a detailed discussion of convex optimization and is recommended for further reading.

### Matlab Code for Calculating Inseparability

We reconstructed and analyzed the covariance matrix using the *YALMIP* [98] and *SeDuMi* [99] toolboxes of the commercial *Matlab* software package (*MATLAB 2009b*, **The MathWorks Inc.**). The following code, written by Carlos Pineda [66], was used to calculate the inseparability of Section 5.1.1 for a given covariance matrix  $\gamma$  of  $N_A \times N_B$  modes.

```
1 % Calculating the Lambda matrix for N modes
2 function [out] = symplecticForm(N)
3 out = zeros(2*N, 2*N);
4 for k = 1:N
```

```
5     out(2*k-1, 2*k) = 1;
6     out(2*k, 2*k-1) = -1;
7 end
8
9 % Calculating the inseparability
10 x = sdpcvar(1);           % Defining solution matrix
11 GammaA = sdpcvar(2*NA); % Defining symmetric 2*NA submatrix
12 GammaB = sdpcvar(2*NB); % Defining symmetric 2*NB submatrix
13 F = set([]);           % Defining an empty set
14
15 % Add conditions to the set
16 F = F + set(gamma - [GammaA zeros(2*NA, 2*NB);
                      zeros(2*NB, 2*NA) GammaB] > 0);
17 F = F + set(GammaA + i/4*x*symplecticForm(NA) > 0);
18 F = F + set(GammaB + i/4*x*symplecticForm(NB) > 0);
19
20 % Solve set
21 sol = solvesdp(F, -x, sdpcsettings('verbose',0));
22
23 % Display solution
24 disp(double(xe))
```

## APPENDIX B

---

### Cavity Equations and Nonlinearities

---

To be able to describe the nonlinear interaction within an optical resonator, we follow [100] and derive the equations of motion of a cavity. Therefore, we rewrite the traveling wave solution of the electric field, see Equation (2.35), as the product of a mode-function  $\mathbf{u}_k(\mathbf{r})$  and an amplitude-function  $\hat{a}_k(t)$

$$\begin{aligned}\mathbf{E}(\mathbf{r}, t) &= \mathbf{E}^+(\mathbf{r}, t) + \mathbf{E}^-(\mathbf{r}, t) \\ &= -i \sum_k \mathcal{E}_\omega \mathbf{u}_k(\mathbf{r}) \hat{a}_k - i \sum_k \mathcal{E}_\omega \mathbf{u}_k(\mathbf{r}) \hat{a}_k^\dagger,\end{aligned}\quad (\text{B.1})$$

with  $\mathcal{E}_\omega = \sqrt{\hbar\omega/2\epsilon_0}$  and the time evolution of an harmonic oscillator

$$\dot{\hat{a}}_k = \frac{i}{\hbar} [\hat{H}, \hat{a}_k] = -i\omega \hat{a}_k.$$

Considering the case of a one-dimensional cavity the mode-function obeys the Helmholtz equation

$$\left(\Delta + n^2(x) \cdot k^2\right) u_k(x) = 0,$$

where  $n(x)$  denotes the index of refraction. The solution for a cavity with a perfect mirror at  $x = 0$  and a partial mirror with amplitude transmission  $t$  and reflectivity  $r$  at  $x = L$  is given by [101]

$$u_k(x) = \begin{cases} \frac{t}{1+re^{2ikL}} \cdot 2i \cdot \sin(kx) & 0 < x < L \\ \frac{1+re^{-2ikL}}{1+re^{2ikL}} \cdot e^{ikx} - e^{-ikx} & L < x < \infty \end{cases}. \quad (\text{B.2})$$

The two terms of the region outside the cavity ( $L < x < \infty$ ) correspond to the outgoing and incoming wave, respectively. The cavity's resonances are given by

$$T(\omega) = \frac{t}{1 + re^{2ikL}} = \frac{t}{1 + re^{2i\omega L/c}}$$

and a resonant enhancement occurs for a perfect mirror ( $r = 1$ ) at  $\frac{2\omega L}{c} = (2n + 1)\pi$ . For the more realistic case of  $r < 1$  we must find a complex solution for  $1 + re^{2i\Omega_n L/c} = 0$ . With  $r = |r|e^{i\phi_r}$  follows

$$\begin{aligned} 1 + re^{2i\Omega_n L/c} &= 0 \\ 1 - |r|e^{2i\Omega_n L/c - i((2n+1)\pi - \phi_r)} &= 0 \\ e^{2i\Omega_n L/c - i((2n+1)\pi - \phi_r)} &= \frac{1}{|r|} \\ 2i\Omega_n L/c - i((2n+1)\pi - \phi_r) &= -\ln r = -\ln \sqrt{1-t^2} \stackrel{t \ll 1}{\approx} -\frac{t^2}{2}, \\ \Rightarrow \Omega_n &= \underbrace{\frac{c}{L}n\pi}_{\omega_n} + \underbrace{\frac{c}{2L}(\pi - \phi_r)}_{\delta\omega} - i \underbrace{\frac{c}{2L}\frac{t^2}{2}}_{\frac{\gamma}{2}}. \end{aligned} \quad (\text{B.3})$$

Expanding  $T(\omega)$  around a cavity resonance  $\omega \approx \omega_n$

$$T(\omega) = \frac{t}{1 + |r|e^{2i(\omega - \Omega_n)L/c}},$$

leads under the assumptions of a 180° phase flip at the mirror ( $\phi_r = \pi \curvearrowright \delta\omega = 0$ ) and an almost ideal mirror reflectivity  $|r| \approx 1$  to the approximated expression

$$\begin{aligned} T(\omega) &\approx \frac{t}{1 - |r|e^{2i(\omega - \Omega_n)L/c}} \\ &= \frac{t}{1 - (1 + 2i(\omega - \Omega_n)L/c)} \\ &= \frac{t}{-2i(\omega - \Omega_n)L/c} \\ &= \frac{ci}{2L} \frac{t}{\omega - \Omega_n}. \end{aligned}$$

With Equation (B.3) the expression becomes

$$\begin{aligned} T(\omega) &\approx \frac{c}{2L} \frac{t}{\gamma/2 - i(\omega - \omega_n)} \\ &= \sqrt{\frac{c}{2L}} \frac{\sqrt{\gamma/2}}{\gamma/2 - i(\omega - \omega_n)}. \end{aligned}$$



The absolute square  $|T(\omega)|^2$  yields the cavity's transmission profile, which is a Lorentzian with center frequency  $\omega_n$  and full width at half maximum  $\gamma$ .

The solution of the electric field within the cavity is with Equations (B.1) and (B.2) given for a continuous frequency distribution as

$$\begin{aligned}
 E^+(x, t) &= -i \sum_k \mathcal{E}_\omega \mathbf{u}_k(x) \hat{a}_k(t) \\
 &= -i \sum_k 2\mathcal{E}_\omega i \cdot \sin(kx) \sqrt{\frac{c}{L}} \frac{\sqrt{\gamma/2}}{\gamma/2 - i(\omega - \omega_n)} \hat{a}_k(t) \\
 &= \sqrt{2} \mathcal{E}_{\omega_n} \cdot \sin(kx) \underbrace{\int d\omega \frac{\sqrt{\gamma/(2\pi)}}{\gamma/2 - i(\omega - \omega_n)} \hat{a}_\omega(t)}_{\hat{a}_c(t) \text{ cavity field operator}}
 \end{aligned}$$

where we used the substitution  $\sum_k \rightarrow \frac{1}{\Delta\omega} \int d\omega$  and  $\hat{a}_k \rightarrow \sqrt{\Delta\omega} \hat{a}_\omega$  with  $\Delta\omega = \frac{2\pi c}{L} \rightarrow 0$  and defined the cavity field operator  $\hat{a}_c(t)$ . The cavity field operator  $\hat{a}_c(t)$  obeys the commutation relation

$$[\hat{a}_c, \hat{a}_c^\dagger] = \int d\omega \frac{\gamma/(2\pi)}{(\gamma/2)^2 + (\omega - \omega_n)^2} = 1,$$

where we used the commutation relation of the continuous field operators  $[\hat{a}_\omega, \hat{a}_{\omega'}^\dagger] = \delta(\omega - \omega')$ . Taking the time evolution of  $\hat{a}_\omega(t) = \hat{a}_\omega(0)e^{-i\omega t}$  into account, we obtain the equation of motion for the cavity operator

$$\begin{aligned}
 \dot{\hat{a}}_c &= \int d\omega \sqrt{\gamma/(2\pi)} \frac{-i\omega}{\gamma/2 - i(\omega - \omega_n)} \hat{a}_\omega(t) \\
 &= \int d\omega \sqrt{\gamma/(2\pi)} \underbrace{\frac{-i\omega + i\omega_n + \gamma/2 - i\omega_n - \gamma/2}{\gamma/2 - i(\omega - \omega_n)}}_{1 - \frac{i\omega_n + \gamma/2}{\gamma/2 - i(\omega - \omega_n)}} \hat{a}_\omega(t) \\
 &= \int d\omega \sqrt{\gamma/(2\pi)} \hat{a}_\omega(t) - (i\omega_n + \gamma/2) \underbrace{\int d\omega \frac{\sqrt{\gamma/(2\pi)}}{\gamma/2 - i(\omega - \omega_n)} \hat{a}_\omega(t)}_{\hat{a}_c(t)} \\
 &= -(i\omega_n + \gamma/2) \hat{a}_c(t) + \sqrt{\gamma} \underbrace{\frac{1}{\sqrt{2\pi}} \int d\omega \hat{a}_\omega(t)}_{\hat{a}_{\text{in}}(\text{vacuum})}.
 \end{aligned}$$

The occurring field  $\hat{a}_{\text{in}}$  has a white noise signature

$$\begin{aligned}\langle \hat{a}_{\text{in}}(t) \hat{a}_{\text{in}}^\dagger(t') \rangle &= \frac{1}{2\pi} \int d\omega \int d\omega' \underbrace{\langle \hat{a}_\omega(0) \hat{a}_{\omega'}^\dagger(0) \rangle}_{\delta(\omega-\omega')} e^{i\omega t} e^{-i\omega' t'} \\ &= \frac{1}{2\pi} \int d\omega e^{i\omega(t-t')} = \delta(t-t')\end{aligned}$$

and corresponds to an in-coupling vacuum field. By moving to the rotating frame, we obtain an expression with the cavity detuning  $\Delta$

$$\dot{\hat{a}}_c = -(i\Delta + \gamma/2) \hat{a}_c(t) + \sqrt{\gamma} \hat{a}_{\text{in}}.$$

The output field  $\hat{a}_{\text{out}}$  for  $x > L$  can be obtained by looking at the outgoing electric field component  $E_{\text{out}}^+(x, t)$

$$\begin{aligned}E_{\text{out}}^+(x, t) &= -i \sum_k \mathcal{E}_\omega \mathbf{u}_k(x) \hat{a}_k(t) \\ &= -i \sum_k \mathcal{E}_\omega \frac{1 + r e^{-2ikL}}{1 + r e^{2ikL}} \cdot e^{ikx} \hat{a}_k(t) \\ &= -i \sum_k \mathcal{E}_\omega \frac{T(\omega)}{T^*(\omega)} \cdot e^{ikx} \hat{a}_k(t) \\ &= -i \sum_k \mathcal{E}_\omega \frac{\gamma/2 + i(\omega - \omega_n)}{\gamma/2 - i(\omega - \omega_n)} \cdot e^{ikx} \hat{a}_k(t) \\ &= -i \sum_k \mathcal{E}_\omega \left( -1 + \frac{\gamma}{\gamma/2 - i(\omega - \omega_n)} \right) \cdot e^{ikx} \hat{a}_k(t) \\ &= -i \mathcal{E}_{\omega_n} e^{ikx} \sqrt{\frac{L}{2\pi c}} \int d\omega \left( -1 + \frac{\gamma}{\gamma/2 - i(\omega - \omega_n)} \right) \hat{a}_\omega(t) \\ &= -i \mathcal{E}_{\omega_n} e^{ikx} \sqrt{\frac{L}{c}} \left[ \underbrace{-\frac{1}{\sqrt{2\pi}} \int d\omega \hat{a}_\omega(t)}_{\hat{a}_{\text{in}}(t)} + \underbrace{\sqrt{\gamma} \int d\omega \frac{\sqrt{\gamma/(2\pi)}}{\gamma/2 - i(\omega - \omega_n)} \hat{a}_\omega(t)}_{\hat{a}_c(t)} \right].\end{aligned}$$

We can hence define the outgoing field operator as

$$\hat{a}_{\text{out}}(t) = -\hat{a}_{\text{in}} + \sqrt{\gamma} \hat{a}_c(t). \quad (\text{B.4})$$

### Nonlinearity

Introducing a nonlinear interaction for twin beam generation with the Hamiltonian

$$\hat{H}_{\text{int}} = d_{\text{eff}} \left( \hat{a}_3 \hat{a}_1^\dagger \hat{a}_2^\dagger + \hat{a}_3^\dagger \hat{a}_1 \hat{a}_2 \right),$$

with the modes 1, 2 and 3 corresponding to signal, idler and pump field, we obtain the cavity differential equation on resonance ( $\Delta = 0$ )

$$\begin{aligned}\dot{\hat{a}}_1 &= -\frac{\gamma}{2}\hat{a}_1 - \sqrt{\gamma}\hat{a}_{\text{in}} + i \underbrace{[\hat{H}_{\text{int}}, \hat{a}_1]}_{-id_{\text{eff}}\hat{a}_3\hat{a}_2^\dagger} \\ &= -\frac{\gamma}{2}\hat{a}_1 - id_{\text{eff}}\hat{a}_3\hat{a}_2^\dagger - \sqrt{\gamma}\hat{a}_{\text{in}}.\end{aligned}$$

Analogously we obtain the cavity equation of motion for the idler and pump field, used in Section 6.2. The degenerated case of squeezing production is obtained in the same way. A detailed description can be found in [102].



## APPENDIX C

---

### Two-Mirror-Cavity with Absorption

---

Cavities are widely used in quantum optics experiments. Here, the calculation of the field properties in transmission and reflection of a two mirror cavity, including a lossy medium, is presented.

We consider the cavity shown in Figure C.1 with *amplitude* reflectivities  $r_i$  and transmittances  $t_i$ . If the distance  $d$  between the two mirrors contains a lossy medium, it will be described by the absorption coefficient  $\beta$ , which expresses the *intensity* absorption in %/cm. The relationship between the amplitudes can be described by the ray transfer matrix formalism [103]. A mirror can be considered as a beam splitter; its ray transfer matrix is given by

$$\begin{aligned} \begin{pmatrix} a_1 \\ a_{\text{refl}} \end{pmatrix} &= \begin{pmatrix} t_1 & r_1 \\ r_1 & -t_1 \end{pmatrix} \begin{pmatrix} a_{\text{in}} \\ a_4 \end{pmatrix}, \\ \begin{pmatrix} a_{\text{trans}} \\ a_3 \end{pmatrix} &= \begin{pmatrix} t_2 & r_2 \\ r_2 & -t_2 \end{pmatrix} \begin{pmatrix} a_2 \\ 0 \end{pmatrix}, \end{aligned} \tag{C.1}$$

where the vacuum input from the back will be set to zero for classical fields. At distance  $d$  the single-path loss is given by

$$\gamma = \exp(-\beta/2 \cdot d), \tag{C.2}$$

while it is important to take the *amplitude* absorption  $\beta/2$  into account.

According to the difference between the frequency of the incident light  $\nu_1$  and the resonance frequency of the cavity

$$\nu_{\text{res}} = n \cdot \frac{c}{2d} = n \cdot \text{FSR}$$

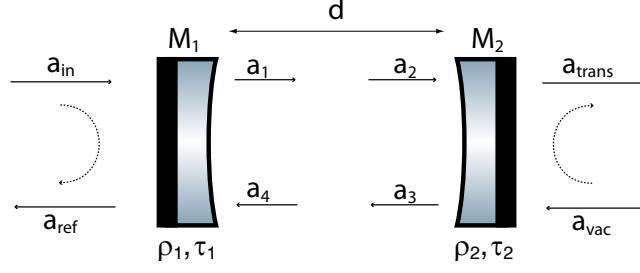


**Figure C.1** – Schematic drawing of a linear cavity.

a phase shift  $\Delta\varphi$  is accumulated. If the length of the cavity is a multiple of the incident wavelength the resonance condition is fulfilled and a power build up can take place. The distance in frequency between two resonances is called the *free spectral range* (FSR). Looking at a round trip, the accumulated phase shift reads

$$\Delta\varphi = 2\pi(\nu_1 - \nu_{\text{res}}) \frac{2d}{c} = 2\pi \frac{\delta\nu}{\text{FSR}} \pmod{2\pi}.$$

Hence, the field propagation through distance  $d$  is described by

$$\begin{aligned} a_2 &= e^{i\Delta\varphi/2 - \beta/2 \cdot d} \cdot a_1, \\ a_4 &= e^{i\Delta\varphi/2 - \beta/2 \cdot d} \cdot a_3. \end{aligned}$$

Solving Equations (C.1) leads to expressions for the involved fields.

$$\begin{aligned} a_3 &= r_2 \cdot a_2 = r_2 \cdot e^{\overbrace{i\Delta\varphi/2 - \beta/2 \cdot d}^{\zeta}} \cdot a_1 \\ &= r_2 \cdot \zeta \cdot (t_1 \cdot a_{\text{in}} + r_1 \cdot a_4) \\ &= \zeta \cdot r_2 t_1 \cdot a_{\text{in}} + r_1 r_2 \cdot \zeta^2 \cdot a_3 \\ &= \frac{\zeta \cdot t_1 r_2}{1 - r_1 r_2 \cdot \zeta^2} \cdot a_{\text{in}}, \end{aligned}$$

$$\begin{aligned} a_1 &= t_1 \cdot a_{\text{in}} + r_1 \cdot a_4 \\ &= t_1 \cdot a_{\text{in}} + r_1 \cdot \zeta \cdot \frac{\zeta \cdot t_1 r_2}{1 - r_1 r_2 \cdot \zeta^2} \cdot a_{\text{in}} \\ &= \left( t_1 + r_1 \cdot \frac{\zeta^2 \cdot t_1 r_2}{1 - r_1 r_2 \cdot \zeta^2} \right) \cdot a_{\text{in}}. \end{aligned}$$

Hence, the transmitted and reflected field amplitudes of the cavity read

$$\begin{aligned}
 a_{\text{trans}} &= t_2 \cdot a_2 = t_2 \cdot \zeta \cdot a_1 \\
 &= t_2 \cdot \zeta \cdot \left( t_1 + r_1 \cdot \frac{\zeta^2 \cdot t_1 r_2}{1 - r_1 r_2 \cdot \zeta^2} \right) \cdot a_{\text{in}} \\
 &= t_1 t_2 \cdot \frac{\zeta}{1 - r_1 r_2 \cdot \zeta^2} \cdot a_{\text{in}}
 \end{aligned}$$

$$\begin{aligned}
 a_{\text{ref}} &= r_1 \cdot a_{\text{in}} - t_1 \cdot a_4 \\
 &= r_1 \cdot a_{\text{in}} - t_1 \cdot \frac{\zeta^2 \cdot t_1 r_2}{1 - r_1 r_2 \cdot \zeta^2} \cdot a_{\text{in}} \\
 &= \left( r_1 - t_1^2 r_1 \cdot \frac{\zeta^2}{1 - r_1 r_2 \cdot \zeta^2} \right) \cdot a_{\text{in}}
 \end{aligned}$$

### Finesse

The finesse of a cavity is defined as the ratio of the FSR to the linewidth, while the latter corresponds to the intensity full width at half maximum (FWHM)

$$\mathcal{F} = \frac{\text{FSR}}{\text{FWHM}}.$$

The maximum is given on resonance with  $\Delta\varphi = 0$ . Therefore, the field propagation through distance  $d$  is solely affected by the intensity loss  $\beta$

$$\zeta = e^{i \cdot \Delta\varphi/2 - \beta/2 \cdot d} \rightarrow e^{-\beta/2 \cdot d} = \gamma.$$

Hence, the transmitted half maximum intensity reads

$$\frac{1}{2} |a_{\text{trans}}(\Delta\varphi = 0)|^2 = \frac{t_1^2 t_2^2 \cdot \gamma^2}{2 \cdot (1 - r_1 r_2 \cdot \gamma^2)^2} \cdot |a_{\text{in}}|^2.$$

With the substitution  $\zeta = \gamma e^{-iz}$ ,  $z = 2\pi \frac{\delta\nu}{2\text{FSR}}$  the full width  $2\delta\nu$  yields

$$\begin{aligned}
 |a_{\text{trans}}|^2 &= \frac{t_1 t_2 \cdot e^{iz} \cdot \gamma}{1 - r_1 r_2 \cdot \gamma^2 (e^{iz})^2} \cdot \frac{t_1 t_2 \cdot e^{-iz} \cdot \gamma}{1 - r_1 r_2 \cdot \gamma^2 (e^{-iz})^2} \cdot |a_{\text{in}}|^2 \\
 &= \frac{t_1^2 t_2^2 \gamma^2}{1 + r_1^2 r_2^2 \gamma^4 - r_1 r_2 \gamma^2 \cdot 2 \cos(2z)} \cdot |a_{\text{in}}|^2 \\
 &\stackrel{!}{=} \frac{1}{2} |a_{\text{trans}}(\Delta\varphi = 0)|^2 = \frac{t_1^2 t_2^2 \cdot \gamma^2}{2 (1 - r_1 r_2 \cdot \gamma^2)^2} \cdot |a_{\text{in}}|^2,
 \end{aligned}$$

$$\sphericalangle \cos(2z) = \cos\left(2\pi \frac{\delta\nu}{\text{FSR}}\right) = \frac{4r_1r_2\gamma^2 - r_1^2r_2^2\gamma^4 - 1}{2r_1r_2\gamma^2}.$$

The final expression for the finesse with absorption reads

$$\mathcal{F} = \frac{\text{FSR}}{2\delta\nu} = \pi \cdot \left[ \arccos\left(\frac{4r_1r_2\gamma^2 - r_1^2r_2^2\gamma^4 - 1}{2r_1r_2\gamma^2}\right) \right]^{-1},$$

while  $\gamma$  is given by Equation (C.2).



---

## Acknowledgments

---

Finally, I would like to take the opportunity to mention those people who contributed to this thesis.

First of all I like to thank our director Prof. Karsten Danzmann for establishing the AEI as a great institute with an excellent scientific environment. For the mentoring I am grateful to my supervisor Prof. Roman Schnabel. It was an exciting experience to be part of a group that performs world's leading research in quantum optics.

The conducted experiments were no “one-man shows”. Collaborations and teamwork led to their success. Carlos Pineda and Prof. Jens Eisert from the University of Potsdam provided the theoretical support for the Bound Entanglement experiment and James DiGuglielmo eased the common hours of laboratory work. The early stage of the Twin Beams experiment was set up with Nicolai Grosse. After he left the institute, the experiment was conducted in a team play with Christina Vollmer, née Laukötter. Christoph Baune joined the team for the Frequency Conversion experiment. You all made a great job, kept me motivated and it was good fun working with you!

Many fruitful discussions with Jaromír Fiurášek, associate professor at Palacký University Olomouc, Czech Republic, Tobias Eberle, Vitus Händchen, Sascha Khalaidovski, Nico Lastzka, Jessica and Sebastian Steinlechner gave seminal impulses for the experiments and the physical understanding of the investigated phenomena.

For proofreading this manuscript I am (in alphabetical order) grateful to Christoph Baune, Paul Cochrane, Tobias Eberle, Nicolai Grosse, Vitus Händchen, Sascha Khalaidovski, Sebastian Steinlechner and Christina Vollmer.

Finally, this thesis would not have been possible without the loving support of my family. Petra and Gert, your support and encouragement kept me grounded all over the years! Almut, your love and confidence cannot be expressed by any words!

THANK YOU!



---

## Curriculum Vitae

---

### Personal Information

---

Aiko Samblowski  
Flüggestr. 22A  
30161 Hannover

Email: Aiko.Samblowski@aei.mpg.de

Date of birth: 06.08.1981

Nationality: German

Marital status: single

### Education

---

since 09/2007	Doctoral studies in physics, Leibniz Universität Hannover. Experimental quantum information
08/2005 – 06/2007	Physics studies, Leibniz Universität Hannover. Graduation (diploma), grade: “with distinction”
09/2004 – 07/2005	Physics studies, University of Strathclyde, Glasgow, Schottland
09/2001 – 08/2004	Physics studies, Leibniz Universität Hannover
08/1994 – 07/2001	Gymnasium Mellendorf, Graduation (Abitur), grade: 2.0

### Graduate School Programs & Scholarships

---

10/2010 – 07/2011	<i>Promotion plus+ qualifiziert</i> , Graduiertenakademie, Leibniz Universität Hannover. Project and conflict management, team coaching and management praxis
06/2009 – 06/2010	<i>Science goes Market</i> , Entrepreneurial PostGraduate Education, Institut für Gründung und Innovation, Universität Potsdam. Including: team building, creativity techniques, moderation and presentation
since 09/2007	Doctoral scholarship of the International Max Planck Research School on Gravitational Wave Astronomy
09/2004 – 07/2005	ERASMUS foreign exchange scholarship, University of Strathclyde, Glasgow, Schottland



---

## List of Publications

---

— 2012 —

16. | C. E. Vollmer, C. Baune, **A. Samblowski**, T. Eberle, V. Händchen, J. Fiurášek and Roman Schnabel, “Quantum Up-Conversion of Squeezed Light from 1550 nm to 532 nm”, in preparation
15. | **A. Samblowski**, C. E. Vollmer, C. Baune, J. Fiurášek and Roman Schnabel, “Highly efficient up-conversion from 1550 nm to 532 nm”, in preparation
14. | V. Händchen, T. Eberle, S. Steinlechner, **A. Samblowski**, R. F. Werner and R. Schnabel, “Observation of one-way Einstein-Podolsky-Rosen steering”, accepted in *Nature Photonics*
13. | B. Sathyaprakash, . . . , A. Rüdiger, **A. Samblowski**, L. Santamará, . . . , K. Yamamoto, “Scientific Objectives of Einstein Telescope”, *Classical and Quantum Gravity* **29**, 124013 (2012).
12. | S. Ast, **A. Samblowski**, M. Mehmet, S. Steinlechner, T. Eberle and R. Schnabel, “Continuous-wave nonclassical light with gigahertz squeezing bandwidth”, *Optics Letters* **34**, 2367 (2012).
11. | J. Abadie, . . . , F. Salemi, **A. Samblowski**, L. Sammut, . . . , J. Zweizig, “Search for Gravitational Waves from Low Mass Compact Binary Coalescence in LIGO’s Sixth Science Run and Virgo’s Science Runs 2 and 3”, *Physical Review D* **85**, 082002 (2012).

10. | J. Abadie, . . . , F. Salemi, **A. Sambrowski**, L. Sammut, . . . , J. Zweizig, “All-sky search for periodic gravitational waves in the full S5 LIGO data”, *Physical Review D* **85**, 022001 (2012).

— 2011 —

9. | J. DiGuglielmo, **A. Sambrowski**, B. Hage, C. Pineda, J. Eisert and R. Schnabel, “Experimental Unconditional Preparation and Detection of a Continuous Bound Entangled State of Light”, *Physical Review Letters* **107**, 240503 (2011).
8. | J. Abadie, . . . , F. Salemi, **A. Sambrowski**, L. Sammut, . . . , J. Zweizig, “A gravitational wave observatory operating beyond the quantum shot-noise limit”, *Nature Physics* **7**, 962 (2011).
7. | **A. Sambrowski**, C.E. Laukötter, N. Grosse, P.K. Lam and R. Schnabel, “Two Color Entanglement”, *AIP Conference Proceedings* **1363**, 219 (2011).

— 2010 —

6. | B. Hage, **A. Sambrowski**, J. DiGuglielmo, J. Fiurášek and R. Schnabel, “Iterative Entanglement Distillation: Approaching the Elimination of Decoherence”, *Physical Review Letters* **105**, 230502 (2010).
5. | B. Hage, **A. Sambrowski** and R. Schnabel, “Towards Einstein-Podolsky-Rosen quantum channel multiplexing”, *Physical Review A* **81**, 62301 (2010).

— 2009 —

4. | T. Kiesel, W. Vogel, B. Hage, J. DiGuglielmo, **A. Sambrowski** and R. Schnabel, “Experimental test of nonclassicality criteria for phase-diffused squeezed states”, *Physical Review A* **79**, 22122 (2009).
3. | J. DiGuglielmo, C. Messenger, J. Fiurášek, B. Hage, **A. Sambrowski**, T. Schmidt, and R. Schnabel, “Markov chain Monte Carlo estimation of quantum states”, *Physical Review A* **79**, 32114 (2009).

## — 2008 —

2. | B. Hage, **A. Samblowski**, J. DiGuglielmo, A. Franzen, J. Fiurášek and R. Schnabel, “Preparation of distilled and purified continuous-variable entangled states”, *Nature Physics* **4**, 915 (2008).
1. | S. Steinlechner, S. Barke, J. Dück, L. Hoppe, R. A. Lorbeer, M. Otto, **A. Samblowski** and T. Westphal, “Der Lifter”, *PhyDid A* **7**, 20 (2008).





---

## Bibliography

---

- [1] M. Planck, “Ueber das Gesetz der Energieverteilung im Normalspectrum”, *Annalen der Physik* **309**, 553 (1901).
- [2] A. Einstein, B. Podolsky and N. Rosen, “Can Quantum-Mechanical Description of Physical Reality Be Considered Complete?”, *Physical Review* **47**, 777 (1935).
- [3] J. S. Bell, “On the Einstein Podolsky Rosen Paradox”, *Physics* **1**, 195 (1964).
- [4] A. Aspect, J. Dalibard and G. G. Roger, “Experimental test of Bell’s inequalities using time-varying analyzers”, *Physical Review Letters* **49**, 1804 (1982).
- [5] H. Kimble, M. Dagenais and L. Mandel, “Photon Antibunching in Resonance Fluorescence”, *Physical Review Letters* **39**, 691 (1977).
- [6] R. E. Slusher, L. W. Hollberg, B. Yurke, J. C. Mertz and J. F. Valley, “Observation of Squeezed States Generated by Four-Wave Mixing in an Optical Cavity”, *Physical Review Letters* **55**, 2409 (1985).
- [7] Z. Y. Ou, S. F. Pereira, H. J. Kimble and K. C. Peng, “Realization of the Einstein-Podolsky-Rosen paradox for continuous variables”, *Physical Review Letters* **68**, 3663 (1992).
- [8] L. Vaidman, “Teleportation of quantum states”, *Physical Review A* **49**, 1473 (1994).
- [9] S. L. Braunstein and H. J. Kimble, “Teleportation of Continuous Quantum Variables”, *Physical Review Letters* **80**, 869 (1998).

- [10] A. Furusawa, J. L. Sørensen, S. L. Braunstein, C. Fuchs, H. Kimble and E. S. Polzik, “Unconditional Quantum Teleportation”, *Science* **282**, 706 (1998).
- [11] S. Pirandola and S. Mancini, “Quantum teleportation with continuous variables: A survey”, *Laser Physics* **16**, 1418 (2006).
- [12] S. Braunstein and H. Kimble, “Dense coding for continuous variables”, *Physical Review A* **61**, 042302 (2000).
- [13] X. Li, Q. Pan, J. Jing, J. Zhang, C. Xie and K. Peng, “Quantum Dense Coding Exploiting a Bright Einstein-Podolsky-Rosen Beam”, *Physical Review Letters* **88**, 047904 (2002).
- [14] S. L. Braunstein and P. van Loock, “Quantum information with continuous variables”, *Reviews of Modern Physics* **77**, 513 (2005).
- [15] T. Ralph, “Continuous variable quantum cryptography”, *Physical Review A* **61**, 010303(R) (1999).
- [16] X. Su, J. Jing, Q. Pan and C. Xie, “Dense-coding quantum key distribution based on continuous-variable entanglement”, *Physical Review A* **74**, 062305 (2006).
- [17] X. Su, W. Wang, Y. Wang, X. Jia, C. Xie and K. Peng, “Continuous variable quantum key distribution based on optical entangled states without signal modulation”, *EPL (Europhysics Letters)* **87**, 20005 (2009).
- [18] V. Scarani, H. Bechmann-Pasquinucci, N. Cerf, M. Dušek, N. Lütkenhaus and M. Peev, “The security of practical quantum key distribution”, *Reviews of Modern Physics* **81**, 1301 (2009).
- [19] A. Kozhekin, K. Mølmer and E. Polzik, “Quantum memory for light”, *Physical Review A* **62**, 033809 (2000).
- [20] B. Julsgaard, J. Sherson, J. I. Cirac, J. Fiurášek and E. S. Polzik, “Experimental demonstration of quantum memory for light.”, *Nature* **432**, 482 (2004).
- [21] S. Tan, “Confirming entanglement in continuous variable quantum teleportation”, *Physical Review A* **60**, 2752 (1999).
- [22] X. Jia, X. Su, Q. Pan, J. Gao, C. Xie and K. Peng, “Experimental Demonstration of Unconditional Entanglement Swapping for Continuous Variables”, *Physical Review Letters* **93**, 250503 (2004).

- [23] J. Fiurášek, P. Marek, R. Filip and R. Schnabel, “Experimentally feasible purification of continuous-variable entanglement”, *Physical Review A* **75**, 050302 (2007).
- [24] B. Hage, A. Sambrowski, J. DiGuglielmo, A. Franzen, J. Fiurášek and R. Schnabel, “Preparation of distilled and purified continuous-variable entangled states”, *Nature Physics* **4**, 915 (2008).
- [25] R. Dong, M. Lassen, J. Heersink, C. Marquardt, R. Filip, G. Leuchs and U. L. Andersen, “Experimental entanglement distillation of mesoscopic quantum states”, *Nature Physics* **4**, 919 (2008).
- [26] R. Ukai, N. Iwata, Y. Shimokawa, S. Armstrong, A. Politi, J. i. Yoshikawa, P. van Loock and A. Furusawa, “Demonstration of Unconditional One-Way Quantum Computations for Continuous Variables”, *Physical Review Letters* **106**, 240504 (2011).
- [27] R. Ukai, S. Yokoyama, J. i. Yoshikawa, P. van Loock and A. Furusawa, “Demonstration of a Controlled-Phase Gate for Continuous-Variable One-Way Quantum Computation”, *Physical Review Letters* **107**, 250501 (2011).
- [28] M. Horodecki, J. Oppenheim and R. Horodecki, “Are the Laws of Entanglement Theory Thermodynamical?”, *Physical Review Letters* **89**, 24 (2002).
- [29] F. G. S. L. Brandão and M. B. Plenio, “Entanglement theory and the second law of thermodynamics”, *Nature* **4**, 873 (2008).
- [30] P. Horodecki, M. Horodecki and R. Horodecki, “Bound Entanglement Can Be Activated”, *Physical Review Letters* **82**, 1056 (1999).
- [31] G. Smith, J. A. Smolin and J. Yard, “Quantum communication with Gaussian channels of zero quantum capacity”, *Nature Photonics* **5**, 624 (2011).
- [32] M. Sasaki *et al.*, “Field test of quantum key distribution in the Tokyo QKD Network”, *Optics Express* **19**, 10387 (2011).
- [33] M. J. Li and D. A. Nolan, “Optical Transmission Fiber Design Evolution”, *Journal of Lightwave Technology* **26**, 1079 (2008).
- [34] H. J. Briegel, W. Dür, J. I. Cirac and P. Zoller, “Quantum Repeaters: The Role of Imperfect Local Operations in Quantum Communication”, *Physical Review Letters* **81**, 5932 (1998).

- [35] L. M. M. Duan, M. D. Lukin, J. I. Cirac and P. Zoller, “Long-distance quantum communication with atomic ensembles and linear optics.”, *Nature* **414**, 413 (2001).
- [36] K. Honda, D. Akamatsu, M. Arikawa, Y. Yokoi, K. Akiba, S. Nagatsuka, T. Tanimura, A. Furusawa and M. Kozuma, “Storage and Retrieval of a Squeezed Vacuum”, *Physical Review Letters* **100**, 93601 (2008).
- [37] J. Appel, E. Figueroa, D. Korystov, M. Lobino and a. I. Lvovsky, “Quantum Memory for Squeezed Light”, *Physical Review Letters* **100**, 93602 (2008).
- [38] I. Afek, O. Ambar and Y. Silberberg, “High-NOON states by mixing quantum and classical light.”, *Science* **328**, 879 (2010).
- [39] C. M. Caves, “Quantum-mechanical noise in an interferometer”, *Physical Review D* **23**, 1693 (1981).
- [40] The LSC, “A gravitational wave observatory operating beyond the quantum shot-noise limit”, *Nature Physics* **7**, 962 (2011).
- [41] M. Mehmet, S. Ast, T. Eberle, S. Steinlechner, H. Vahlbruch and R. Schnabel, “Squeezed light at 1550 nm with a quantum noise reduction of 12.3 dB”, *Optics Express* **19**, 25763 (2011).
- [42] S. Kawamura *et al.*, “The Japanese space gravitational wave antenna – DECIGO”, *Classical and Quantum Gravity* **23**, S125 (2006).
- [43] J. C. Maxwell, “A Dynamical Theory of the Electromagnetic Field”, *Philosophical Transactions of the Royal Society of London* **155**, 459 (1865).
- [44] A. Einstein, “Über einen die Erzeugung und Verwandlung des Lichtes betreffenden heuristischen Gesichtspunkt”, *Annalen der Physik* **322**, 132 (1905).
- [45] R. J. Glauber, “Quantum Theory of Optical Coherence: Selected Papers and Lectures”, Wiley-VCH (2007), ISBN 3527406875.
- [46] R. J. Glauber, “Coherent and incoherent states of the radiation field”, *Physical Review* **131**, 2766 (1963).
- [47] R. W. Boyd, “Nonlinear Optics”, Academic Press; 3rd revised edition (2008), ISBN 0123694701.
- [48] C. C. Gerry and P. L. Knight, “Introductory Quantum Optics”, Cambridge University Press (2005), ISBN 9780521820356.

- [49] M. O. Scully and M. S. Zubairy, “Quantum Optics”, Cambridge University Press (1997), ISBN 0521435951.
- [50] W. Heisenberg, “Über den anschaulichen Inhalt der quantentheoretischen Kinematik und Mechanik”, *Zeitschrift für Physik* **43**, 172 (1927).
- [51] E. Wigner, “On the quantum correction for thermodynamic equilibrium”, *Physical Review* **40**, 749 (1932).
- [52] U. Leonhardt, “Measuring the Quantum State of Light”, Cambridge University Press (1997), ISBN 978-0521497305.
- [53] W.P. Schleich, “Quantum Optics in Phase Space”, Wiley-VCH Verlag GmbH (2001), ISBN 352729435X.
- [54] R. Simon, “Peres-Horodecki Separability Criterion for Continuous Variable Systems”, *Physical Review Letters* **84**, 2726 (2000).
- [55] C. Weedbrook, S. Pirandola, R. Garcia-Patron, N. J. Cerf, T. C. Ralph, J. H. Shapiro and S. Lloyd, “Gaussian Quantum Information”, *arXiv* **1110.3234** (2011).
- [56] A. Franzen, B. Hage, J. DiGuglielmo, J. Fiurášek and R. Schnabel, “Experimental Demonstration of Continuous Variable Purification of Squeezed States”, *Physical Review Letters* **97**, 150505 (2006).
- [57] H. Yuen and J. Shapiro, “Optical communication with two-photon coherent states—Part III: Quantum measurements realizable with photoemissive detectors”, *IEEE Transactions on Information Theory* **26**, 78 (1980).
- [58] M. Horodecki, P. Horodecki and R. Horodecki, “Mixed-State Entanglement and Distillation: Is there a "Bound" Entanglement in Nature?”, *Physical Review Letters* **80**, 5239 (1998).
- [59] C. Bennett, G. Brassard, S. Popescu, B. Schumacher, J. Smolin and W. Wootters, “Purification of Noisy Entanglement and Faithful Teleportation via Noisy Channels”, *Physical Review Letters* **76**, 722 (1996).
- [60] J. Eisert, D. E. Browne, S. Scheel and M. B. Plenio, “Distillation of continuous-variable entanglement with optical means”, *Annals of Physics* **311**, 431 (2004).
- [61] R. Horodecki, P. Horodecki, M. Horodecki and K. Horodecki, “Quantum entanglement”, *Reviews of Modern Physics* **81**, 865 (2009).

- [62] R. F. Werner and M. M. Wolf, “Bound Entangled Gaussian States”, *Physical Review Letters* **86**, 3658 (2001).
- [63] G. Giedke and I. J. Cirac, “Characterization of Gaussian operations and distillation of Gaussian states”, *Physical Review A* **66**, 32316 (2002).
- [64] P. Hyllus and J. Eisert, “Optimal entanglement witnesses for continuous-variable systems”, *New Journal of Physics* **8**, 51 (2006).
- [65] A. Peres, “Separability Criterion for Density Matrices”, *Physical Review Letters* **77**, 1413 (1996).
- [66] J. DiGuglielmo, A. Sambrowski, B. Hage, C. Pineda, J. Eisert and R. Schnabel, “Experimental Unconditional Preparation and Detection of a Continuous Bound Entangled State of Light”, *Physical Review Letters* **107**, 240503 (2011).
- [67] A. Serafini and G. Adesso, “Standard forms and entanglement engineering of multimode Gaussian states under local operations”, *Journal of Physics A: Mathematical and Theoretical* **40**, 8041 (2007).
- [68] InnoLight, “<http://www.innolight.de> – Innovative Laser und Systemtechnik GmbH”.
- [69] E. D. Black, “An introduction to Pound-Drever-Hall laser frequency stabilization”, *American Journal of Physics* **69**, 79 (2001).
- [70] S. Chelkowski, H. Vahlbruch, K. Danzmann and R. Schnabel, “Coherent control of broadband vacuum squeezing”, *Physical Review A* **75**, 43814 (2007).
- [71] B. Hage, “Purification and Distillation of Continuous Variable Entanglement”, Dissertation, Gottfried Wilhelm Leibniz Universität Hannover (2010).
- [72] S. Shapiro and M. B. Wilk, “An Analysis of Variance Test for Normality (Complete Samples)”, *Biometrika* **52**, 591 (1965).
- [73] H. Büning and G. Trenkler, “Nichtparametrische statistische Methoden”, Gruyter (1994), ISBN 978-3110163513.
- [74] J. DiGuglielmo, “On the Experimental Generation and Characterization of Entangled States of Light”, Dissertation, Gottfried Wilhelm Leibniz Universität Hannover (2010).
- [75] S. L. Braunstein and A. K. Pati (editors) “Quantum Information Theory with Continuous Variables”, Kluwer Academic Publishers (2002).

- [76] R. C. Eckardt, C. D. Nabors, W. J. Kozlovsky and R. L. Byer, “Optical parametric oscillator frequency tuning and control”, *Journal of the Optical Society of America B* **8**, 646 (1991).
- [77] S. Schiller, “OPTICAL PARAMETRIC DEVICE Optical Parametric Oscillators (Continuous Wave)”, B. Guenther (editor) “Encyclopedia of Modern Optics”, 51–62, Elsevier (2005).
- [78] A. S. Lane, M. D. Reid and D. F. Walls, “Quantum analysis of intensity fluctuations in the nondegenerate parametric oscillator”, *Physical Review A* **38**, 788 (1988).
- [79] S. Reynaud and A. Heidmann, “A semiclassical linear input output transformation for quantum fluctuations”, *Optics Communications* **71**, 209 (1989).
- [80] C. Fabre, E. Giacobino, A. Heidmann and S. Reynaud, “Noise characteristics of a non-degenerate Optical Parametric Oscillator-Application to quantum noise reduction”, *Journal de Physique* **50**, 1209 (1989).
- [81] L. M. Duan, G. Giedke, J. I. Cirac and P. Zoller, “Inseparability criterion for continuous variable systems”, *Physical Review Letters* **84**, 2722 (2000).
- [82] B. Hage, A. Sambrowski and R. Schnabel, “Towards Einstein-Podolsky-Rosen quantum channel multiplexing”, *Physical Review A* **81**, 62301 (2010).
- [83] P. Kumar, “Quantum frequency conversion”, *Optics Letters* **15**, 1476 (1990).
- [84] A. Freise, “<http://www.gwoptics.org/finesse/> – Finesse, an interferometer simulation tool”, (2009).
- [85] S. Ast, R. M. Nia, A. Schönbeck, N. Lastzka, J. Steinlechner, T. Eberle, M. Mehmet, S. Steinlechner and R. Schnabel, “High-efficiency frequency doubling of continuous-wave laser light”, *Optics Letters* **36**, 3467 (2011).
- [86] N. Lastzka, “Numerical modelling of classical and quantum effects in non-linear optical systems”, Dissertation, Gottfried Wilhelm Leibniz Universität Hannover (2010).
- [87] J. Nelder and R. Mead, “A simplex method for function minimization”, *The Computer Journal* **7**, 308 (1965).
- [88] E. Amsellem and M. Bourennane, “Experimental four-qubit bound entanglement”, *Nature Physics* **5**, 748 (2009).

- [89] J. Lavoie, R. Kaltenbaek, M. Piani and K.J. Resch, “Experimental bound entanglement?”, *Nature Physics* **6**, 827 (2010).
- [90] J. T. Barreiro, P. Schindler, O. Gühne, T. Monz, M. Chwalla, C.F. Roos, M. Hennrich and R. Blatt, “Experimental multiparticle entanglement dynamics induced by decoherence”, *Nature Physics* **6**, 943 (2010).
- [91] J. Lavoie, R. Kaltenbaek, M. Piani and K. Resch, “Experimental Bound Entanglement in a Four-Photon State”, *Physical Review Letters* **105**, 1 (2010).
- [92] P. Horodecki, J. I. Cirac and M. Lewenstein, “Bound entanglement for continuous variables is a rare phenomenon”, *arXiv* **0103.076** (2001).
- [93] Y. Li, X. Guo, X. Wang and K. Zhang, “Observation of two-color continuous variable quantum correlation at 0.8 and 1.5  $\mu\text{m}$ ”, (2010).
- [94] Y. Li, X. Guo, Z. Bai and C. Liu, “Generation of two-color continuous variable quantum entanglement at 0.8 and 1.5  $\mu\text{m}$ ”, *Applied Physics Letters* **97**, 031107 (2010).
- [95] J.S. Neergaard-Nielsen, B. M. Nielsen, C. Hettich, K. Mølmer and E. S. Polzik, “Generation of a Superposition of Odd Photon Number States for Quantum Information Networks”, *Physical Review Letters* **97**, 83604 (2006).
- [96] A. Ourjoumtsev, H. Jeong, R. Tualle-Brouri and P. Grangier, “Generation of optical ‘Schrödinger cats’ from photon number states”, *Nature* **448**, 784 (2007).
- [97] S.S. Boyd and L. Vandenberghe, “Convex Optimization”, Cambridge University Press, [www.stanford.edu/~boyd/cvxbook/bv\\_cvxbook.pdf](http://www.stanford.edu/~boyd/cvxbook/bv_cvxbook.pdf) (2004), ISBN 978-0521833783.
- [98] J. Löfberg, “YALMIP: A Toolbox for Modeling and Optimization in MATLAB”, *Proceedings of the CACSD Conference* (2004).
- [99] SeDuMi, “<http://sedumi.ie.lehigh.edu/> – A matlab toolbox to solve optimization problems”, (2004).
- [100] K. Hammerer, “Lecture Notes on Nonclassical Light”, Leibniz Universität Hannover (2011).
- [101] W. Vogel and D.G. Welsch, “Quantum Optics”, Wiley-VCH (2006), ISBN 3527405070.
- [102] D. Walls and G.J. Milburn, “Quantum Optics”, Springer (2007), ISBN 3540285733.



- [103] A. E. A. Siegman, "Lasers", University Science Books (1986), ISBN 0935702113.